THESIS

DAYTIME EVOLUTION OF OXIDIZED REACTIVE NITROGEN IN WESTERN U.S. WILDFIRE SMOKE PLUMES: *IN SITU* AND SATELLITE OBSERVATIONS

Submitted by
Julieta Fernanda Juncosa Calahorrano
Department of Atmospheric Science

In partial fulfillment of the requirements
For the Degree of Master of Science
Colorado State University
Fort Collins, Colorado
Fall 2020

Master's Committee:

Advisor: Emily V. Fischer

Tami Bond
Jeffrey R. Pierce
A.R. Ravishankara

ABSTRACT

DAYTIME EVOLUTION OF OXIDIZED REACTIVE NITROGEN IN WESTERN U.S. WILDFIRE SMOKE PLUMES: *IN SITU* AND SATELLITE OBSERVATIONS

The Western Wildfire Experiment for Cloud Chemistry, Aerosol Absorption, and Nitrogen (WE-CAN) deployed the NSF/NCAR C-130 aircraft in summer 2018 across the western U.S. to sample wildfire smoke during its first day of atmospheric evolution. We present a summary of a subset of oxidized nitrogen species (NO_y) in plumes sampled in a pseudo-lagrangian fashion. Emissions of nitrogen oxides ($NO_x = NO + NO_2$) and nitrous acid (HONO) are rapidly converted to more oxidized forms. Within 4 hours, $\sim$86% of the measured NO_y ($\sum NO_y$) is in the form of peroxy acyl nitrates (PANs) ($\sim$37%), particulate nitrate (pNO$_3$) ($\sim$26%) and gas-phase organic nitrates ($\sim$23%). The average e-folding time and distance for NO_x are $\sim$90 minutes and $\sim$40 km, respectively. Nearly no enhancements in nitric acid (HNO_3) were observed in plumes sampled in a pseudo-lagrangian fashion, implying HNO_3-limited ammonium nitrate (NH_4NO_3) formation, with one notable exception that we highlight as a case study. We also summarize the observed partitioning of $\sum NO_y$ in all the smoke-impacted samples intercepted during WE-CAN. In the smoke-impacted samples intercepted below 3 km above sea level (ASL), HNO_3 is the dominant form of $\sum NO_y$ and its relative contribution increases with smoke age. Above 3 km ASL, the contributions of PANs and pNO$_3$ to $\sum NO_y$ increase with altitude. WE-CAN also sampled smoke from multiple fires mixed with anthropogenic emissions over the California Central Valley. We distinguish samples where anthropogenic NO_x emissions appear to lead to an increase in NO_x abundances by a factor of 4 and contribute to additional PAN formation.

We utilize data from the Cross-Track Infrared Sounder (CrIS) on the Suomi National Polar-orbiting Partnership (Suomi-NPP) satellite, which continues the thermal infrared peroxyacetyl nitrate (PAN) satellite record established by the Tropospheric Emission Spectrometer (TES) onboard the Aura satellite. CrIS provides improved spatial resolution, allowing for improved analysis opportunities. Here we present an analysis of CrIS PAN retrievals over the western US during the summer 2018 wildfire season. The analysis period coincides with WE-CAN. CrIS is capable of detecting PAN and CO enhancements from smoke plumes sampled during WE-CAN, especially those that became active before the satellite overpass or burned for several days (*e.g.,* Carr Fire, Mendocino Complex Fire). The analysis show that ∼40 - 70% of PAN over the western U.S. can be attributed to smoke from wildfires. The contribution of smoke from wildfires to free tropospheric PAN generally increases with latitude. We calculate peroxyacetyl nitrate (PAN) excess mixing ratios normalized by CO (NEMRs) in fresh smoke plumes from fires and follow the evolution as these plumes are transported several hours to days downwind. This analysis shows that elevated PAN within smoke plumes can be detected several states downwind from the fire source. The combination of high CrIS spatial resolution and favorable background conditions on 13 September 2018 permits detecting chemical changes within the Pole Creek smoke plume in Utah. In this plume, CrIS PAN NEMRs increase from < 1% to 3.5% within 3 - 4 hours of physical aging. These results are within the range observed in fresh plumes sampled during WE-CAN, where PAN NEMRs increased from 1.5% to 4% within 4 hours of physical aging.

ACKNOWLEDGEMENTS

First, I would like to thank my committee members: Tami, Jeff, and Ravi. I feel really fortunate to work with you and get to know you better. Thank you for the useful comments that helped me improve my work. You are outstanding scientists, and your work inspires me to be a better one and work towards a better world. On top of that, you are all wonderful human beings. I have enjoyed getting to know you better and witness your kindness and caring for others!

An immense thanks to my advisor Emily V. Fischer. Emily, I feel so happy to work by your side. You are such an inspiration on so many levels. Thank you for being such a well-rounded advisor. Thank you for pushing me to keep the big picture in mind while also paying attention to the details. Thank you for being passionate about making science more inclusive to minority groups. Thank you for teaching me that scientists can have a direct and tangible impact on their communities, and that better science and more creative solutions result from working with diverse teams. Specially thanks for encouraging me to raise my voice and take my space in the room. Thank you for making me even more excited about open water swimming by telling me all about your Horsetooth Reservoir swimming practices. Hopefully in a post COVID-19 world we can swim together. Thank you for keep learning about anything and everything as you go and teaching us that learning is a process that never stops. These two years have been a phenomenal journey. I look forward to our journey through my Ph.D.

I also want to express my immense gratitude to the Fischer group: Zitely, Ilana, Jared, Jakob, Kate, Jake, Steve, Brittany, and Juliet. I feel so fortunate to have met you all at some point. Zitely, thank you so much for chatting with me, answering all my questions, and your helpful advice months before I arrived at Fort Collins. You were such an important support back then and I am happy to have you as a mentor now. Ilana, thank you for all the fun time in the lab, and for always pushing me to be better at building and understanding our instruments. Thanks to my office mates Jared and Jakob, for all the conversations, jokes, and good times. Thanks to Kate, who is such a great scientist and a fun person to be around. Thanks to Steve for all his craziness and kindness. Thanks to Brittany, Jake, and Juliet, even when I met you briefly, you were always kind to me!

I want to thank my Fulbright family, you are a wonderful group of people. I am so lucky to have you in my life. A special thanks to Vicky G., Chimgee N., Joaquín C., JuanMa E., and Ali M. I could not have asked for a better group of people to start this journey with. I love you. Thanks to all the friends that I made in Fort Collins. A particular thanks to Drew K., I-Ting K., Jhordanne J., Ting-Yu C., Chealsea N., Michael D., Iván A., Luciana, F. and Ali A. I want to thank all of you for the fun times and not so fun ones. Vicky, Drew, I-Ting, and Ali M., thank you for being there for me in the tough times. Your caring and kindness were so crucial to me. Thanks for all the music, the beer, and the food that we enjoyed together. Thank you to those that willingly explored this beautiful country with me. My trips with you are amongst the best memories during these two years. Joaquín, thank you for enjoying near-death experiences with me. Please, do not stop pushing me to go crazy, but also, let's try to stay alive! I look forward to collecting more good memories with all of you!

I want to heartily thank my family: José Juncosa, Narcisa Calahorrano, Javier Juncosa, and Gabriela Juncosa. All the conversations, jokes, card games, trips around Ecuador, meals together, and so much more have made me who I am. I am incredibly thankful for your support in the last four years. A special thanks to my parents. Dad, thank you for teasing me and letting me tease you. Whenever I talk to you, I know I will have a good time. Mom, you are an inspiration to me. You are hard-working, fun, energetic, loving, and kind, all at the same time! I can only hope to be as good as you are!

TABLE OF CONTENTS

LIST OF TABLES

LIST OF FIGURES

Chapter 1

Introduction

Biomass burning directly impacts air quality, nutrient cycles, and climate by releasing large amounts of trace gases and particulate matter into the atmosphere ([1], [2], [3], [4]). Because western U.S. wildfire activity is expected to increase in a drier and warmer climate ([5], [6], [7], [8], [9], [10], [11]), it is vital to understand the impacts of smoke on atmospheric composition on local and regional scales. Here we focus on the evolution of oxidized nitrogen in western U.S. wildfire smoke plumes. Understanding the near-source first day of evolution of the oxidized nitrogen in smoke is necessary to predict its further partitioning (*i.e.,* species, phase, amount) as plumes age ([12], [13]). The partitioning and evolution of the oxidized nitrogen emitted from fires drives the production of free radicals ([14]) and oxidants in wildfire plumes, which in turn drives the formation and removal of secondary pollutants (*e.g.,* [15], [16], [13], [17]. Moreover, longer-lived non-radical reservoir species such as peroxy acyl nitrates (PANs) can travel long distances impacting air composition on regional and global scales (*e.g.,* [18], [19], [20], [21]).

Prior field, laboratory, and modeling experiments provide strong foundational knowledge of the emissions and evolution of oxidized nitrogen emissions from biomass burning. During biomass burning, nitrogen in the fuel is released into the atmosphere ([22], [23]). Different forms of nitrogen are emitted or formed during different processes. Small nitrogen-containing molecules (*e.g.,* hydrogen cyanide (HCN), ammonia (NH_3), and isocyanic acid (HNCO)) are typically emitted during pyrolysis ([24], [25], [26]). Radical chemistry within flames converts these species to more oxidized forms including N_2, nitrous oxide (N_2O), nitrogen oxide (NO), nitrogen dioxide (NO_2), and nitrous acid (HONO) ([27], [28]). The most abundant emitted reactive N species include nitrogen oxides (NO_x = NO + NO_2), ammonia (NH_3), nitrous acid (HONO), hydrogen cyanide (HCN), and acetonitrile (CH_3CN) (*e.g.,* [4], [29], [30]). Laboratory and field studies have shown that for a given fuel, emissions of reduced forms of nitrogen (*e.g.,* NH_3) are favored during smoldering conditions, whereas oxidized forms of nitrogen (*e.g.,* NO, NO_2) are favored during flaming conditions ([31], [32], [33], [34]).

The species and phase of oxidized nitrogen in smoke plumes are rapidly processed chemically within minutes to hours after emission. For example, observations of smoke from deforestation and crop residue fires in the Yucatan Peninsula ([17]), boreal fires ([15]), and chaparral fires in California ([16]) suggest fast conversion (within 1-2 hours) of NO_x into more oxidized forms such as peroxyacetyl nitrate (PAN) and other nitrates. Liu et al. ([13]) report on emissions and the first hour of the evolution of trace gases from 15 agricultural fires in the southeast U.S. They observed fast PAN and aerosol nitrate production and little to no gas-phase nitric acid (HNO_3) enhancement in the plumes. These observations suggest that PAN and aerosol nitrate comprise a large portion of the total NO_x in smoke plumes that are more than a few hours old. In addition, Briggs et al. ([35]) report that in aged smoke plumes (*i.e.,* 1-2 days) observed over the U.S. Pacific Northwest, NO_x, PAN, and aerosol nitrate comprise on average 11%, 36%, and 51%, respectively, of the observed total NO_x. While many past field campaigns have quantified NO_x, PANs, and aerosol nitrate in smoke, observations of many of the other oxidized species including multifunctional organic nitrates, and peroxy nitrates are rare. In contrast to the work we present here, their overall contribution is often inferred from measurements of total NO_x.

A more limited body of existing research also provides several insights into oxidized nitrogen chemistry in situations where smoke from western U.S. wildfires mixes with urban emissions. Lindaas et al. ([36]) report on aged smoke *i.e.,* 2-3 days) from the Pacific Northwest and Canada impacting the urban Colorado Front Range. They observed several perturbations to the local NO_x budget, including PAN and peroxypropionyl nitrate (PPN) enhancements of $\sim$100% above background concentrations as well as shifts in the peak of the diurnal cycle of PAN to later in the day during the smoke-impacted periods. Similar to PAN and PPN, lower-mass alkyl nitrate molecules (C_1-C_2) showed enhancements (41% and 31% for methyl and ethyl nitrate, respectively) while the higher-mass alkyl nitrate molecules (C_3-C_5) showed shifts later in the day in their diurnal cycle peaks. NO_2 was enhanced compared to smoke-free time periods near sunrise and sunset. Singh et al. ([37]) used aircraft observations of smoke mixed with urban emissions from the Arctic Research of the Composition of the Troposphere from Aircraft and Satellites (ARCTAS)-CARB campaign to challenge a regional air quality model (CMAQ). The model substantially underpredicted observations of secondary pollutants (ozone (O_3), PAN, and formaldehyde (HCHO)). Similarly, Cai et al. ([38]) used the observations from the ARCTAS-CARB campaign to evaluate the predictions of a fine-resolution regional air quality modeling system. The model results predicted the total NO_x mixing ratios; however, larger uncertainties were found in the partitioning between individual NO_x compounds. The available literature (*e.g.,* [37], [38]) shows that when smoke-impacted air masses mix with urban emissions, there is additional chemistry that might not be represented in air quality models. Air quality models require improvements to emission estimates, chemical mechanisms (including more detailed photochemistry), plume injection height, and meteorological inputs, to improve the results on nitrogen chemistry in smoke-impacted air masses ([38]).

There are relatively few examples of wildfire smoke plumes where all the key species relevant to the conversion of emissions of NO_x and HONO to their oxidation products have been simultaneously measured to allow for "bottom up" accounting of NO_x. The Western Wildfire Experiment for Cloud Chemistry, Aerosol Absorption, and Nitrogen (WE-CAN) field campaign provides an opportunity to examine the partitioning of oxidized reactive nitrogen across a variety of western U.S. wildfire smoke plumes. During the summer 2018 fire season, an instrumented National Science Foundation/National Center for Atmospheric Research (NSF/NCAR) C-130 research aircraft sampled the emissions and near-field (< 400 km from the centroid of the active burn area) evolution of >20 western U.S. wildfire plumes. The aircraft payload consisted of a large suite of instrumentation for the measurement of major anticipated NO_x species. The aircraft also intercepted numerous smoke plumes from additional wildfires across the western U.S.

In Chapter 3, we summarize the evolution of the most abundant oxidized nitrogen species across 17 fresh smoke plumes with physical ages ranging from $\sim$1 to $\sim$6 hours, sampled during WE-CAN. We provide case studies of two particularly well-sampled smoke plumes and discuss observed differences in NO_x partitioning between these fires. We also summarize NO_x partitioning in all the smoke-impacted air masses intercepted during WE-CAN as a function of altitude and relative chemical age. Finally, we compare observations of smoke mixed with urban emissions from the California Central Valley with prior observations in this region.

In Chapter 4, we summarize the Cross Track Infrared Sounder (CrIS) PAN retrieval collected over a portion of summer 2018 North American wildfire season (24 July 2018 to 13 September 2018) coinciding with WE-CAN. CrIS has flown on the Suomi National Polar-orbiting Partnership (Suomi NPP) since 2011. CrIS offers an opportunity to continue and substantially expand the PAN observational record established by the Tropospheric Emission Spectrometer (TES). CrIS offers improved spatial coverage, lower instrument noise, and an improved detection limit. Existing *in situ* measurements of PAN within wildfire plumes from surface sites or airborne platforms (e.g., [39], [40], [4], [13], [41], [42], [43], [44]) cover a relatively limited number of plumes, often do not provide information over the full spatial extent of individual plumes (*i.e.,* extending from the source fire downwind), and provide limited temporal coverage (*i.e.,* observations are campaign-based, covering weeks to months). New satellite observations of PAN offer a complementary perspective, overcoming some of the limitations associated with *in situ* observations. PAN observations from TES on the Aura satellite demonstrate that satellite-measured PAN enhancements over North American are often (15 - 32% of the time) associated with smoke plumes during summer months, specific instances of elevated PAN can be connected to specific fire complexes, and that within-plume enhancements ratios of PAN relative to carbon monoxide (CO) fall within the range calculated from *in situ* observations ([45]).

Chapter 2

Methods

2.1 Overview of WE-CAN flights and pseudo-lagrangian sampling strategy

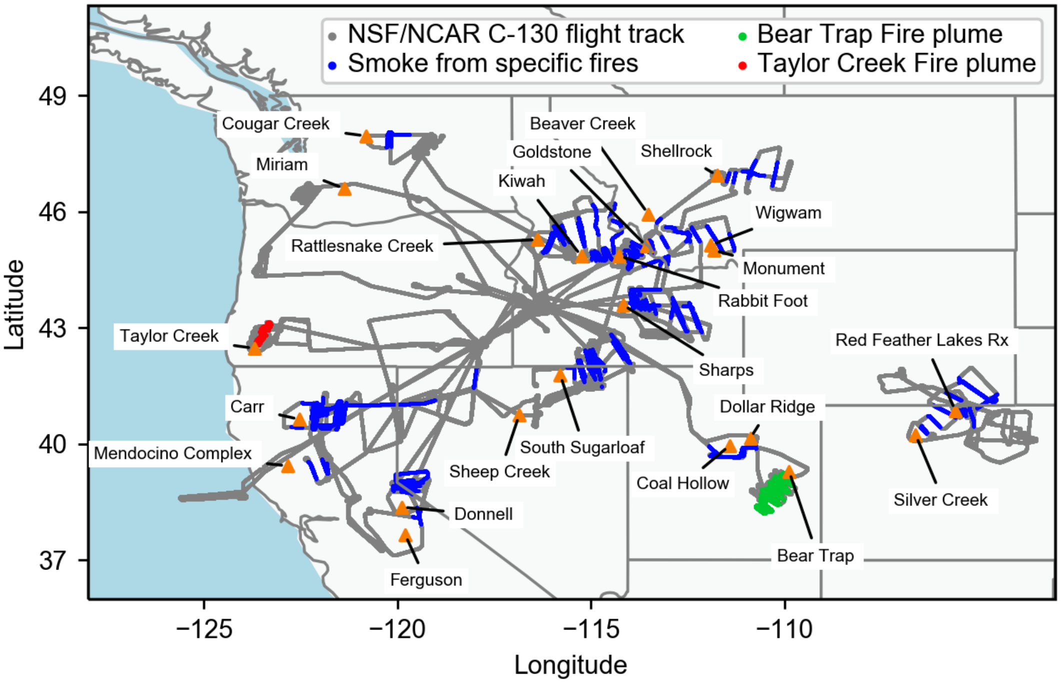

Figure 2.1: Flight tracks during WE-CAN (grey) with plume transects associated with specific, identifiable near-field fires (orange triangles) plotted in blue lines. Green and red lines indicate flight segments associated with smoke from the Bear Trap and Taylor Creek Fires, respectively.

In summer 2018, WE-CAN deployed the NSF/NCAR C-130 to answer questions related to the chemical evolution of reactive nitrogen emitted from wildfires, cloud-smoke interactions, and absorbing aerosols (https://www.eol.ucar.edu/field_projects/we-can). There were a total of 16 research flights (RF) based out of Boise, ID and 3 educational flights (EF) based out of Broomfield, CO. WE-CAN sampled smoke plumes from 23 fires with identified locations, as well as smoke impacted air masses, and cloud-smoke mixtures. A pseudo-lagrangian sampling strategy was attempted for smoke plumes from fires with an identified location using wind speed and wind direction to spatially and temporally position the aircraft to intercept the same portion of the smoke plume as it was transported downwind. The pseudo-lagrangian sampling strategy normally began by characterizing the background air upwind of the fire source. From here the aircraft traversed the smoke plumes perpendicular to the wind direction and downwind of the fire source in an 'S' or 'lawn-mower' pattern as shown in Figure A.1. The timing and location of each intercept was executed with the goal of intercepting portions of the smoke that had already been sampled upwind, i.e. additional time was often spent outside of the plumes because the aircraft speed is typically much faster than the mean wind speed carrying a given smoke plume. The first transect was performed as close to the fire as safety and logistical constraints allowed (6 - 48 km from the fire centroid). Background composition was also measured during turns between plume transects. This sampling strategy was repeated multiple times downwind of the plume.. The distance of the aircraft from the fire source and the wind speed and direction were used to determine a physical age for each plume transect. During WE-CAN, the aircraft sampled downwind of targeted fresh smoke plumes with estimated physical ages as young as 20 min and as old as 10 hours between 2.2 and 6.1 km above sea level (ASL). Given the focus on near-source aging, the dataset is more robust for smoke plumes with physical ages spanning 20 minutes to 6 hours. The aircraft also intercepted air masses impacted by smoke from various unidentified sources in transit (shown in Figure 2), and we analyzed this data as a function of estimated chemical age and altitude. The WE-CAN campaign additionally targeted cloud-smoke mixtures. Given that some of the reactive nitrogen instruments were not able to collect data during these time periods, we have excluded these from our analysis.

2.2 Instrument Descriptions

The WE-CAN payload included instrumentation to measure a large suite of gas-phase and aerosol-phase compounds. In this study, we use the following observations: NO and NO_2 measured using the NCAR 2-channel chemiluminescence instrument; PAN and peroxypropionyl nitrate (PPN) measured using the NCAR PAN-I-CIMS instrument; HONO, HNO_3, gas phase organic nitrates, and gas phase nitro aromatics measured using the University of Washington (UW) I-CIMS; oxidized nitrogen-containing volatile organic compounds (NVOCs) (*i.e.,* nitromethane, nitroethane, nitropropanes, nitrofuran, nitrotoluene) measured using the University of Montana (UM) proton-transfer-reaction time-of-flight mass spectrometer (PTR-ToF-MS), and particulate nitrate ($p$$NO_3$) measured using the CSU high-resolution time-of-flight aerosol mass spectrometer (AMS). C_1-C_5 alkyl nitrates have been quantified by the NCAR Advanced Whole Air Sampler (AWAS) for the transects closest to the fires ([46]). They contribute a small fraction of the total measured NO_y and are not yet quantified for all smoke-impacted samples, so they are not included here. This is consistent with prior observations. For example, Singh et al. ([47]) report on measurements of total NO_y and the most abundant components of NO_y (*i.e.,* NO_x, HNO_3, PANs, alkyl nitrates) during the ARCTAS campaign. C_1-C_5 alkyl nitrates comprise a small fraction (<10%) of the total measured NO_y. We use carbon monoxide (CO) as a fire tracer. CO was measured by two different instruments: the NCAR QC-TILDAS and the NCAR Picarro. VOCs were used to estimate the chemical age of the smoke and identify air masses influenced by urban emissions. The VOCs used in this analysis (2-methylfuran, acrolein, acrylonitrile, 2,2,4-trimethylpentane, tetrachloroethene, chloroform, HFC-134a, and HCFC-22) were measured by the NCAR Trace Organic Gas Analyzer (TOGA). The WE-CAN payload did not include a direct NO_y measurement. In this study, $\sum NO_y$ refers to the sum of NO, NO_2, PAN, PPN, HONO, HNO_3, pNO_3, NVOCs, and Org $N_{(g)}$. The following sections describe the instrumentation listed above. Table 2.1 shows a summary of the instrument technique, uncertainties, detection limit, and PI information for each of the individual components of $\sum NO_y$.

Table 2.1: Instrument details and contact information for measurements used in Chapter 2.

Molecule(s)	Instrument	PI, Contact, Institution, Reference	Detection Limit, Uncertainty
CO	QC-TILDAS	Teresa Campos, campos@ucar.edu, NCAR, (Lebegue et al., 2016)	100 pptv, 0.6 ppbv
CO	Picarro	Teresa Campos, campos@ucar.edu, NCAR	30 pptv, NA
NO	2-channel chemiluminescence	Andy Wienheimer, wein@ucar.edu, NCAR, (Ridley and Grahek, 1990)	100 pptv, 6%
NO_2	2-channel chemiluminescence	Andy Wienheimer, wein@ucar.edu, NCAR, (Ridley and Grahek, 1990)	140 pptv, 12%

Table 2.1: Instrument details and contact information for measurements used in Chapter 2.

Molecule(s)	Instrument	PI, Contact, Institution, Reference	Detection Limit, Uncertainty
HONO	I-CIMS	Joel A. Thornton, joelt@uw.edu, University of Washington, (Lee et al., 2014)	20.5 pptv, 30%
HNO_3	I-CIMS	Joel A. Thornton, joelt@uw.edu, University of Washington, (Lee et al., 2014)	13.5 pptv, 30%
Org $N_{(g)}$	I-CIMS	Joel A. Thornton, joelt@uw.edu, University of Washington, (Lee et al., 2014)	NA, Factor of 2
PAN	PAN-I-CIMS	Frank Flocke, ffl@ucar.edu, NCAR, (Zheng et al., 2011)	20 pptv, 12%

Table 2.1: Instrument details and contact information for measurements used in Chapter 2.

Molecule(s)	Instrument	PI, Contact, Institution, Reference	Detection Limit, Uncertainty
PPN	PAN-I-CIMS	Frank Flocke, ffl@ucar.edu, NCAR, (Zheng et al., 2011)	20 pptv, 12%
pNO$_3$	HR-ToF-AMS	Delphine Farmer, delphine.farmer@colostate.edu, Colorado State University, (Bahreini et al., 2016)	$<$0.12 ug m^{-3}, 35%
NVOC	PTR-ToF-MS	Lu Hu, lu.hu@mso.umt.edu, of Montana, (Sekimoto et al.,2017)	NA, 50%
2-methylfuran	TOGA	Eric Apel, apel@ucar.edu, NCAR, (Apel et al., 2013)	5 pptv, 20%

Table 2.1: Instrument details and contact information for measurements used in Chapter 2.

Molecule(s)	Instrument	PI, Contact, Institution, Reference	Detection Limit, Uncertainty
acrolein	TOGA	Eric Apel, apel@ucar.edu, NCAR, (Apel et al., 2013)	0.5 pptv, 30%
acrylonitrile	TOGA	Eric Apel, apel@ucar.edu, NCAR, (Apel et al., 2013)	1 pptv, 50%
2,2,4-trimethylpentane	TOGA	Eric Apel, apel@ucar.edu, NCAR, (Apel et al., 2013)	0.5 pptv, 15%
tetrachloroethene	TOGA	Eric Apel, apel@ucar.edu, NCAR, (Apel et al., 2013)	0.5 pptv, 15%

Table 2.1: Instrument details and contact information for measurements used in Chapter 2.

Molecule(s)	Instrument	PI, Contact, Institution, Reference	Detection Limit, Uncertainty
chloroform	TOGA	Eric Apel, apel@ucar.edu, NCAR, (Apel et al., 2013)	1 pptv, 15%
HFC-134	TOGA	Eric Apel, apel@ucar.edu, NCAR, (Apel et al., 2013)	1 pptv, 50%
HCFC-22	TOGA	Eric Apel, apel@ucar.edu, NCAR, (Apel et al., 2013)	1 pptv, 50%

2.2.1 NCAR PAN-CIMS

A thermal dissociation chemical ionization mass spectrometer (CIMS) was used to measure PAN and PPN ([48], [49]). In the instrument inlet, PANs in ambient air are decomposed into NO_2 and the parent peroxy acyl (PA) radical at a temperature of 150 °C. The latter reacts with iodine ions produced from trifluoroiodomethane (CF_3I) in a static ionizer cartridge in a flow tube controlled to a pressure of 20 Torr. A quadrupole mass spectrometer detects the produced acylate ions. A known amount of isotopically labeled ^{13}C-PAN is added to the aircraft inlet to perform continuous calibrations.

2.2.2 UW I-CIMS

The UW high-resolution chemical ionization time-of-flight mass spectrometer using iodide-adduct ionization (I-CIMS; [50], [51]) was used to measure HNO_3, HONO, and a suite of other oxidized organic and inorganic gases. Ambient air was sampled at 20 lpm through a straight $\sim$50 cm length (0.75 in OD) PTFE Teflon tube. In order to minimize the influence of the tubing walls on the measurements and to characterize the remaining wall effects, the air was then subsampled at 2 slpm into a custom ion-molecule reaction (IMR) inlet ([52]). The mass spectrometer simultaneously measured hundreds of molecular formulas at 2 Hz time resolution and with a mass resolving power of approximately 5000. Water vapor was continuously added to the IMR in order to maintain relatively constant water vapor concentrations and minimize the effects of water vapor dependence on the ionization process. The IMR background signal was measured for 6 s each 1 min by overflowing the IMR with clean N_2 gas. The tubing background signal was also measured for 15 s every 15 mins. HNO_3 and HONO were each calibrated in the laboratory before and after WE-CAN deployment. Calibration factors and details specific to the WE-CAN deployment can be found in Peng et al. ([14]), but in general are similar to those reported previously ([51], [50]). Gas phase organic nitrogen-containing species measured by the I-CIMS were identified as any species containing nitrogen, two or more carbon atoms, and three or more oxygen atoms. The I-CIMS does not provide information on molecular structure or functional groups, but for this range of molecular formulas iodide-adduct ionization is most likely to be sensitive to multifunctional organic nitrates, peroxy nitrates, and/or peroxyacyl nitrates ([53]). Multifunctional oxidized amines cannot be ruled out but are expected to be minor. Multifunctional nitroaromatic species are also included in this group, however they comprise a small fraction (<1%) of total gas phase mass measured in this category. For these reasons and for simplicity, we refer to the sum of these I-CIMS measurements as gas phase organic nitrates. Since it is not feasible to individually calibrate for each organic nitrate species (or to determine their isomeric structures), we provide an estimate of the combined abundance of gas phase organic nitrate species by assigning a calibration factor of 5 normalized counts per second (ncps) per ppt of analyte for all organic nitrates measured by the I-CIMS. This number was chosen as an estimate of the average sensitivity for this group of compounds, based on the range of sensitivity values of calibrated gases during WE-CAN. We estimate a factor of 2 uncertainty on the absolute concentration of the sum of organic nitrates, although the trend within a plume over time is much less uncertain.

2.2.3 NCAR CO/N_2O/CO_2/CH_4

CO was measured with a commercial Mini-TILDAS tunable diode laser infrared absorption spectrometer (Aerodyne Research; [54]). 1-sigma precision for CO is 100 ppt. A Picarro G-2401-m analyzer was used for the measurement of CO_2 and CH_4, which also provided an additional, but lower precision, measurement of CO. Stated 1-sigma precision for the Picarro is 200 ppb, 2 ppb, and 30 ppb for CO_2, CH_4, and CO, respectively. During the flights, regular calibrations were done by overflowing the inlet with a known mixture of the measured gases in ultra zero air.

2.2.4 NCAR NO_x/O_3

An NCAR 2-channel chemiluminescence instrument was used to measure NO and NO_2. Integrated with these instruments was a NCAR single-channel chemiluminescence instrument that measured O_3. These instruments share an inlet, pumping system, data acquisition system, and power supplies. NO is measured through its chemiluminescent reaction with a flow of reagent O_3, generated on board ([55]). Photons from resulting excited NO_2 are counted with a dry-ice-cooled photomultiplier tube to provide the primary signal. NO_2 is measured in a separate sample flow as an increase in NO following photolysis of NO_2 by 400 nm light-emitting diodes (LEDs). Periodic calibrations of the NO and NO_2 channels were performed during the flights. Two flows from a compressed gas calibration standard of NO in N_2 were used. One of the flows had O_3 added in order to convert NO to NO_2 for the calibration of the NO_2 conversion efficiency by the LEDs. Data are reported at 1 Hz, though the time response of the NO_x channels is somewhat slower than this. At high mixing ratios, the uncertainties are 6% for NO and 12% for NO_2.

2.2.5 CSU AMS

pNO$_3$ submicron non-refractory aerosol mass was measured by a high-resolution time-of-flight aerosol mass spectrometer (HR-TOF-AMS; Aerodyne, Inc; [56]) equipped with a pressure controlled inlet ([57]). Detailed description of the operation of this instrument and data processing during WE-CAN can be found in Garofalo et al. ([58]). The time resolution for the measurements is 5 s. Accuracy (2 σ) for inorganic species is estimated to be 35% ([59]). Given the nature of electron ionization, organic nitrates will fragment to NO_x^+ ions in the AMS, and thus may contribute to the reported pNO$_3$ ([60]).

2.2.6 NCAR TOGA

TOGA, the Trace Organic Gas Analyzer, is a fast online mass spectrometer gas chromatograph instrument ([61], [62]) that was used to measure a wide range of VOCs, some of which are used here. During WE-CAN, TOGA had a sample collection time of 28 s every 100 s for the first 11.5 research flights, and then transitioned to a 33 s sampling time every 105 s for the remainder of the research flights.

2.2.7 UM PTR-ToF-MS

VOC measurements were made with a proton-transfer-reaction time-of-flight mass spectrometer (PTR-ToF-MS 4000, Ionicon Analytik, Innsbruck, Austria). Briefly, atmospheric VOCs with a proton affinity higher than that of water (>165.2 kcal/mol) are ionized via proton-transfer reaction with H_3O^+ ions, and subsequently separated and detected by a time-of-flight mass spectrometer. PTR-ToF-MS measured ion m/z from 15–400 at 2 or 5 Hz frequency during WE-CAN. Ambient air was drawn to the instrument at 10–15 lpm via a $\sim$3 m 1/4" O.D. PFA tube at $\sim$55 °C, and then subsampled by the instrument though a $\sim$100 cm 1/16" O.D PEEK tube at 60 °C, resulting in less than 2 seconds for inlet residence time. Instrument background was checked in flight $\sim$hourly.

Dynamic dilution of certified gas standard mixtures containing 25 VOCs including acetonitrile was used to perform calibrations 3 times each flight (Apel-Riemer Environmental Inc., Miami, FL). For ions not directly calibrated, sensitivities were estimated based on their molecular properties as described by Sekimoto et al. ([63]). Measurement uncertainties for the 25 directly calibrated VOCs are $\sim$15%; for the remaining compounds including many NVOCs the uncertainty is estimated to be < 50%. Detection limits are species-specific and with the range of 50–250 pptv for VOCs with direct calibrations ([64]).

2.3 Identification of Plumes

2.3.1 Identification of fresh smoke plumes from identified fires and physical aging

The plume transects shown in Figure 2.1 are associated with known fires and based on visual identification of sharp increases in CO mixing ratios in time series plots; CO is a common fire tracer with a summertime lifetime of at least 10 days ([65]). We define the core of each plume as the portion of that plume transect where CO is above the 75^{th} percentile for that crossing. We define a transect-specific background as the period when CO is below the 5^{th} percentile. During this portion of the WE-CAN sampling, the aircraft always attempted to fully exit the plume before turning around to complete the next transect. We estimate a physical age for each plume transect by dividing the distance of the aircraft to the fire location by the average wind speed of that specific plume crossing. We also estimated a chemical age for all the smoke impacted air masses intercepted during WE-CAN. We discuss this in section 2.3.2. The fire location is defined as the centroid of the active burn area for that day. We note that there are uncertainties in the active burn area location and entrainment. There is also variability in the wind speed 1) that each plume experienced as it rose to the altitude where it was intercepted by the aircraft, 2) along the plume trajectory, and 3) across each sampling transect. Our definition is intended to capture an approximate average physical plume age once a plume is entrained in the mean flow. In total, we identified 213 plume passes from 21 fires using this method.

In Section 3.1, we show results from 147 plume transect from 17 fires with physical ages ranging from 20 minutes to 6 hours. This analysis includes 9 research flights (RF03, RF04, RF06, RF07, RF09, RF10, RF11, RF13, and RF15) which had complete data coverage for the individual NO_y components. We present the results as the partitioning of the normalized excess mixing ratio (NEMR) of the NO_y component species as a function of estimated physical age. The NO_y NEMR is defined as the sum of the enhancements of the individual NO_y species divided by the CO enhancement. We use NEMR in order to present a dilution-corrected view of the evolution of NO_y across all the plumes sampled during WE-CAN.

In Section 3.2, we present two case studies of specific smoke plumes. These plumes are associated with the Bear Trap (RF09) and the Taylor Creek (RF03) Fires. These plumes are interesting because the majority of the reactive nitrogen emissions from the Bear Trap Fire were in a reduced form (as seen for most fires sampled during WE-CAN), while the Taylor Creek Fire emitted more oxidized forms of reactive nitrogen than other fires in the WE-CAN data set ([46]). The smoke plumes from these two fires were each sampled in pseudo-lagrangian fashion twice, and as such they represent the most successful attempts at pseudo-lagrangian sampling during WE-CAN with $\sim$20 individual plume transects each.

2.3.2 Aged smoke identification and chemical aging

Smoke impacted air masses intercepted during transit, as well as smoke plumes from identified sources were also grouped by altitude (reported in km ASL) and by an approximate chemical age using three co-sampled VOCs, for which OH is likely the dominant sink, with different 2^{nd}-order reaction rate constants for loss via reaction with OH: 2-methylfuran, acrolein and acrylonitrile. These three VOCs, quantified by TOGA, were selected for assigning chemical age because they have high in-plume concentrations and their reaction rates with OH span a broad range. We have used the TOGA data for this analysis because TOGA has a lower detection limit for these species than the PTR-ToF-MS. We assign chemical ages to each of the smoke-influenced observations shown in Figure 2.2 according to the definitions given in O'Dell et al. ([66]). Briefly, observations

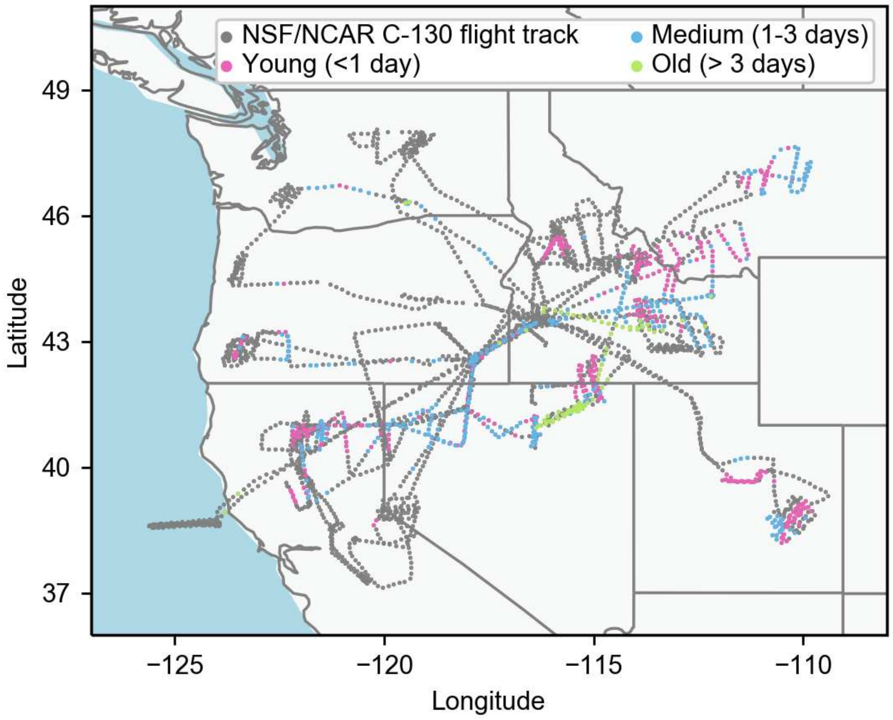

Figure 2.2: WE-CAN flight tracks colored by estimated plume chemical age on the TOGA instrument time resolution of an approximate 30-second sampling time with a 72-second gap between observations.

corresponding to CO > 85 ppbv, HCN > 275 pptv and acetonitrile (CH_3CN) > 200 pptv are defined as smoke-influenced. The chemical age is defined according to a combination of the observed levels of 2-methylfuran, acrolein, or acrylonitrile. Smoke is categorized as 'young' (< 1 day of aging) when 2-methylfuran > 0.5 ppt (mean non-smoke background + 1 standard deviation). Smoke is categorized as 'medium' (1-3 days of aging) when 2-methylfuran is not elevated but acrolein is > 4.2 ppt (mean non-smoke background + 1 standard deviation). Smoke is categorized as 'old' (> 3 days of aging) when neither 2-methylfuran nor acrolein are elevated, but acrylonitrile is > 2.1 ppt (mean non-smoke background + 1 standard deviation). The 'old' category also includes the few samples (7) when none of the VOC age tracers, (*i.e.,* 2-methylfuran, acrolein or acrylonitrile) are elevated, but CO, HCN and CH_3CN are elevated (> 85 ppbv, 275 pptv, and 200 pptv respectively). Samples where one of the fire tracers or the VOCs used for the aging were missing were excluded from this analysis. Limitations of using these species for chemical aging include: fast reaction of 2-methylfuran with NO_3 ([67]), which would reduce the quantitative age assigned to the 'young' and 'medium' categories, and the chemical production of acrolein from alkenes, believed to be minimal compared to direct emissions of acrolein from fires ([62]). O'Dell et al. ([66]) shows that 2-methylfuran is highly reactive with NO_3. Therefore NO_3 chemistry in the dark core of the plume or during nightime can decrease the age associated with the 'young' and 'medium' plumes. However, the OH concentration assumptions and the role of dominant sinks for each age tracer would only impact the quantitative ages associated with smoke impacted air masses, but not the qualitative 'young', 'medium', 'old' categories assigned to each of them. Samples with urban influence are removed using elevated anthropogenic tracers (measured by TOGA) such as 2,2,4-trimethylpentane (a fuel additive) (> 20 pptv), tetrachloroethene (used in dry-cleaning and as a metal degreasing agent) (> 2 pptv), HFC-134a (a refrigerant) (> 125 pptv), or HCFC-22 (refrigerant) (> 275 pptv) (ATSDR, EPA, [68]).

We acknowledge that the O'Dell et al. ([66]) method of assigning approximate chemical age is sensitive to both variability in emissions from fires and dilution. Dilution effects could cause the mis-placement of younger, dilute smoke into an older category. O'Dell et al. ([66]) explore the potential impacts of dilution on age assignment to show that the distribution of dilution-corrected tracers is similar to the non-dilution-corrected tracer distributions, and that age uncertainties are unlikely to significantly impact our conclusions. We also note that all measurements are averaged over the TOGA sampling time, and TOGA collection times can encompass both smoke-impacted and background conditions or steep gradients in concentration. This can impact our assignment of chemical ages used here, and it is particularly relevant for narrow plumes.

2.4 CrIS PAN observations

The Suomi NPP satellite is on a sun-synchronous Earth orbit (512 miles above the surface) with overpass times around 1:30 and 13:30 local time (LT), completing 14 orbits around the planet every day. CrIS is a nadir viewing Fourier transform spectrometer (FTS) that measures thermal infrared radiances with high spectral resolution (0.625 cm^{-1}). CrIS PAN provides an opportunity to continue the satellite record of PAN established by TES, and while the two retrievals are linked, there are several important differences. TES PAN retrievals rely on the PAN absorption feature at 1150 cm^{-1}, a region not covered by CrIS. However, an approach that uses the PAN absorption feature at 790 cm^{-1} was recently developed to retrieve PAN from CrIS spectra. The CrIS PAN retrieval algorithm was built on capabilities of the Multi-Species, Multi-Spectral, Multi-Satellite (MUSES) retrieval software ([69]), which builds on the optimal estimation algorithm developed for Aura-TES ([70], [71]). The retrievals used in this thesis were done by Drs. Vivienne Payne and Susan Kulawik at the NASA Jet Propulsion Laboratory (NASA JPL). The retrievals were received by CSU in December 2019 via a direct transfer to our computing cluster (Ozone). A validation of this product is ongoing using Atmospheric Tomography Mission (AToM) vertical profiles; this validation is being led by Dr. Vivienne Payne (JPL). Compared to TES, CrIS offers improved spatial coverage and lower instrument noise. The latter has a direct impact on the CrIS PAN detection limit. Simulations suggest that the single footprint detection limit for CrIS PAN is < 0.15 ppbv.

The retrieval algorithm produces observation operators (averaging kernels) for each individual retrieval. The averaging kernels represent the sensitivity of that retrieval to the true state and the a priori. This sensitivity varies by altitude, and it depends on the surface characteristics, atmospheric temperature, and cloud cover. Figure 2.3 shows the CO (Figure 2.3a) and PAN (Figure 2.3c) averaging kernels from retrievals on 20 August 2018 associated with the Mendocino Complex smoke plume (39° - 43° N, 115° - 123° W). Figures 1b and 1d show the a priori (black) used in the retrieval algorithm and the retrieved vertical profiles (shades of pink) colored by their corresponding tropospheric averages for CO and PAN, respectively. In general, CrIS is most sensitive to PAN in the free troposphere (> 680 hPa) (Figure 2.3c) and its sensitivity decreases rapidly near the surface. CrIS PAN retrievals have $\sim$1 Degrees of Freedom for Signal (DOFS), which represents the independent pieces of vertical information. Thus the retrievals do not provide information about the vertical distribution of PAN. This is apparent in the vertical PAN profiles in Figure 2.3d, where there is little variation in the mixing ratios of PAN along the vertical within a specific retrieval. For this analysis, we largely present a tropospheric average for each PAN retrieval. This is defined as the average retrieved PAN between 800 hPa and the tropopause.

CrIS CO is also retrieved using the MUSES algorithm at the 2169 cm^{-1} spectral feature. Note that the averaging kernel values are higher for CO than PAN (Figure 2.3a and Figure 2.3c) meaning that CrIS is more sensitive to tropospheric CO than PAN. As shown in Figure 2.3a the sensitivity of CrIS to CO peaks at the 680 and 510 hPa pressure levels. CrIS CO has >1 DOFS, and thus the retrievals provide some additional information about the vertical distribution of CO. See section 4.1.

For the analysis presented below, we include retrievals that fulfill the following criteria: tropospheric column average for PAN $>$0.1 ppbv and $<$2 ppbv, and tropospheric column average of CO $<$4000 ppbv. The lower threshold for tropospheric PAN was selected based on the estimated limit of detection ($\sim$0.15 +/- 30%). During data inspection, we noticed elevated PAN and CO in individual retrievals that were not consistent with the surrounding atmospheric composition (textiti.e., low PAN/CO). The upper PAN and CO thresholds chosen are above the 99th percentile of

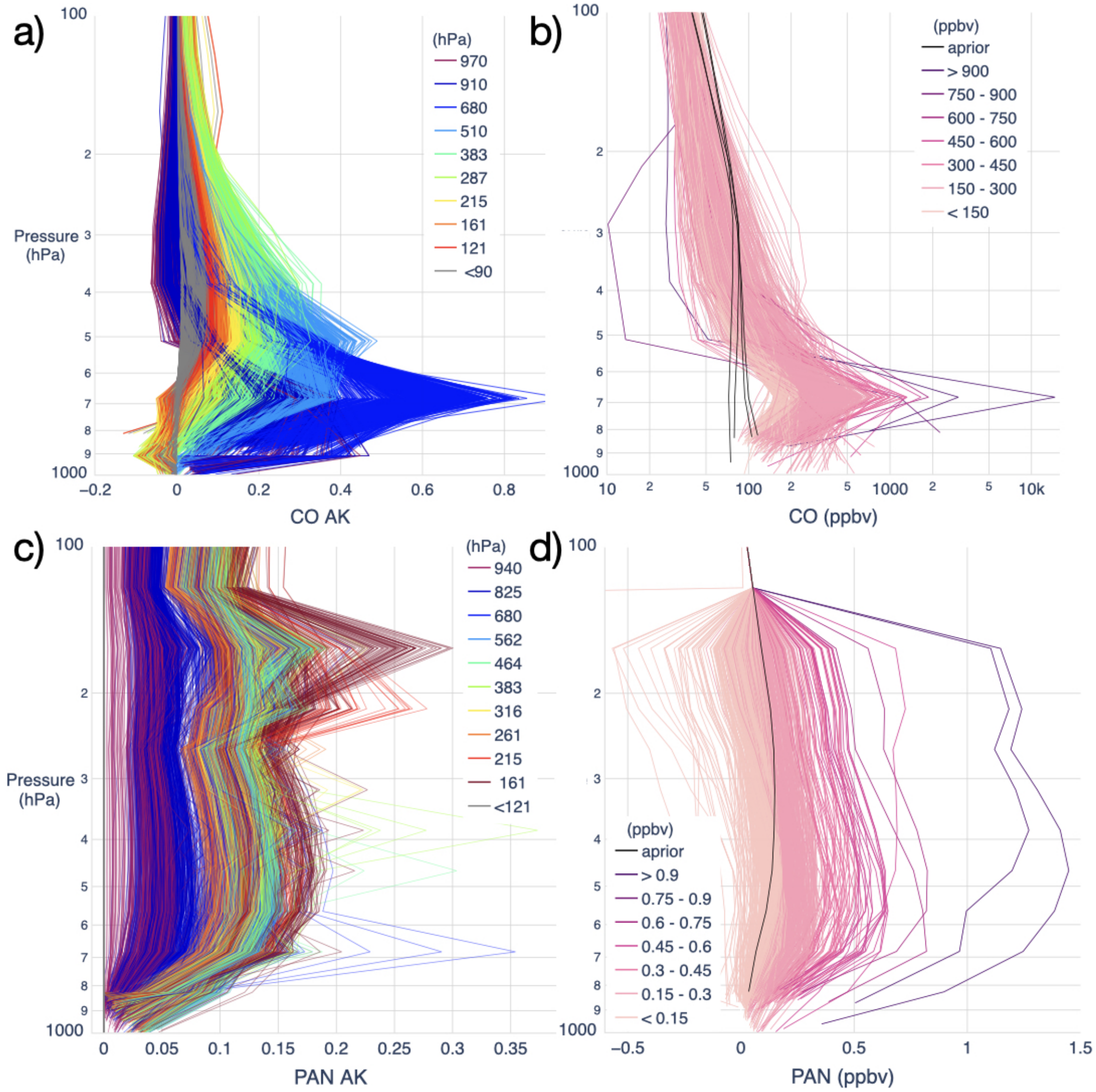

Figure 2.3: a) CrIS CO averaging kernels and b) retrievals over the western U.S. (39 - 43 °N, 115 - 123 °W) on 20 August 2018. Averaging kernels are colored by their corresponding pressure level, and retrievals are colored by the tropospheric average mixing ratio. (c) Corresponding PAN averaging kernels and d) retrievals. There is one prior profile for the entire study region based on a GEOS-Chem simulation described in Payne et al. ([72]) and [42]

distribution for the entire set of PAN and CO retrievals. There is on-going work to identify the reason for such elevated retrievals.

2.5 NOAA Hazard Mapping System (HMS) Fire and Smoke Product

We use the NOAA Hazard Mapping System (HMS) to identify smoke-impacted CrIS retrievals. HMS is a smoke-mapping tool from the National Environmental Satellite, Data and Information Services (NESDIS) in support to the National Oceanic and Atmospheric Administration (NOAA) and the National Weather Service (NWS) efforts to build an operational air quality forecast capability ([73]). Using visible imagery from seven NOAA and National Aeronautics and Space Administration (NASA) satellites, trained satellite analysts generate a daily operational list of fire locations and outline areas of smoke (Ruminski, 2006). The use of geostationary satellites (GOES-11 and GOES-12) allows for continuous coverage over North America. When the smoke plumes are detected, the analysts do not differentiate between wildfires and agricultural/prescribed fires. Thus the dataset contains smoke from both types of fires. Due to the nature of smoke detection by HMS, clouds are an important interference during the detection and validation of the HMS products ([73]). Smoke detections are manually inspected, and contours are drawn depicting and approximate smoke concentrations (5, 16, and 27 ug m-3, i.e., light, moderate, and dense contours). Smoke concentrations are estimated using the Aerosol Optical Depth (AOD) estimates from the Geostationary Operational Environmental Satellite (GOES) Aerosol Smoke Product (GASP) which assumes a mass extinction coefficient for smoke below 5 km. The vertical location of the smoke is not provided ([74]). The false alarm rate for fire detection is $\sim$2% ([75]). Dilute smoke is particularly challenging to visually identify as it can mix with anthropogenic haze. This results in a conservative estimate of smoke detection and extent from the HMS dataset ([76]). In this work, we use archived HMS files with a 0.2° x 0.5° horizontal grid resolution that provide the maximum smoke concentration value for a given location in a given day.

2.6 HYSPLIT Trajectories

We use the Hybrid Single Particle Lagrangian Integrated Trajectory (HYSPLIT) model (Draxler and Hess,1998) to estimate the origin and age of a small subset of smoked plumes detected by CrIS. For this application, the HYSPLIT model uses the North American Regional Reanalysis (NARR) meteorological product. NARR has a time step of 3 hours, a grid spacing of 32 x 32 km, and 23 vertical layers between the surface and 100 hPa. We initialized a set of forward and backward trajectories for a period of 24 hours at the locations of smoke-impacted CrIS retrievals. All trajectories were initialized at 720, 600 and 495 hPa levels. Details on the time and location that each trajectory was initialized are detailed in Section 4.3

Chapter 3

Daytime Oxidized Reactive Nitrogen Partitioning in Western U.S. Wildfire Smoke Plumes

3.1 Summary of $\sum \mathrm{NO}_y$ Partitioning in Near-Source Wildfire Plumes

Figure 3.1 shows a summary of quantified specific individual components of NO_y as a function of physical age in 147 smoke plume intercepts from 17 western U.S wildfires sampled during WE-CAN. The plumes shown in Figure 3.1 were largely sampled above 3 km ASL with the exception of three plume transects from the Cougar Creek Fire (RF06) intercepted at lower altitudes (2.5 - 2.9 km ASL). The average temperature and altitude for each age category is shown on the top of the figure with the corresponding standard deviation in parentheses. We refer here to this particular subset of NO_y species as $\sum \mathrm{NO}_y$. Also note that the number of transects is largest closer to the fire; reflecting the scientific foci of WE-CAN as well as aircraft duty limitations. Figure 3.1 shows that NO_x is depleted quickly in large smoke plumes. On average after 3 hours, NO_x contributes only 4 - 7% of $\sum \mathrm{NO}_y$. Several studies have also observed the rapid decay of NO_x in wildfire plumes ([15], [77], [78], [79]). This has also been observed in plumes emanating from agricultural fires; Liu et al. ([13]) report that after ∼30 min NO_x NEMRs drop between ∼26% and ∼56%. The average *e*-folding (decay) time and distance for NO_x for the smoke plumes sampled during WE-CAN and shown in Figure 3.1 is approximately 90 minutes of physical age, which corresponds to an average distance downwind of 40 km (Figures Figure A.7 and Figure A.8). The median ratio of NO to NO_2 at the core of the plumes range from 0.11 to 0.24. This ratio varies as a function of time of day, with values > 0.16 observed earlier in the day (*i.e.,* the median ratio is 0.24 before 15:00 MDT) and values < 0.2 observed later in the day as the photolysis rate of NO_2 decreases (*i.e.,* the median ratio is 0.11 after 17:00 MDT) (Figure Figure A.6). HONO is depleted faster than

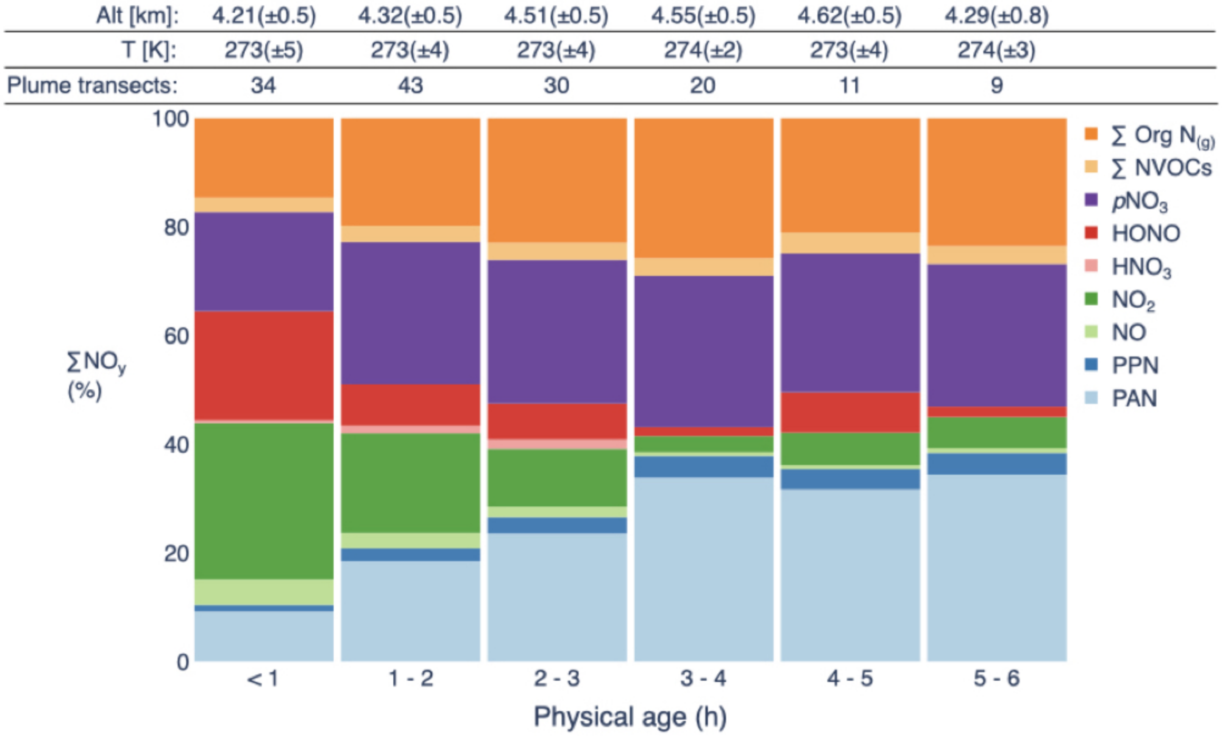

Figure 3.1: Partitioning of $\sum NO_y$ as a function of physical age (h) in the most concentrated cores of western U.S. wildfire smoke plumes sampled in a pseudo-lagrangian fashion during WE-CAN. Each of the plumes included in this figure are associated with a specifically targeted fire (see Figure 2.1). The observations shown here correspond to sampling in the center of the plume, which is defined as the portion of each plume transect where CO is above the 75^{th} percentile of that transect. To calculate the enhancement of each species, a transect-specific background mixing ratio for each individual species is subtracted. Comparable figures for regions of the plume outside the concentrated cores are provided in the Supplementary Information (Figures Figure A.2 and Figure A.3).

NO_x in the fresh plumes sampled during WE-CAN (see Figure 3.2 for specific examples). HONO emissions are sufficiently large to be the dominant OH source in these WE-CAN plumes ([14]).

Averaged across all plumes, approximately 37% of the $\sum NO_y$ is in the form of PANs (PAN and PPN in this case) after 3 hours. The rapid conversion of NO_x to PANs has been observed in several prior field campaigns targeting wildfire smoke. For example, Alvarado et al. ([15]) reported on aircraft observations of boreal smoke plumes and showed that the average percent contributions of PAN to NO_y are 50% and 69% in fresh and aged smoke plumes, respectively. Yokelson et al. ([39]) reported on smoke plumes from a suite of tropical crop residue and deforestation fires. They primarily traced the evolution of the smoke for the first 2 hours of atmospheric aging. On average, they concluded that approximately 17% of NO_y was in the form of PAN following 1.2 to 1.4 hours of aging. Akagi et al. ([4]) reported aircraft observations of a prescribed California chaparral fire. They point out rapid initial growth of the PAN NEMR, based on observed increases of a factor of 10.7 (± 5.3, standard deviation) in the first 4 hours after emission. The rapid production of PAN has also been observed in agricultural fires ([13]). The PAN NEMR relative to NO_y increased from less than 5% to 30% in ∼1 hour; after ∼1.2 hours, PAN accounted for 51 - 74% of the loss of NO_x on a molar basis in a survey of 15 agricultural fires ([13]). Within the first 4 hours following emission in the WE-CAN dataset, PAN accounts for 38% (±11%, standard deviation) of initial NO_x on a molar basis. The average PPN to PAN ratio in the core of the fresh plumes sampled during WE-CAN is 0.12 (± 0.014, standard deviation).

HNO_3 mixing ratios within the center of these plumes, on average, are only slightly enhanced above background mixing ratios during the first 3 hours of physical aging. After this point, the average enhancement of HNO_3 is zero or negative. This means that the background mixing ratio of this species is greater than the mixing ratio in the most concentrated part of the plume. As we show later, HNO_3 is often a substantial fraction of $\sum NO_y$ in lower-altitude, warmer plumes. Trentmann et al. ([80]) used a photochemical box-dilution model to show that the magnitude of the increase in pNO_3 observed during the South African Regional Science Initiative (SAFARI 2000) field experiment could be explained by the uptake of HNO_3 produced by gas-phase chemistry. As suggested by Yokelson et al. ([39]), null or negative HNO_3 enhancements may be due to a rapid reaction of HNO_3 with NH_3 to form particulate ammonium nitrate.The process by which ammonium nitrate forms is mandated by the availability of NH_3 and HNO_3 and it is a strong function of temperature and humidity ([81]). (In the concentrated cores of the WE-CAN plumes, the formation of ammonium nitrate may occur in the aqueous phase as well.) Additionally, Tabazedah et al. ([82]) proposed that biomass burning aerosols can remove HNO_3 in a similar way to sea salt aerosol, by HNO_3 replacing chloride (Cl-) ions or water soluble organic ions such as formate, acetate, and oxalate present in biomass burning aerosols. Several studies have also noted that HNO_3 does not correlate with elevated CO in fresh or aged biomass burning smoke (*e.g.,* [39], [15], [13]).

Figure 3.1 indicates that 18% to 28% of the $\sum NO_y$ is in the form of *p*NO_3 (purple bars in Figure 3.1), and that the evolution in the contribution of *p*NO_3 to $\sum NO_y$ mirrors the evolution of PAN during the first 4 hours. This result suggests rapid formation of *p*NO_3 in the first several hours of physical aging, similar to that observed by Hobbs et al. ([79]). The contribution of *p*NO_3 to $\sum NO_y$ rapidly increases in the WE-CAN dataset from 18% to $\sim$ 26% in the first 2 hours. The *p*NO_3 reported here by the AMS represents both organic and inorganic forms (Section 2.2.5). Work is ongoing to separate the inorganic fraction. Liu et al. ([13]) also observed cases of rapid production of *p*NO_3 in agricultural smoke. They note that the *p*NO_3 in these smoke samples is mostly inorganic (>90%) as indicated by AMS measurements. Alvarado et al. ([15]) report contributions of 24% and 12% of *p*NO_3 to NO_y in fresh and old boreal smoke plumes, respectively. Similarly, Briggs et al. ([43]) report that *p*NO_3 contributed 20 - 69% of the measured NO_y in 23 aged smoke plumes observed over the U.S. Pacific Northwest.

Despite relatively large measurement uncertainties, Figure 3.1 also shows that gas phase organic nitrates may comprise a large fraction (15% - 26%) of $\sum NO_y$. Their collective evolution appears to mirror that of PANs and *p*NO_3, increasing their total contribution to $\sum NO_y$ from 15% to $\sim$23% within 3 hours of physical aging. C_4 and C_5 organic nitrates contribute $\sim$50% of the total abundance (in mixing ratio units); 80% of the total is from C_2-C_6 compounds (Figure Figure A.4). Gas phase nitro aromatics are a small fraction (<1%) of $\sum NO_y$ during WE-CAN; we expect that a dominant portion of the nitrophenolics are in the particle phase. The large contribution of gas-phase organic nitrates to $\sum \mathrm{NO}_y$ in the WE-CAN dataset is not necessarily unexpected based on prior observations indicating that select individual organic nitrates (*e.g.,* methyl peroxy nitrate) are present in smoke plumes intercepted under cold or high altitude conditions ([83]), and model simulations of smoke chemistry require more NO_x loss in the first several hours of plume evolution than can be explained by the formation of PAN or HNO_3 ([40]).

While also more uncertain than many of the other measurements summarized in Figure 3.1, the oxidized NVOCs quantified by the PTR-ToF-MS likely comprise a small and relatively consistent fraction of $\sum \mathrm{NO}_y$ as smoke plumes age. All comparable measurements of NVOCs in smoke are relatively recent. NVOCs comprise a small fraction of measured VOCs (*e.g.,* [84], [85], [86], [87], [88], [89], [24]). For instance, Gilman et al. ([84]) observed that NVOC (including reduced and oxidized forms) are a small fraction (<8%) of the total molar mass of VOC measured during laboratory burns. Methyl nitrite was the only oxidized NVOC reported as a dominant NVOC during these experiments.

We anticipate that the NO_y species presented in this overview analysis comprise the majority of the total NO_y present in the wildfire smoke plumes sampled during WE-CAN. Our approach is different from many past studies in that we quantify $\sum \mathrm{NO}_y$ using individual contributors without a simultaneous NO_y measurement. Other studies that have measured total NO_y (*e.g.,* [90], [43]) have reported that $\sim$80 - 100 % of the NO_y sampled in aged smoke plumes are in the form of peroxy nitrates (PNs), NO_x, $p\mathrm{NO}_3$ and HNO_3. For instance, Singh et al. ([90]) show that PNs, mostly in the form of PAN, comprise 60 - 70% of the total NO_y during ARCTAS-A (spring) and ARCTAS-B (summer) in smoke plumes from boreal fires sampled after 3 - 8 days of aging. Some studies do report on select organic nitrate species. For example, in the smoke plumes sampled during ARCTAS-B and ARCTAS-CARB the total alkyl nitrates (ANs) comprise less than 10% of the measured NO_y. Similarly, Briggs et al. ([43]) report that NO_x, PAN and $p\mathrm{NO}_3$ comprise 77 - 100% of the observed NO_y in 4 wildfires smoke plumes observed over the U.S. Pacific Northwest after 1 - 2 days of aging. Thus, our results are broadly consistent with this prior work.

3.2 Case Studies of NO$_y$ partitioning: Bear Trap (BT) and Taylor Creek (TC) Fires

Figure 3.2 presents the evolution of $\sum$NO$_y$ in two individual smoke plumes emanating from the Bear Trap and Taylor Creek Fires; each of these plumes were repeatedly sampled in a pseudo-lagrangian fashion. For these plumes, we present the absolute values for the NO$_y$ NEMR rather than percentages to investigate $\sum$NO$_y$ mass conservation with time. These plumes demonstrate the variability between different smoke plumes, a perspective that is somewhat masked in the average view presented in Figure 3.1. Proximity to the fire source, sampling altitude, meteorological conditions, modified combustion efficiency (MCE), and OH concentrations varied between these plumes. From Figure 3.2, we can see that the dilution corrected abundance of $\sum$NO$_y$ is conserved with time within the measurement uncertainties.

The Bear Trap Fire plume was sampled at approximately the same altitude for the first ($\sim$4.3 km) and second ($\sim$4.5 km) sampling attempts. Temperature and relative humidity are approximately constant in the plume cores downwind (ΔT < 1K and ΔRH = 9% across the samples included in the upper panel of Figure 3.2). The Taylor Creek plume was much more narrow vertically, and the sampling altitude was less consistent as the mission attempted to intercept the plume at multiple altitudes. Thus, there are 8 near-source transects with a mean estimated physical age of 35 minutes, ranging from 19 to 54 minutes. The sampling altitudes from the second pseudo-lagrangian sampling effort of the Taylor Creek Fire plume encompass a wider range (3.3 - 4.5 km) because this set of intercepts includes a spiral through the plume. This sampling began further downwind; no intercepts represent < 1 hour of physical aging. As a result of these sampling choices, the temperature in Taylor Creek smoke plume intercepts (including the spiral) varies between 274 and 283 K (mean 281 K, $\pm$ 2.2 standard deviation). Within the pseudo-lagrangian sampling pattern (*i.e.,* not the spiral), the temperature varies between 280 and 284 K (mean 282 K, $\pm$ 1.2 standard deviation). The Taylor Creek Fire plume is also the driest smoke plume in the

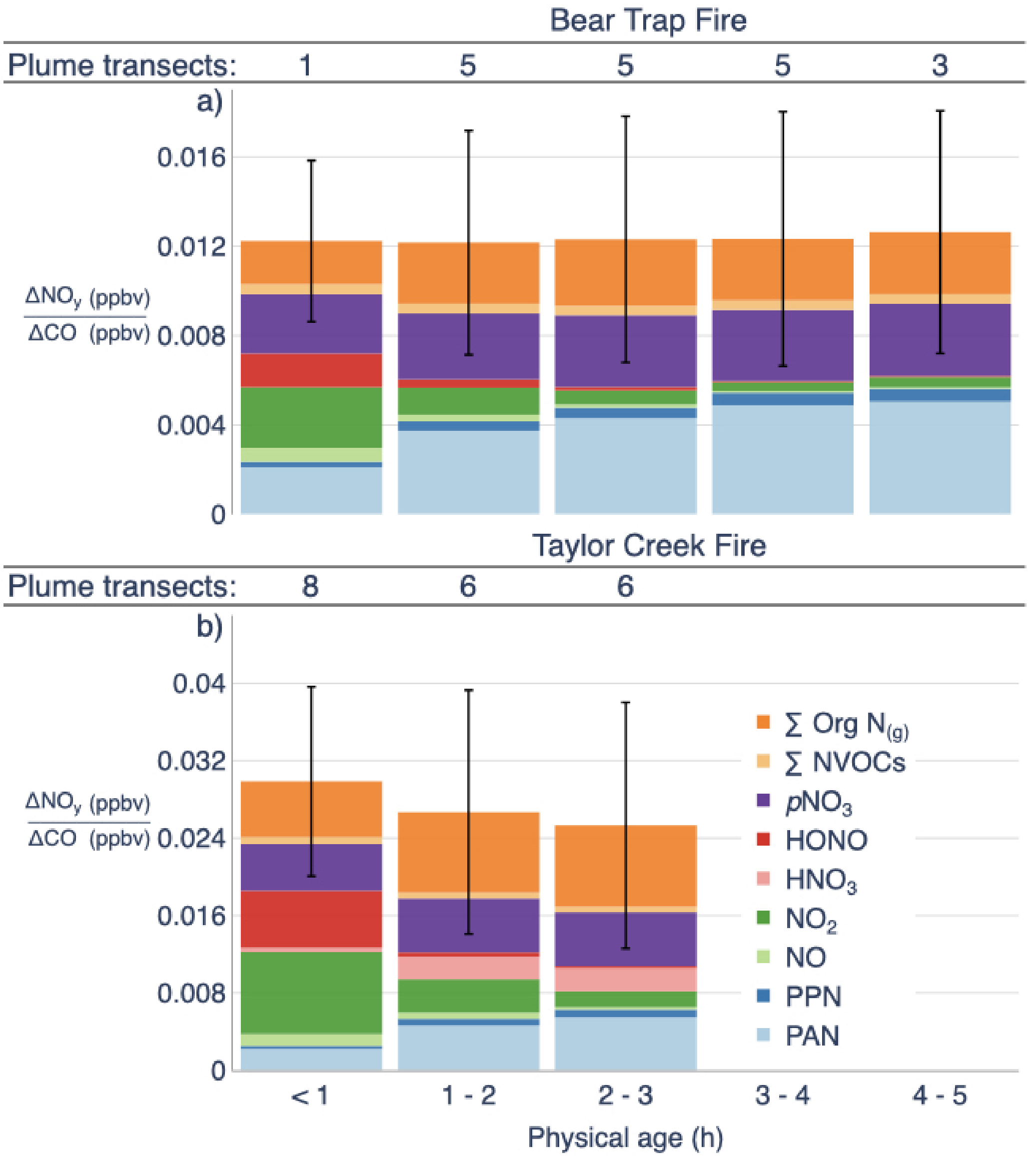

Figure 3.2: Partitioning of the NEMR of $\sum NO_y$ as a function of physical age (h) in the most concentrated cores of the Bear Trap and Taylor Creek Fire smoke plumes sampled during WE-CAN. These smoke plumes were sampled in a pseudo-lagrangian fashion twice. Here we present the average of the plume transects from both samples binned by their corresponding physical age. (See Section 2.3.1 for a discussion of uncertainty in the inputs to the calculation of physical age.) The center of the plume is defined as in Figure 3.1, and a transect-specific background mixing ratio for each individual species was subtracted. The numbers above each bar signify the individual transects through the plume in each physical age bin. Error bars were calculated by adding the individual uncertainty for each NO_y species in quadrature.

WE-CAN dataset (3 < RH < 11 %), thermodynamically favoring the presence of gas-phase nitrate (*i.e.,* HNO_3) over $p$$NO_3$ ([81]) in this smoke plume.

Figure 3.2 shows that, for both smoke plumes, the ratio of HONO to NO_x in the closest sampling passes is between 0.45 - 0.60 (ppbv $ppbv^{-1}$). Within 3 hours, this ratio is less than 0.2 for both plumes, indicating that the photolysis of HONO occurs more rapidly than the overall conversion of NO_x to its oxidation products ([14]). Despite sampling these smoke plumes closer to the source than other fires targeted during WE-CAN, the samples still show substantial conversion of NO_x to its oxidation products in the closest sampling passes to the fire (blue, purple and orange bars in the leftmost columns of Figure 3.1). For instance, in the plume crossing closest to the Bear Trap Fire (physical age $\sim$ 33 min), PANs, $p$$NO_3$ and gas-phase organic nitrates comprise 20%, 22%, and 16% of $\sum NO_y$ measured. These percentages are lower for the closest pass of the Taylor Creek Fire (physical age $\sim$ 20 minutes), which are 4%, 11%, and 12% for PANs, $p$$NO_3$, and gas-phase organic nitrates, respectively. The PAN NEMR increases in the Bear Trap Fire smoke plume through $\sim$3-4 hours of physical aging ($\sim$40% of the $\sum NO_y$). The pattern of $p$$NO_3$ production in this case was different. The $p$$NO_3$ NEMR increases rapidly, and then stabilizes after 2 hours ($\sim$26% of $\sum NO_y$). Similar to the $p$$NO_3$ evolution, the gas-phase organic nitrates NEMR increases rapidly and stabilizes after 2 hours ($\sim$23%), mainly driven by those with 6 or fewer carbon atoms. The detailed partitioning of gas phase organic nitrate across different carbon number groups are shown in Figure A.4 and Figure A.5. For the Taylor Creek plume, we do not have samples out further than $\sim$3 hours of physical aging, but like in the Bear Trap Fire plume, the PAN NEMR increases through $\sim$3 hours of physical aging and the $p$$NO_3$ and gas-phase organic nitrates NEMR stabilize after $\sim$2 hours. By the end of the sampling period, PAN and $p$$NO_3$ account for approximately the same percentage of $\sum NO_y$ ($\sim$22%), and the gas-phase organic nitrates make the largest contribution to $\sum NO_y$ ($\sim$33%).

Liu et al. ([13]) observed similar production rates for PAN and $p$$NO_3$ in the first hour of smoke evolution from 5 individual agricultural fires. Even though these agricultural fires were relatively small, and the smoke was less dense than the plume cores included in Figure 3.2, Liu et al. ([13])

also found that by the end of the sampling periods ($\sim$30 - 50 min) PAN and $p\mathrm{NO}_3$ accounted for approximately the same fraction of the total NO_y. However, they also encountered two fires where a larger fraction of NO_x converted to $p\mathrm{NO}_3$ instead of forming PAN by the end of the sampling period ($\sim$1 h). The evolution of $\Delta p\mathrm{NO}_3/\Delta\mathrm{PAN}$ as a function of physical age for each of the Bear Trap and Taylor Creek smoke plumes can be described with an exponential decay function (Figure Figure A.9). For the Taylor Creek Fire plume, this ratio is $\sim$3 at 30 min and drops to $\sim$0.7 by $\sim$1.5 hours of physical aging. For the Bear Trap Fire, this ratio is slightly > 1 at 30 min and drops to $\sim$0.6 after 4 hours of sampling, signifying faster PAN production. Liu et al. ([13]) report the same ratio as slightly > 1 after 1 hour of physical aging, while Akagi et al. ([16]) and Alvarado et al. ([15]) report $\Delta p\mathrm{NO}_3/\Delta\mathrm{PAN}$ of $\sim$0.75 and $\sim$0.5 in fresh plumes (4 - 10 h) from chaparral and boreal fires, respectively.

Of the two example plumes shown here, the Taylor Creek Fire produced larger emissions of $\sum\mathrm{NO}_y$ relative to CO (0.030 ppbv ppbv^{-1}), more than twice that of the Bear Trap Fire (0.012 ppbv ppbv^{-1}). We calculated the MCE for each fire following Lindaas et al. ([46]). The Bear Trap Fire had an average MCE of 0.88 ($\pm$ 0.017, standard deviation) indicating that the plume contained emissions produced from both smoldering and flaming conditions. This is reflected in the higher relative abundance of reduced forms of nitrogen ([46]). The Taylor Creek Fire had an average MCE of 0.94 ($\pm$ 0.003, standard deviation) indicating that the plume represents more flaming conditions and efficient combustion. This plume has one of the highest MCE of all the plumes sampled during WE-CAN, suggesting emission of more oxidized forms of reactive nitrogen (*i.e.,* NO_x and HONO) and less of reduced forms of reactive nitrogen (*i.e.,* NH_3). Despite the difference in MCE between fires, the relative contribution of $p\mathrm{NO}_3$ to $\sum\mathrm{NO}_y$ is not substantially different between these plumes, as was discussed above. However, distinguishable HNO_3 enhancements (up to 2.1 ppbv) above background were present in the Taylor Creek plume for the duration of the sampling period; HNO_3 accounts for $\sim$10% of $\sum\mathrm{NO}_y$, even after 3 hours of physical aging. Tabazadeh et al. ([82]) and Trentmann et al. ([80]) suggest that an important sink for HNO_3 in plumes is scavenging by particles. Even at an RH of 15% and temperature of 220 K, dust particles contain sufficient liquid water for the displacement of carbonate by NO_3^- ions to occur ([82]). Cl^- replacement by the NO_3^- ion can also occur in smoke plumes as smoke particles have a significant mass fraction of water present ([82]). One potential reason that the Taylor Creek plume contained excess HNO_3 may be because of the simultaneously dry conditions; the scavenging of HNO_3 by particles may not have been as efficient as in other smoke plumes. Additionally, the production of NH_4NO_3 in the smoke plume of the Taylor Creek Fire might have been impacted by other factors. The flaming condition (MCE = 0.94) of this fire resulted in higher emissions of oxidized over reduced forms of reactive nitrogen limiting the availability of NH_3 to form NH_4NO_3 as the plume ages (Jakob Lindaas, personal communication). The abundance of organic and inorganic particulate sulfate (pSO$_4$) is 1-2 orders of magnitude higher in the Taylor Creek Fire plume; thus, sulfate had the potential to impact the free NH_3 initially available in the system to form NH_4NO_3. In this plume, NH_3 enhancements become smaller than HNO_3 enhancements after 2 hours of physical aging, whereas in the Bear Trap Fire plume, the system remains HNO_3 limited for the duration of the sampling. The Taylor Creek Fire plume is a special case among the plumes sampled during WE-CAN given the warmer and drier conditions of the plume, relatively low NH_3 emissions, and high pSO$_4$ abundance, all resulting in positive HNO_3 enhancements.

We estimate an OH concentration for these plumes via two methods. The first method is described by Hobbs et al. ([79]) and de Gouw et al. ([91]). To do this, we assume that the loss rate of the NEMR of toluene and benzene is dominated by reaction with OH (Eq. (A.1) and Figures Figure A.10 and Figure A.11). While this method is grounded in past literature, it is imperfect because of the short timescales of interest here. Our second method is based on prescribing OH to match the observed decay of butene and methyl furans, significantly shorter-lived species with large primary emissions. We know that the actual OH concentration changes rapidly in smoke plumes ([14]), but the average OH concentration for the Bear Trap Fire and Taylor Creek Fire smoke plumes calculated via the first (second) method are 4 x 10^6 (2 x 10^6) molecules cm^{-3} and 1 x 10^7 (5.5 x 10^6) molecules cm^{-3}, respectively. The production of HNO_3 by the reaction of NO_2 with OH is an important sink for NO_x. At the average temperatures and pressures of the Bear Trap and Taylor Creek smoke plumes (275 K and 573 hPa, and 281 K and 644 hPa, respectively) and the two different OH estimates (estimates from second method in parenthesis), the pseudo first order rate coefficients for this association reaction are 3.74 x 10^{-5} (1.88 x 10^{-5}) s^{-1} and 9.54 x 10^{-5} (5.25 x 10^{-5}) s^{-1} which result in average NO_2 lifetimes against OH oxidation of $\sim$7.4 - 14.8 and $\sim$2.9 - 5.3 hours for the Bear Trap Fire and Taylor Creek Fire smoke plumes, respectively. The value reported by Akagi et al. ([12]) for the Williams Fire plume ($\sim$5.1 h) is between our two estimates. In the time these two plumes were observed ($\sim$4.4 and $\sim$2.6 hours for Bear Trap Fire and Taylor Creek Fire smoke plumes, respectively), we estimate, assuming no other loss paths for NO_x, that 55 - 75% and 40 - 60% of the initial NO_x would be converted to HNO_3 (or pNO$_3$). In the Taylor Creek Fire plume, after 2.6 hours of sampling, the total observed increase in HNO_3 + pNO$_3$ accounts for $\sim$41% of the initial NO_x (matching our estimate). On the other hand, in the Bear Trap Fire plume, after 4.4 hours of sampling, the observed increase in pNO$_3$ (no HNO_3 enhancement was observed in this plume) accounts for only 20% of the initial NO_x. This suggests that in the Bear Trap plume either a competitive pathway for NO_x loss dominated and/or that our assumptions of OH are not realistic. We note that rapid PAN production was observed in the Bear Trap plume without a similar sustained HNO_3 or pNO$_3$ formation with time. The mechanisms for PAN production in these plumes are the subject of ongoing work.

3.3 NO_y Partitioning Across the Entire WE-CAN Smoke-Impacted Dataset

There is considerable variability in the composition and abundances of $\sum NO_y$ across the entire WE-CAN dataset which includes measurements of young, medium and old smoke and air parcels not containing smoke sampled at different altitudes. The smoke-impacted flight segments presented in Figure 3.3 include samples from both fresh plumes attributed to known fires and diluted smoke intercepted outside of pseudo-lagrangian sampling efforts. No background was subtracted from these samples because there can be variability in the sources of NO_y and their abundances within the distance traveled by the aircraft in the 100-second TOGA sampling interval. Thus, as-

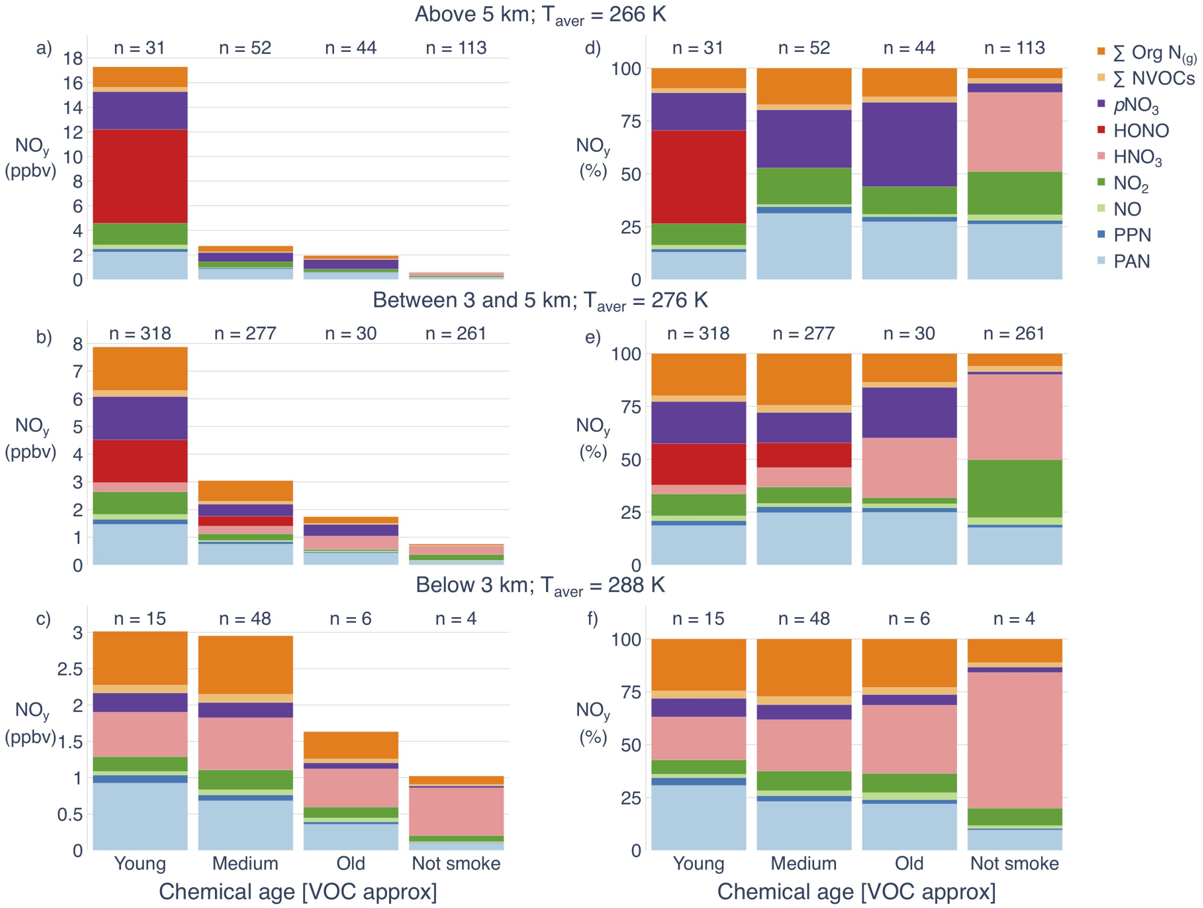

Figure 3.3: Partitioning of $\sum \mathrm{NO}_y$ within smoke-impacted and smoke-free samples within the full WE-CAN dataset. TOGA time-base samples are binned by an approximate chemical age: young (< 1 day of aging), medium (1 - 3 days of aging) and old (> 3 days of aging) as described in Section 2.3.2. Samples are also binned by sampling altitude, and the average temperature of the samples in each category is provided. No background is subtracted; the columns in the left panels represent the partitioning of absolute mixing ratios and are shown as percentages in the right panels. The number above each bar represents the number of individual TOGA time segments in category, not individual plume transects. The majority of samples were collected between 3 and 5 km ASL. A smaller number of samples were collected below 3 km, due to safety and logistical constraints of operating the aircraft in low visibility conditions and high terrain elevation on where most of the fires were located. These samples were largely collected during missed approaches at airports in California's Central Valley. The samples that are substantially influenced by anthropogenic emissions (see Section 2.3.2) are not included in this analysis. Note that the majority of the young and medium plumes (*i.e.,* left-most bars) coincide with the plumes presented in Figure 3.1.

signing an accurate background based on the TOGA timestep is not practical. Background subtractions would also have a larger influence on NEMR calculations for the most aged smoke-impacted samples.

Briefly, smoke-free samples are characterized by a larger contribution from HNO_3 to $\sum NO_y$ at all altitudes ($\sim$40 - 65%, decreases with altitude). Inversely, the $p$$NO_3$ contribution to $\sum NO_y$ increases with altitude (consistent with the thermodynamically favorable conditions for NH_4NO_3 formation), but it accounts for a small fraction (<5%) of the $\sum NO_y$ measured. NO_x is between (10-30%) of the $\sum NO_y$ measured with a larger contribution above 3 km (>20%). In the smoke-free WE-CAN samples, PAN and PPN contribution to the $\sum NO_y$ increases with altitude. We note that the WE-CAN smoke-free samples are not broadly representative of the summertime western U.S. atmosphere. The average T/RH/altitude of these samples are 273 K, 20% and 4.5 km ASL respectively and were largely collected outside of urbanized areas.

Across the smoke-impacted dataset, the contribution of HNO_3 to $\sum NO_y$ increases as the plumes age below 5 km. The relative contribution of HNO_3 is largest below 3 km ($\sim$20 - 30%). Background mixing ratios have not been subtracted from the data presented in Figure 3.3, thus the summary of NO_y species include contributions from both smoke and other sources (*e.g.,* anthropogenic emissions and their subsequent chemistry). The relative contribution of smoke is smallest in the most dilute, and often oldest, smoke-impacted air masses. Samples below 3 km also do not carry much weight in the summary of fresh plumes presented in Figure 3.1. Furthermore, the volatilization of HNO_3 from ammonium nitrate (NH_4NO_3) aerosol into the gas phase is more favorable under warmer temperatures (lower altitudes) ([92], [93]). However, there are other potential forms of inorganic and organic $p$$NO_3$ in these samples. There is no HNO_3 present in smoke above 5 km, consistent with Figure 3.1 and the temperature dependency of the NH_3-HNO_3 system that favours NH_4NO_3 at lower temperatures. The measured contribution of $p$$NO_3$ to $\sum NO_y$ varies with altitude. Figure 3.3 shows that, above 3 km, $p$$NO_3$ is generally of comparable abundance to NO_x in the younger smoke-impacted samples and more than twice as abundant as NO_x in the old smoke-impacted samples. Below 3 km the $p$$NO_3$ contribution decreases as the smoke-impacted samples age and dilute. Between 3 and 5 km (middle row of Figure 3.3) the contribution of $p\mathrm{NO}_3$ to $\sum \mathrm{NO}_y$ remains approximately constant ($\sim$15 - 24%) in all smoke impacted samples, while its contribution increases with more age above 5 km.

The amount of PANs present in the smoke-impacted samples increases with increasing altitude (note different y-axis), which is consistent with the temperature-dependent lifetime of these compounds ([19]). Briggs et al. ([43]) observed 25 - 57 % of NO_y as PAN in aged smoke plumes from regional fires observed in Oregon in summers 2012 and 2013. These numbers are within the range observed in the WE-CAN data set where PAN accounts for 22 - 27% of $\sum \mathrm{NO}_y$ in the medium and old smoke-impacted samples.

3.4 NO_y partitioning in the smoke-impacted California Central Valley

The NSF/NCAR C-130 performed a dedicated flight over the California Central Valley during a period when smoke from multiple fire complexes impacted the region. The aircraft performed a combination of low-level legs and two sets of missed approaches at three different airports in the region: Chico Municipal Airport (KCIC; 39.7991 °N, 121.8548 °W), Mather Airport (KMHR; 38.5637 °N; 121.2972 °W), and Merced County Castle Airport (KMER; 37.3735 °N; 120.5731 °W). There were many layers of smoke in the Central Valley, and the aircraft did not specifically target a particular smoke plume during this flight, but sampled smoke from the Carr Fire, the Mendocino Complex, and several fires located near Yosemite National Park. Most of the smoke was intercepted below 3 km (mean temperature = 300 K). The WE-CAN data shows that HNO_3 is the dominant NO_y species in the smoke-impacted samples collected over the Central Valley, accounting for $\sim$60% of the total NO_y. This is consistent with the overall picture shown in Figure 3.3 and the unfavorable warm conditions for PAN ([19]) and $p\mathrm{NO}_3$ ([81]). Gas-phase organic nitrates, PAN and NO_2 are the next most abundant NO_y species accounting for 16%, 10 %, and 9%, respectively. Finally, the contributions from $p\mathrm{NO}_3$, NO, PPN, and oxidized NVOCs were minor, individually contributing $\sim$1-3% of the total NO_y measured over the Central Valley.

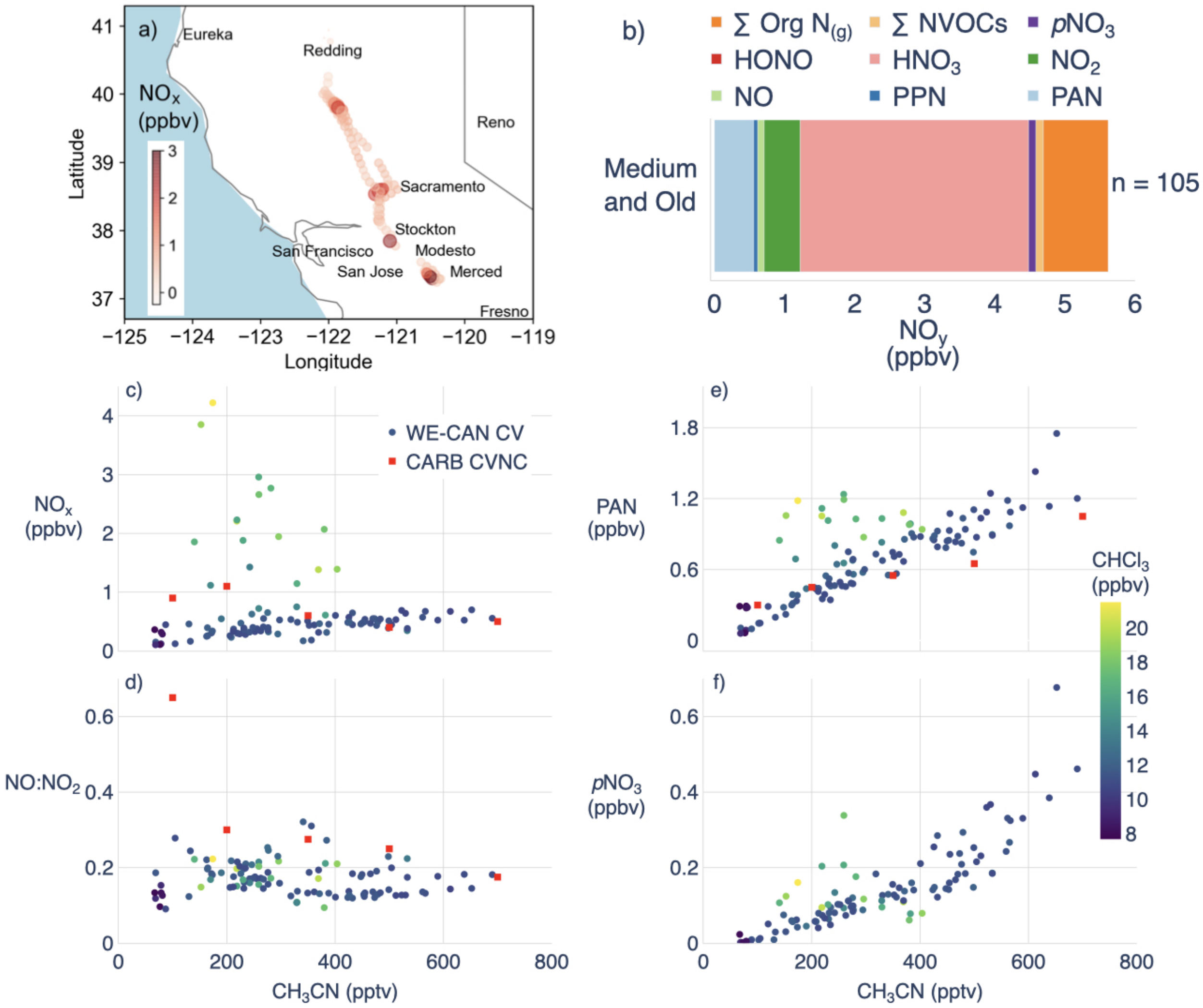

Figure 3.4: a) NSF/NCAR C-130 flight track through the California Central Valley (CV) on 8 August 2018 colored by NO$_x$ mixing ratio (ppbv). b) The inset bar shows the NO$_y$ partitioning for all the medium and old smoke-impacted samples shown in a). There were no samples classified as young based on the criteria in Section 2.3.2. Data was collected between 13:30 and 17:00 PDT. The $\sum$NO$_y$ mixing ratio in the smoke impacted Central Valley was ~5.5 ppbv, with little difference between the medium and old categories. Therefore, we show their partitioning together as one inset bar. c) - e) Scatterplots of NO$_x$, NO:NO$_2$, PAN and pNO$_3$ versus CH$_3$CN for the flight segment through the region are shown in a). These panels are colored by chloroform (CHCl$_3$). Shown in red squares are NO$_x$ (c), PAN (e), and NO:NO$_2$ (d) observed during ARCTAS-CARB ([90]).

The NASA DC-8 research aircraft outfitted with a similar suite of instrumentation sampled this same geographical region during the ARCTAS-CARB field campaign in June 2008 ([94]), another time with large wildfires in northern California. Using similar data collected below 3 km and between 11:00 and 17:00 PDT, we are able to compare NO_x, PAN and $NO:NO_2$ ratios as a function of CH_3CN with those measured by Singh et al. ([90]) in 2008. We note that the WE-CAN data was collected later in the day, between 13:30 and 17:00 PDT. Singh et al. ([90]) report average NO_x enhancements of $\sim$2 - 5 ppbv, and these are generally higher than the total NO_x mixing ratios observed in this region during WE-CAN. The only instances when NO_x mixing ratios during WE-CAN were within the range of those reported by Singh et al. ([90]) are within air masses clearly impacted by anthropogenic emissions, denoted in Figure 3.4 as samples with elevated chloroform (3-methyl-pentane, tetrachloroethylene, HFC-134a, HCFC-141b, and HCFC-22 were also elevated in these samples). In these instances, NO_x mixing ratios in smoke-urban mixtures increased by $\sim$3.5 ppbv. Singh et al. ([90]) observed decreasing $NO:NO_2$ ratios with increasing smoke contribution. The $NO:NO_2$ ratios observed over the California Central Valley during WE-CAN are not consistent with the pattern in Singh et al. ([90]). This ratio is also not systematically perturbed in more anthropogenically influenced air masses (*i.e.,* points with elevated chloroform).

We also compared PAN mixing ratios between the WE-CAN data set and the data reported by Singh et al. ([90]). Both show a strong relationship between PAN and CH_3CN. Samples with more PAN relative to CH_3CN in the WE-CAN data set appear to be the result of injections of anthropogenic emissions. For the same CH_3CN mixing ratio, there can be twice as much PAN when smoke is mixed with urban emissions. $p$$NO_3$ abundances in the California Central Valley also increase with increasing fire influence (*i.e.,* higher CH_3CN mixing ratios). There are $p$$NO_3$ outliers when anthropogenic emissions mix with smoke. However, the relative change is much smaller than what was observed for NO_x and PAN.

Chapter 4

Evolution of PAN in wildfire smoke plumes detected by the Cross-Track Infrared Sounder (CrIS) over the western US during summer 2018.

4.1 Western U.S. CrIS PAN Retrievals and Wildfire Smoke

During 2018, there were 23,104 wildfires in the western US (Northwest, Southwest, Northern California, Southern California, Great Basin, Rocky Mountain, and Northern Rockies) corresponding to a burned area of > 6.5 million acres (National Interagency Coordination Center (NICC) statistics for 2018; https://www.nifc.gov/nicc/index.html). Figure 4.1 shows CrIS retrievals of CO (Figure 4.1a) and PAN (Figure 4.1c) on 20 August 2018 when the Mendocino Complex fire was active. Fires detected by the Visible Infrared Imaging Radiometer Suite (VIIRS) on the Suomi-NPP on this day are shown as red dots. Figure 4.1 shows that many fires can be active on a given day and that CrIS has the ability to detect CO and PAN from individual smoke plumes. This is in contrast to the TES PAN retrievals which can really only be interpreted in aggregate ([45]).

Figure 4.1 shows that PAN and CO enhancements from the wildfires cross many western states, and that the smoke plumes from some wildfires are detectable multiple days downwind. Many of the smoke plumes sampled during WE-CAN were also detected by the CrIS (*e.g.,* Carr Fire, Cougar Creek Fire, South Sugarloaf Fire, Taylor Creek Fire). Within the lifecycle of a wildfire, the CrIS overpass time at ∼1:30 pm LT (∼19:30 - 20:30 UTC) often occurs before many wildfires are most active. The WE-CAN sampling efforts most often intercepted fresh plumes between 3 and 6 pm LT (21:00 - 01:00 UTC), when plumes were injected sufficiently high to be reached by the aircraft. Therefore, there is often a ∼4 hour difference between the satellite overpass and the *in situ* measurements.

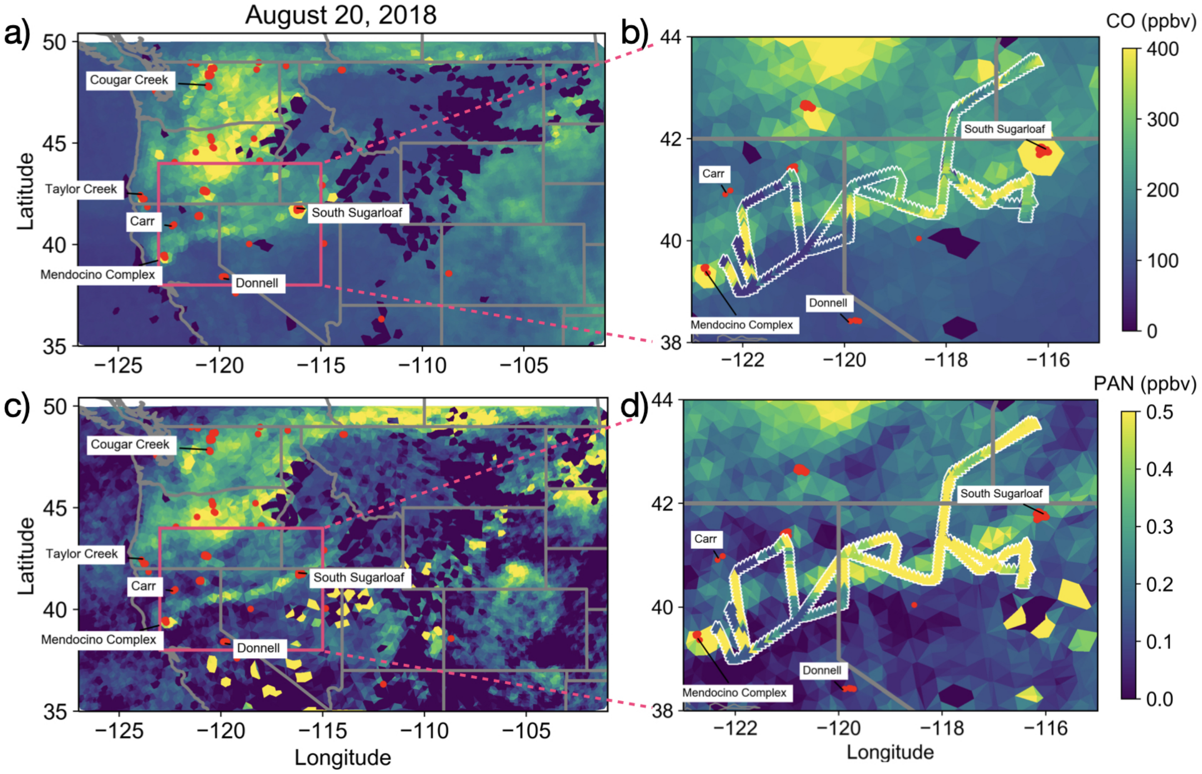

Figure 4.1: a) Daytime overpass tropospheric average CrIS CO for 20 August 2018. c) Daytime overpass tropospheric average CrIS PAN for 20 August 2018. The pink box in panels a) and c) encompasses the region plotted in panels b) and d). 1-min averaged *in situ* b) CO and d) PAN observations associated with the Mendocino Complex Fire on 20 August 2018 are shown in triangles. These observations were collected between 21:00 and 02:00 UTC (2 and 7 PM LT). Red dots indicate high quality fire detection by VIIRS, also onboard the Suomi-NPP satellite. Fires that produced smoke plumes sampled during the WE-CAN campaign are labeled.

Figure 4.1b and Figure 4.1d show the aircraft sampling of the plume associated with the Mendocino Complex. The Mendocino Complex was first active on 27 July 2018 and was not contained until mid-September. This is the largest fire in the history of the state of California with a final burn area of > 450,000 acres. The WE-CAN team first sampled the smoke plume associated with the Mendocino Complex fire on 5 August 2018 as part of a large "river of smoke" that contained emissions from multiple fires. On 20 August 2018, the NSF/NCAR C-130 sampled the fires in a pseudo lagrangian fashion completing multiple transects across the plume. *in situ* PAN (CO) abundances at the core of the Mendocino Complex smoke plume on 20 August 2018 ranged from 3 - 7 ppbv (0.7- 2 ppmv), and the plume was sampled between 610 - 570 hPa (4.1 - 4.6 km ASL). CrIS free tropospheric average PAN (CO) mixing ratios within the plume ranged from 0.14 - 1.3 ppbv (0.13 - 0.48 ppmv).

Given the differential sensitivities between the CO and PAN retrievals by CrIS, and the need to use both products to distinguish between dilution and chemical evolution in fire plumes, we use the CO retrievals at specific pressure levels to determine whether to include an individual set of retrievals in our analysis. Figure 4.2 shows the CO retrievals at 380, 510, 680, and 900 hPa for 20 August 2018 associated with the WE-CAN sampling of the Mendocino Complex Fire (Figure 4.1b and Figure 4.1d). We remind the reader that the DOFS for CO are 2 which means that the CO retrievals contain information about the CO tropospheric column average and some information about the vertical distribution of CO. However, we include Figure 4.2 to show that the largest CO mixing ratios are often reported at the 510 and 680 hPa levels (Figure 4.2b and Figure 4.2c) where the CO averaging kernels indicate consistently strong sensitivity (Figure 2.3a and Figure 2.3b). The PAN retrieval is largely insensitive near the surface (*i.e.,* < 850 hPa), but it is characterized by similar sensitivity across much of the free troposphere. Following Fischer et al. ([45]), we define smoke-impacted retrievals using the CrIS dataset where CO is > 150 ppbv on either the 510 or 680 hPa level. See the following section for details.

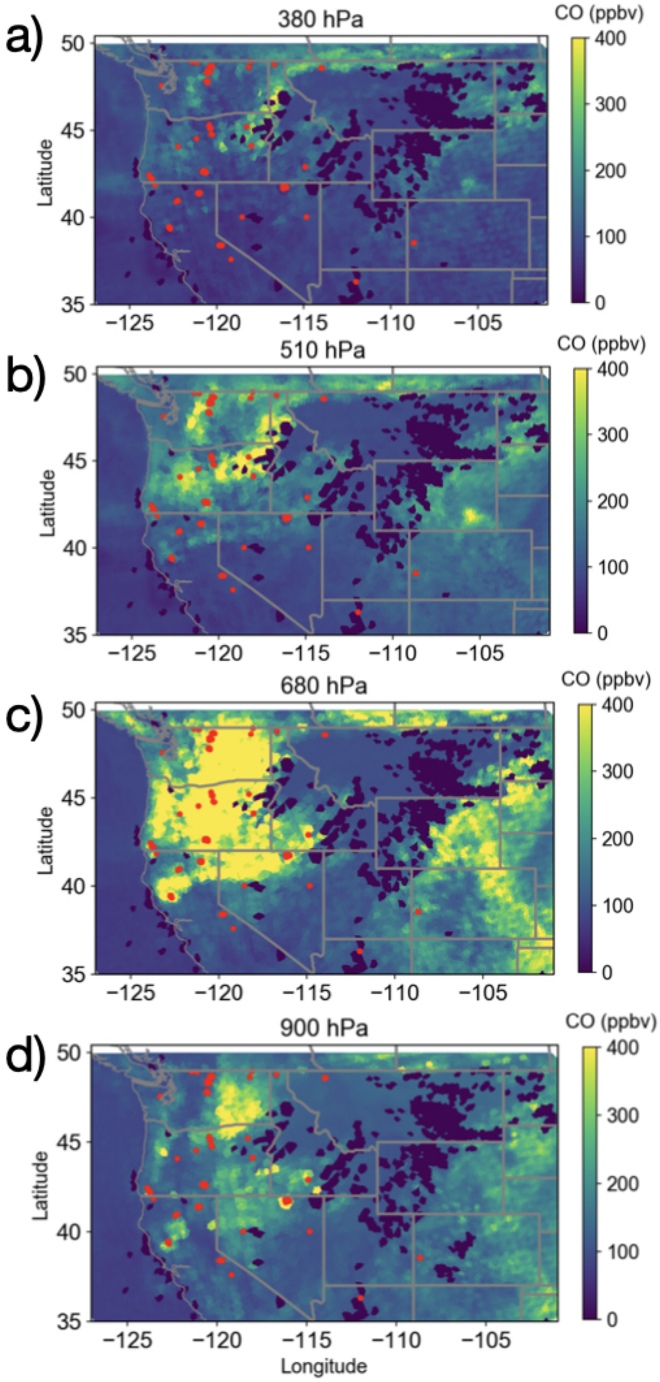

Figure 4.2: Daytime CrIS CO retrievals at a) 380, b) 510, c) 680, and d) 900 hPa on 20 August 2018. Red dots show high quality fire detection by VIIRS on the Suomi-NPP satellite

4.2 CrIS PAN Abundances Within and Outside Wildfire Smoke Plumes

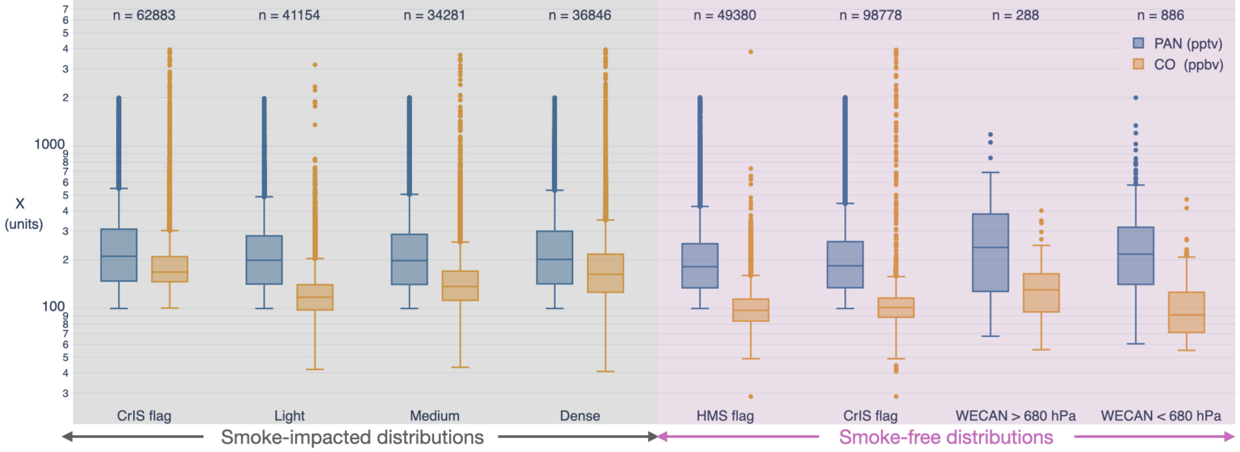

Figure 4.3: Distributions of PAN (blue) and CO (orange) for smoke-impacted retrievals identified using the CrIS criteria (see section 4.2) and the HMS smoke identification (light, medium, and dense) and smoke-free or "background" conditions estimated using CrIS tropospheric average observations and in situ observations from WE-CAN below and above 680 hPa. The number above each distribution corresponds to the number of individual retrievals in each category.The y-axis indicated the PAN or CO tropospheric column average mixing ratios in pptv and ppbv, respectively as shown in the label.

Figure 4.3 presents a summary of smoke-impacted and smoke-free or "background" tropospheric average PAN and CO CrIS retrievals designated using multiple methods. We classify smoke-impacted retrievals using satellite observations in two ways. First, we classify the CrIS retrievals as smoke-free or smoke-impacted using the *cdist* tool in the python *scipy.spatial.distance* package to co-locate the CrIS retrievals with the NOAA Hazard Mapping System (HMS) smoke plumes. The smoke plumes identified by the NOAA HMS are classified as light, medium, or dense smoke, so we present the distribution of CrIS observations in all these categories in Figure 4.3. The second satellite-based classification is based on the CrIS measurements themselves. Here smoke-impacted retrievals include any CrIS retrievals where CO > 150 ppbv at the 510 or 680 hPa level.

The right side of Figure 4.3 provides a summary of estimates of summertime background PAN and CO mixing ratios over the western U.S. based on multiple definitions/techniques. The designation of background is important for both quantifying the contribution of wildfire smoke to the abundance of a given species within a given air mass, and for separating chemical processes from dilution within the smoke plume ([39]). The correction for dilution is usually done by normalizing the abundance of the species of interest (*i.e.,* PAN) by dividing by the abundance of a conserved tracer (*e.g.,* CO or HCN). This ratio is referred to as normalized excess mixing ratio (NEMR) of the species of interest (*i.e.,* PAN). While there are challenges associated with identifying background air within *in situ* datasets, the challenges are much larger with satellite data. This is an issue that needs to be addressed if we are to use satellite data in a manner analogous to *in situ* measurements ([45]). Figure 4.3 shows that the satellite-based designations of background conditions (*i.e.,* both the HMS-based designation and the designation based on CrIS alone) produce similar estimated median background values for PAN ($\sim$0.18 ppbv). The rightmost background classification is based on the *in situ* out-of-smoke observations collected during WE-CAN. Out-of-smoke WE-CAN observations are defined as any sample where CO, HCN and CH_3CN are < 85 ppbv, 275 pptv, and 200 pptv, respectively ([66]). We then separate the dataset into two pressure (altitude) bins: surface to 680 hPa (< $\sim$3.2 km ASL) and above 680 hPa (3.2 - 6.1 km ASL).

Within the two different smoke identification techniques, only $\sim$30% of the CrIS retrievals are classified as smoke-free by the HMS criteria. However, 61% of the retrievals are classified as smoke-free based on the CrIS criteria. This indicates that $\sim$half of the smoke-free retrievals in this subset are actually smoke-impacted, and thus likely contain elevated CO and PAN from smoke. Figure 4.3 shows that the smoke-impacted CrIS retrievals (from the HMS and CrIS criteria) contain more PAN and CO than the smoke-free distributions. This pattern was not distinguishable in TES data, but it is significant in the CrIS data.

The *in situ* measurements produce higher background estimates (> 0.2 ppbv, median of the smoke-free samples collected during WE-CAN as identified by O'Dell et al. [66]) than the satellite based estimates, especially within the boundary layer (*i.e.,* below 680 hPa). As discussed above, the *in situ* measurements are limited on their spatial coverage. Thus, the number of samples is substantially smaller than the number of available satellite retrievals. However, they provide a robust measurement of the abundance of PAN and CO at the time and location of air masses that have not been impacted by biomass burning. Often, as was the case during summer 2018, fresh smoke plumes were injected within larger more dilute smoke plumes, often from multiple fire complexes burning over multiple days-to-weeks (*e.g.,* Mendocino Complex Fire, Carr Fire). For this reason, Figure 4.3 also shows a summary of the distribution of CrIS PAN and CO in light, medium and dense smoke regions as designated by HMS. The light smoke designation is often an appropriate background for specific dense (and more fresh) plumes.

In the following section, we assume background tropospheric average mixing ratios for PAN and CO of 0.13 and 95 ppbv. This choice of background values represent the lowest 25th percentile for PAN and the highest 25th percentile value for CO for the distributions shown in Figure 4.3. These backgrounds are within the range of background mixing ratios used by Fischer et al. ([45]) to analyze smoke plumes detected by TES. Singh and Hanst ([20]) estimated PAN abundances of 0.09 - 0.36 ppbv in the upper troposphere. CO background mixing ratios have changed as a result of emission controls (*e.g.,* [95], [96]), and over North America, they are certainly impacted by biomass burning during summer months (*e.g.,* [97], [98]). The choice of background does impact the absolute magnitude of the calculations presented in Section 4.3, and we discuss that below.

Figure 4.4 shows free tropospheric PAN mixing ratios averaged in a 0.5° x 0.5° grid over 24 July 2018 and 13 September 2018. Briefly, to estimate the average daily PAN abundance within a given grid cell, we add all the retrievals within that cell over the 50 days of retrievals and divide by 50. To construct the average daily PAN related to smoke-free or smoke-impacted observations, we included only the retrievals that meet the smoke selection criteria in the calculation described above. We then subtracted the smoke-free from the smoke-impacted tropospheric average PAN to yield an estimate of the contribution of smoke to average PAN on a given day (Figure 4.4d and Figure 4.4h for the CrIS and HMS smoke criteria, respectively). We then divided the smoke contribution by the tropospheric average PAN to obtain the fraction of PAN associated with smokey conditions. Figure 4.4a shows that CrIS PAN tropospheric mixing ratios range from 0.10-1.1 ppbv over the western US during the summer season (averaged over 50 days). The areas with the highest free tropospheric PAN correspond to Northern California, Northern Nevada, South Idaho, the Rocky Mountains, and the Pacific Northwest. All these areas were impacted by smoke from many active fires or smoke transported downwind from upwind fires.

$$\overline{XPAN_i} = \frac{\sum_{m=1}^{50}(\sum_{n=1}^{n} XPAN_n)}{50} \tag{4.1}$$

Where:

i= number of grid cells.

n = number of retrievals in a 0.5° x 0.5° cell.

m = number of retrieved days.

To assess what percentage of the PAN retrieved by CrIS can be attributed to fires, we separate the retrievals as smoke-free or smoke-impacted using both the criteria from the CrIS retrievals alone and the HMS data described above. Figure 4.4b/d and Figure 4.4c/e show the smoke-free and smoke- impacted retrievals, respectively. As noted above, more retrievals ($\sim$60%) are identified as smoke-free with the CrIS criteria (Figure 4.4c) and many of those show elevated PAN (> 0.6 ppbv) (i.e., over the Rocky Mountain). On the other hand, fewer regions with elevated PAN are identified as smoke-free by the HMS flag (Figure 4.4g). The CrIS smoke criteria show that the average contribution of fires on a given day to PAN is 40-70% over northern California, Nevada, Oregon, Idaho, and Washington (Figure 4.4e). The HMS smoke criteria show that more of the western U.S average PAN can be attributed to smoke. Figure 4.4a shows that the highest CrIS PAN retrievals are located over the Rocky Mountains. The HMS smoke criteria show that 40 - 70% of the free tropospheric PAN over this area can be attributed to smoke.

Finally, we further separate the smoke-impacted retrievals (HMS flag) into light, medium, and dense contributions (lower panel of Figure 4.4; panels j - l). Light smoke (Figure 4.4j) can be responsible for up to 60% of the free tropospheric PAN over Nevada, Utah, Colorado, and Wyoming. Moderate smoke (Figure 4.4k) can contribute up to 60% of the free tropospheric PAN over central Nevada, contributing to up to ∼40% over the rest of the western U.S. Dense smoke (Figure 4.4l) is mainly located over northern California, Oregon, and Washington; ∼70% of the total free tropospheric PAN detected by CrIS over this region is associated with dense smoke near to most active fires during the 2018 wildfire season (*e.g.,* Carr Fire and Mendocino Complex Fire).

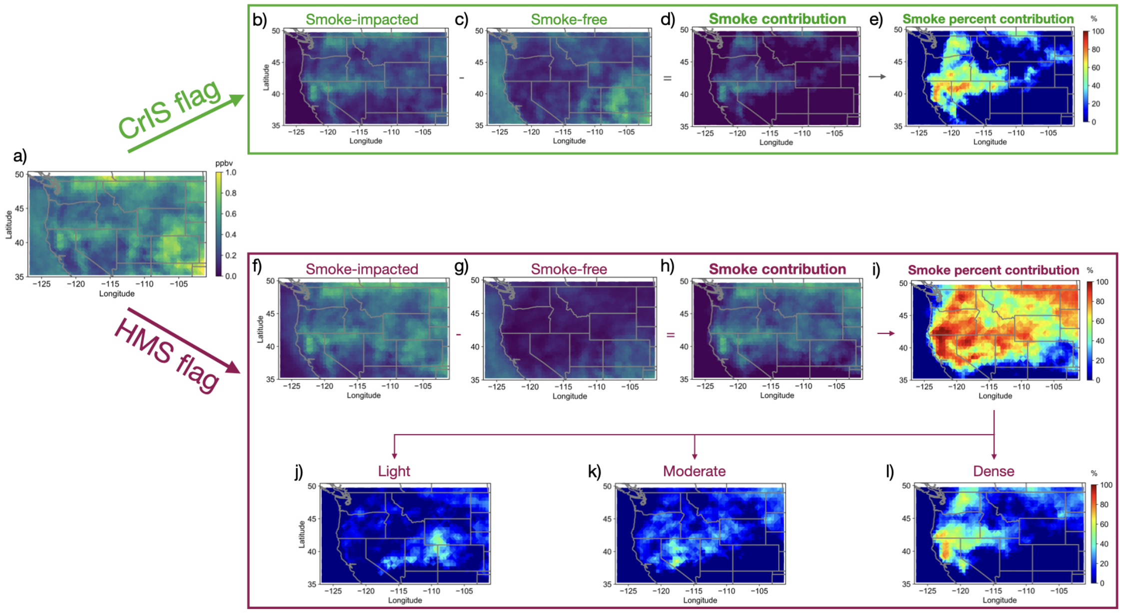

Figure 4.4: a) Tropospheric PAN averaged in a 0.5° x 0.5° grid during 24 July 2018 - 13 September 2018. Tropospheric average PAN from b) smoke-impacted and c) smoke-free retrievals as identified by the CrIS criteria (CO > 150ppbv at either 510 or 680 hPa). d) Smoke contribution to average tropospheric PAN and e) smoke percent contribution to average tropospheric PAN . f), g), h), i) same as b), c), d), e) with the HMS criteria. HMS smoke percent contribution to average tropospheric PAN were further separated into j) light, k) moderate, and l) dense plumes.

Table 4.1: Percent contribution to free tropospheric PAN attributed to wildfires over the entire study region from CrIS as identified by the selection criteria described in section 4.2

Selection citeria	Smoke-contribution
CrIS	14%
HMS	49%

4.3 CrIS - detected PAN Enhancements in Wildfire Smoke Plumes

Figure 4.5 shows CrIS CO (6a) and PAN (6b) retrievals on 13 September 2018, and the plume associated with the Pole Creek Fire in Utah is highlighted. This particular plume is included here because it demonstrates that the combined spatial resolution and sensitivity of CrIS is sufficient to detect chemical evolution in plumes when background conditions are favorable for these calculations (*i.e.,* a plume is isolated and the abundance of PAN and CO within the plume are substantially higher than outside the plume). The Pole Creek Fire was reported on 6 September 2018. On 13 September 2018 high winds drove active burning despite efforts to contain the fire. The smoke closest to the fire becomes visible in satellite imagery (GOES16 2km Ch2 HighRes Vis) between 16:00 and 16:30 UTC and the evolution of the plume can be followed in visible satellite imagery until nightfall; the plume crosses the Utah-Wyoming border at 20:00 UTC. The Suomi-NPP overpass shown in Figure 4.5 is at 20:40 UTC (3.6 - 4.6 hours after the plume becomes visible). Based on visible imagery and fire reports, this fire continued to burn actively and the smoke was advected in sustained high winds after the satellite overpass. An isolated plume extending from the Pole Creek Fire can be distinguished through 01:00 UTC 14 September.

Figure 4.5c isolates the Pole Creek Fire plume with the calculated PAN NEMR in percent units. Figure 4.5c shows that the PAN NEMR increases in the smoke plume with distance from the fire source, reflecting the photochemical production of PAN within the plume. To our knowledge,

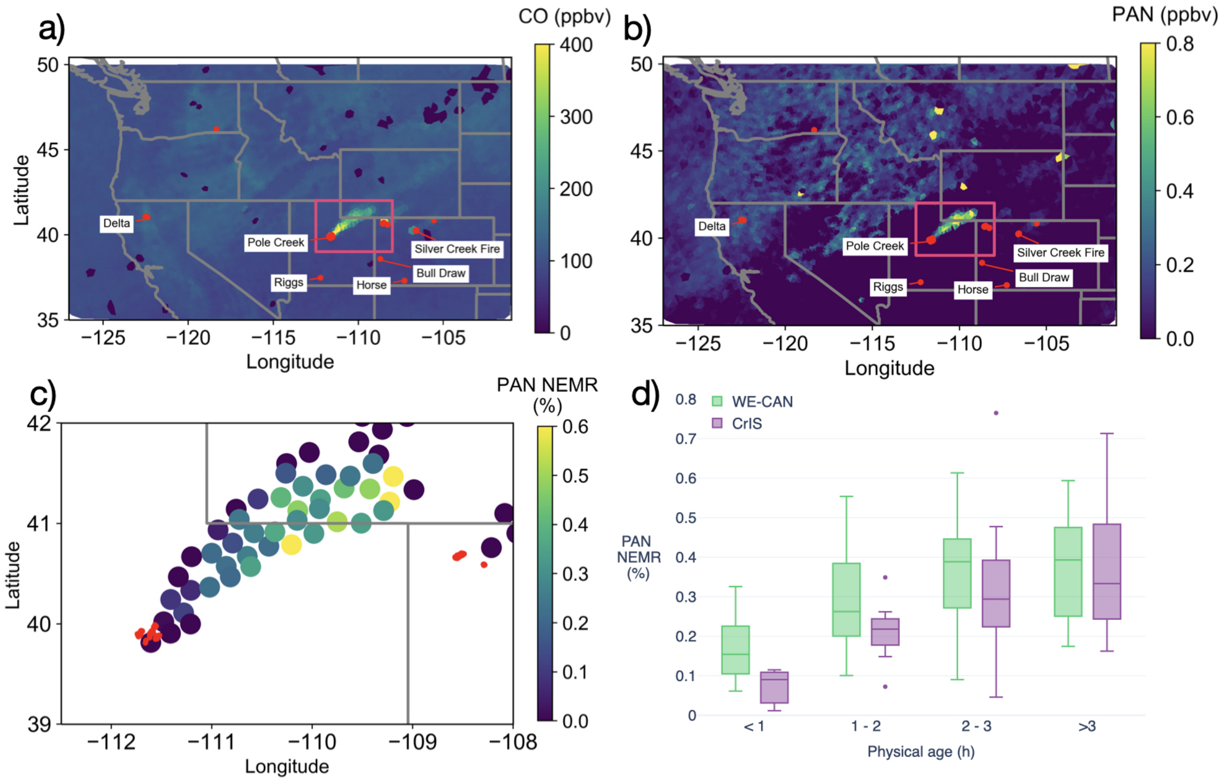

Figure 4.5: a) Daytime overpass CrIS a) CO and b)PAN retrievals for 13 September 2018. The pink boxes in panels a) and b) encompass the region plotted in panel c). c) CrIS PAN NEMRS for the Pole Creek Fire Plume. The plume has been isolated in this figure by requiring CO > 150 ppbv at the 510 or 680 hPa level. NEMRs are calculated assuming a background of 95 and 0.13 ppbv for CO and PAN respectively. d) PAN NEMRs for the Pole Creek Fire (purple) calculated with the CrIS data compared to those calculated across all fresh plumes associated with known fires encountered during the WE-CAN campaign (green). See Chapter 3 for details.

this is the first time PAN production on the timescale of minutes to hours has been observable via satellite.

Figure 4.5d compares the CrIS PAN NEMRs from the Pole Creek Fire smoke plume with those produced from the WE-CAN *in situ* data set. To compare these two datasets, we assign a physical age to each CrIS retrieval based on the visible images from GOES-16 and HYSPLIT forward and backward trajectories initiated at the time of the satellite overpass (21:00 UTC). A visual inspection of satellite images and the trajectory analysis concur that the front edge of the plume is 3 - 4 hours old at 21:00 UTC. Using the distance function of the Python geopy package, we calculate the distance from each retrieval to the fire centroid for that day as reported by Inciweb. Finally, we calculate an average plume wind speed dividing the distance of the furthest in-smoke CrIS retrieval by the range of ages of the front edge of the plume. This yields average wind speeds between 19 - 26 m/s. Using the lower estimate for wind speed, we estimate the age of each in-smoke CrIS retrieval. Figure 4.5d shows that the rate of PAN production in the Pole Creek Fire plume is within the range of that observed for plumes that were sampled with the NSF/NCAR C-130 during WE-CAN. Note that the PAN NEMRs near the fire in Figure 4.5c (and those included in the box plot for < 1 hour of physical age in Figure 4.5d) are largely lower than those observed during WE-CAN. This likely reflects, at least partially, the ability of the satellite to observe smoke closer to a large fire than often possible with aircraft due to logistical and safety constraints.

Figure 4.6 demonstrates the ability of CrIS to observe a wildfire plume over the course of several days as it evolves in the atmosphere. The Carr Fire was one of the largest fires during the 2018 wildfire season. This fire burned 229,651 acres over 38 days (NICC). The smoke plume from the Carr Fire is first visible in the CrIS PAN and CO retrievals on 26 July 2018 (Figure 4.6a). The plume continues to be easily distinguished on 27 July 2018 (Figure 4.6b) as the fire continued to burn and the smoke from the previous day moved toward the east-northeast. Figure 4.6a/b shows the spatial evolution of the Carr Fire smoke plume as it traveled from California to several other downwind states (textiti.e., Nevada, Idaho, Oregon, Utah, Wyoming) within 24 hours. The two

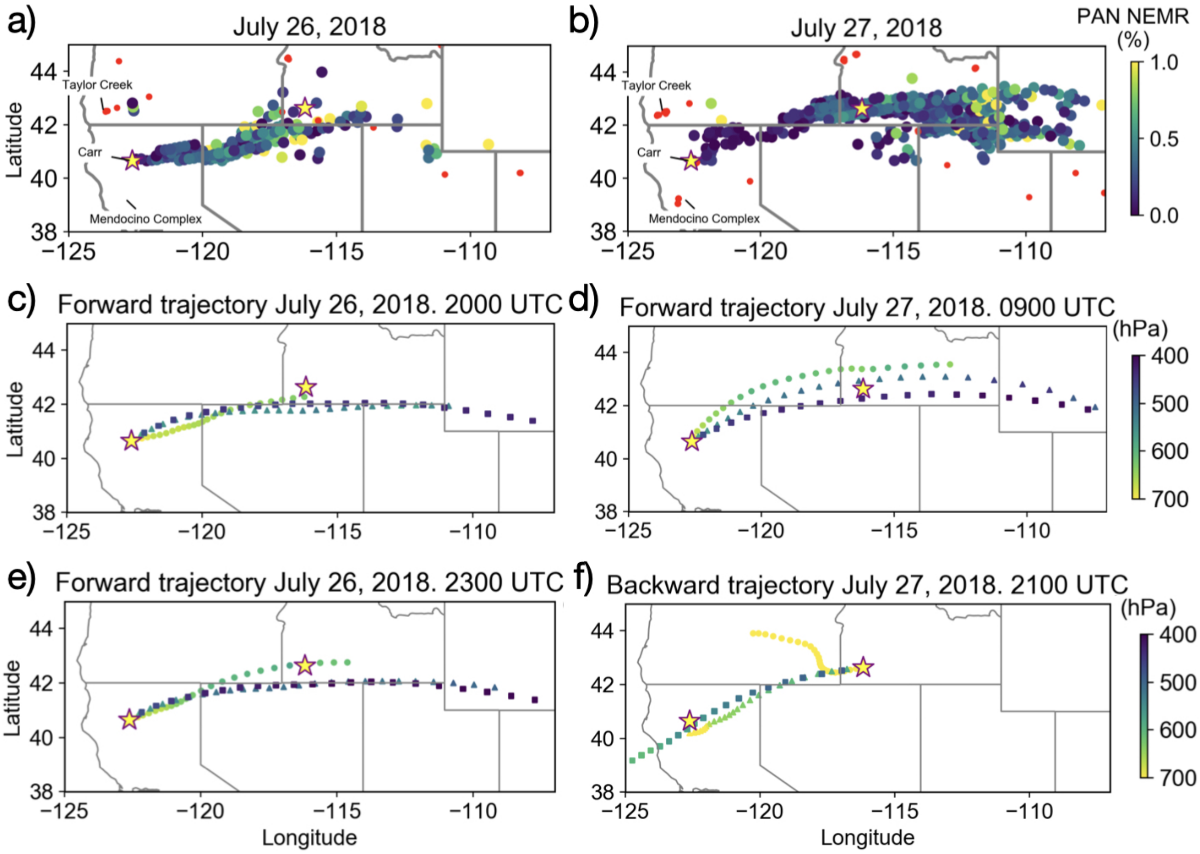

Figure 4.6: CrIS PAN NEMRs from the Carr Fire a) 26 July 2018 and b) 27 July 2018 calculated assuming 95 and 0.13 ppbv of CO and PAN background mixing ratios respectively. Panel c) - f) show forward or backwards trajectories initialized at 720 (circles), 600 (triangles) and 495 (squares) hPa. Forward trajectories were always initialized at the Carr Fire centroid location (40.65° N, 122.63° W) (yellow star to the west), and backward trajectories were initialized at (42.63° N, 116.18° W) (yellow star to the east). Panel c) forward trajectory on 26 July 2018 at the approximate Suomi-NPP overpass time (20:00 UTC), panel e) forward trajectory on 26 July 2018 at the time when WE-CAN sampled the Carr Fire (∼23:00 UTC), panel d) forward trajectories initialized on 27 July 2018 at 09:00 UTC, and panel f) backward trajectories initialized on 27 July 2018 at the approximate Suomi-NPP overpass time (21:00 UTC).

yellow stars plotted across all the panels in Figure 4.6 show the locations where forward (Carr Fire centroid) and backward (southwest Idaho) trajectories are initialized.

Like all wildfires, the injection height of the Carr fire smoke plume was variable, and the CrIS data itself offers limited information on the vertical location of the plume. The NSF/NCAR C-130 sampling provides one constraint. The aircraft sampled the Carr Fire plume on 26 July 2018 at $\sim$23:00 UTC, and the pseudo-lagrangian sampling of this plume occurred between 665 - 510 hPa. Panels c) and e) show example HYSPLIT trajectories initialized on 26 July 2018 at the approximate time of the satellite overpass (20:00 UTC) and the WE-CAN sampling time (23:00 UTC), respectively. Panel c) shows that smoke emitted by the Carr Fire on 26 July 2018 would reach southwest Idaho (easternmost yellow star) in 11-24 hours depending on the assumed smoke injection altitude. Slower boundary layer winds ($\sim$720 hPa) produce a longer transport time ($\sim$24 hours).

A set of backward trajectories, initialized at various altitudes from the easternmost star on Figure 4.6f provide additional constraints on the likely altitude of the smoke detected by CrIS. We calculated 3 back trajectories initialized at 720 (circles), 600 (triangles) and 495 (squares) hPa at 21:00 UTC (Figure 4.6f), the approximate daytime CrIS overpass time on 27 July 2018. Figure 4.6f shows that back trajectories initialized between 600 and 495 hPa are consistent with the transport of the smoke plume visible by satellite. Back trajectories initialized lower (*i.e.,* $\sim$700 hPa) are inconsistent with the visible smoke plume transport pathway. The example forward trajectories in Figure 4.6d confirm the 11-24 hour smoke age estimate range.

The transport analysis above implies that the PAN NEMRs detected on 27 July 2018 by CrIS (at 21:00 UTC) over southwest Idaho originated $\sim$10:00 UTC ($\sim$03:00 LT) when the Carr Fire would have been burning at a lower intensity. The atmospheric temperatures encountered by the smoke favor PAN stability. We used the range of temperatures (288 - 264 K) from the North American Regional Analysis (NAAR) reanalysis data at the time and locations of the forward trajectories in Figure 4.6d, a $NO:NO_2$ between 0.15 and 0.30 based on the *in situ* observations and an approximate OH concentration of $2x10^6$ molecules cm^{-3} to calculate PAN lifetime based on Singh ([19]).

The PAN lifetime can range between 7.5 - 414 h depending on the plume injection altitude and the assumed NO:NO_2 ratio. Higher injection altitudes and lower NO:NO_2 ratios promote PAN stability. For instance, if we assume that the plume is injected near the surface (*i.e.,* 720 hPa), the PAN lifetime is $\sim$7.5 - 12 hours. If the plume is injected higher (*i.e.,* 600 (490) hPa) the PAN lifetime is $\sim$60 - 95 ($\sim$300 - 400) hours. If the plume is injected at $\sim$ 600 hPa (altitude of the *in situ* measurements) or higher then the PAN lifetime is certainly sufficient to be transported to the location of the second star in Figure 4.6. Figure 4.6b shows that the PAN NEMRs in southwest Idaho on 27 July 2018 are comparable to those closer to the Carr fire centroid on 26 July 2018 (Figure 4.6a), suggesting PAN conservation and transport over long distances. As suggested in Section 3.1 and 3.2 PAN NEMRs plateau after 3-4 hours in fresh plumes sampled during WE-CAN over the western US.

Figure 4.7 shows the distribution of PAN enhancement ratios relative to CO (%) (NEMRs) from *in situ* and satellite observations. The distribution of PAN enhancement ratios (NEMR) for smoke-impacted conditions, and specifically for the Carr Fire smoke plume, calculated from CrIS overlap the distribution of NEMRs calculated from *in situ* measurements within smoke plumes. They also overlap with those calculated from TES in-smoke data in Fischer et al. ([45]). However, there is a substantial fraction of satellite-based in-smoke NEMRs that are lower than normally observed during WE-CAN sampling efforts. CrIS-based NEMRs < 0.2% are characterized by lower PAN (median 0.25 vs 0.33 ppbv for NEMRs > 0.2%) and high CO (median 227 vs. 156 ppbv for NEMRs > 0.2%). A generalized background will have a higher impact on smaller PAN and CO mixing ratios retrieved by CrIS (*e.g.,* smoke where PAN has not yet been produced or dilute smoke). There is no evident spatial clustering of the NEMRs < 0.2% (Figure B.1) disproving the hypothesis that an interference from an specific surface type (*e.g.,* silica, ice) could be affecting the PAN retrievals. There are several circumstances where smoke would be characterized by lower PAN abundances relative to CO. First, the satellite is able to retrieve smoke closer to the fire source than aircraft are typically able to do. This smoke will be characterized by high CO (more concentrated) and lower PAN (not yet produced within the smoke), driving the NEMRs to lower values. Second,

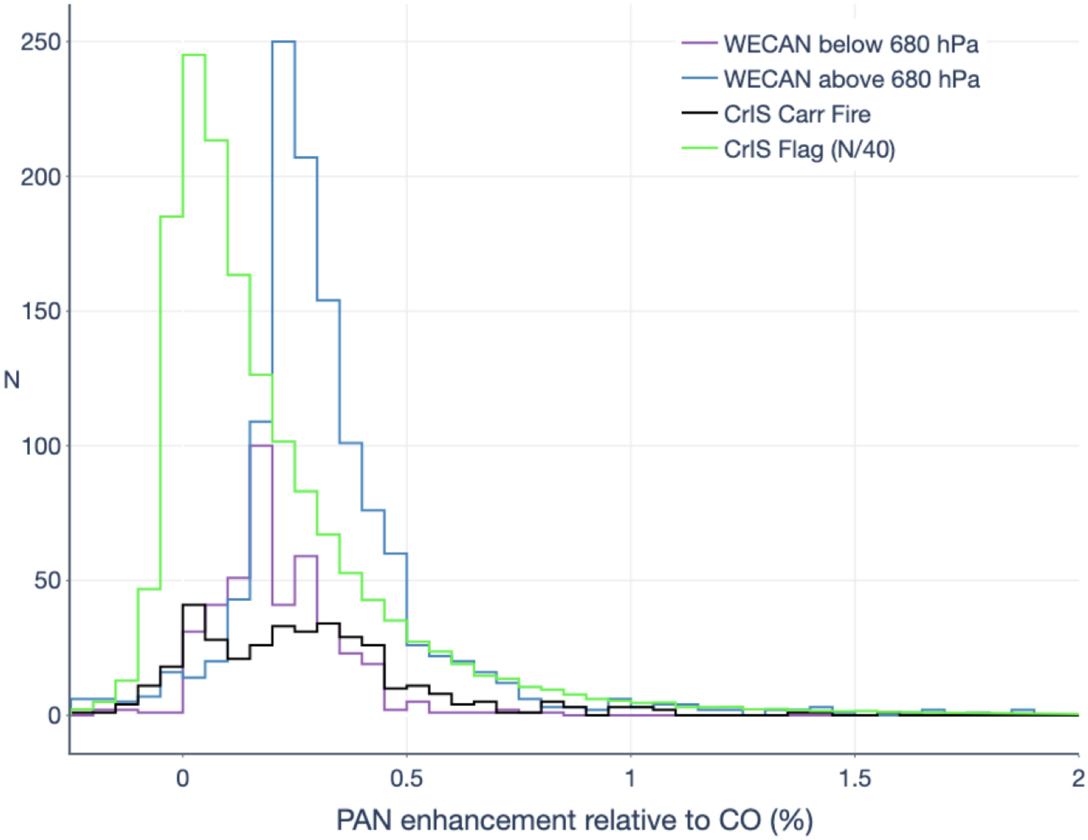

Figure 4.7: Histogram of calculated PAN enhancement ratios relative to CO (%) based on smoke-impacted samples from *in situ* (WE-CAN, purple and blue) and satellite (CrIS, green and black) observations. Enhancement ratios for the *in situ* observations are calculated using the 25^{th} percentile background from the corresponding distributions shown in Figure 4.3. The *in situ* data is divided into altitude bins corresponding to samples below (purple) and above (blue) 680 hPa. The enhancement ratios for CrIS observations of the Carr Fire plume and the smoke-impacted retrievals during summer 2018 (24 July - 13 September) are shown in black and green, respectively. The CrIS PAN NEMRs are calculated using 0.13 and 95 ppbv background mixing ratios for PAN and CO, respectively. Note that the number of smoke-impacted samples for the CrIS retrievals (green) is divided by 40 for scaling purposes.

the lifetime of PAN is highly temperature dependent, and surface temperatures in summer over the western U.S. can be sufficiently high to reduce the thermal lifetime of PAN to $\sim$hours. The smoke-impacted retrievals may be closer to the surface. In addition to a short PAN lifetime, the near-surface sensitivity of CrIS to PAN is lower than that to CO.

Chapter 5

Conclusions

The WE-CAN field campaign utilized the NSF/NCAR C-130 to systematically build a dataset of afternoon smoke observations. The WE-CAN observations include more than 200 plume transects that can be connected to >20 different specific fires and an additional set of smoke samples from a wider set of fires. The full dataset affords the opportunity to examine the evolution of oxidized reactive nitrogen in western U.S. smoke plumes over timescales of hours to days.

1. We find that daytime emissions of NO_x and HONO from wildfires are rapidly transformed to more oxidized forms of NO_y ($p$$NO_3$, PANs, and gas-phase organic nitrates) within the first few hours of physical aging in the plumes sampled during WE-CAN. After $\sim$2 hours the fraction of $\sum NO_y$ in the form of $p$$NO_3$ approximately doubles, and after $\sim$4 hours the dilution corrected abundances of PANs plateau. After $\sim$4 hours NO_x and HONO together account for a small fraction (<10%) of $\sum NO_y$, and $p$$NO_3$, PANs, and gas-phase organic nitrates become the dominant contributors to $\sum NO_y$, contributing on average $\sim$26 %, $\sim$37%, and $\sim$23%, respectively. Little to no enhancement of HNO_3 is typically observed in the near-source (< 6 hours of aging) wildfire smoke plumes (suggesting either rapid association with NH_3 (when favorable) to form NH_4NO_3 or effective scavenging by other heterogeneous aerosol chemistry).

2. Significant differences are observed between the Bear Trap Fire and Taylor Creek Fire smoke plumes. These two fires were successfully and repeatedly sampled in a pseudo-lagrangian fashion and both show $\sum NO_y$ conservation (within the uncertainties of the measurements) for the duration of the sampling. Variability in sampling conditions include differences in: proximity to the fire source, plume height, atmospheric conditions (temperature and relative humidity), MCE, and estimated OH concentration. The higher MCE Taylor Creek Fire smoke plume samples contain almost twice as much $\sum NO_y$ relative to CO than the Bear

Trap Fire smoke plume samples. The Taylor Creek Fire smoke plume, characterized by exceptionally low RH ($\sim$7%), warmer conditions, and low abundances of NH_3 ([46]) is the only young plume sampled in a pseudo-lagrangian fashion during WE-CAN that contains HNO_3 enhancements above background conditions.

3. The partitioning of $\sum NO_y$ in all the smoke-impacted samples intercepted during WE-CAN varies with altitude. These samples include smoke-impacted samples outside the pseudo-lagrangian sampling efforts and include influence from other NO_y sources. Below 3 km, the dominant $\sum NO_y$ species in this subset of summertime samples is HNO_3, and its contribution to the total $\sum NO_y$ below 5 km increases with age. Above 5 km, HNO_3 is only present in the smoke-free samples; within smoke there is higher NH_3 availability to form NH_4NO_3. Above 3 km, HONO is only elevated above the detection limit in young and medium smoke-impacted samples. NO_x abundances are comparable to those of $p$$NO_3$ in younger plumes above 3 km. The abundance of PANs increases with altitude in the smoke-impacted samples. Finally, the behavior of $p$$NO_3$ varies with altitude. Below 3 km, the relative abundance of $p$$NO_3$ is much lower than smoke samples intercepted at higher altitudes; abundances are typically < 2 ppbv (5.5 ug stdm-3). Between 3 and 5 km, the contribution of $p$$NO_3$ to $\sum NO_y$ is largely constant but coupled with an increasing contribution of HNO_3. Above 5 km, HNO_3 is below the detection limit in all age categories, and the relative contribution of $p$$NO_3$ to $\sum NO_y$ increases as the samples chemically age.

4. WE-CAN also sampled smoke from multiple fires mixed with anthropogenic emissions over the California Central Valley. In these mixed smoke plumes, predominantly sampled below 3 km, additional injections of anthropogenic NO_x (and secondary PAN) can be distinguished by examining relationships between these species and CH_3CN. For this specific day, injections of anthropogenic emissions provided additional NO_x, increasing the abundance by up to a factor of 4. Anthropogenic NO_x appears to contribute to additional PAN formation. The NO to NO_2 ratio in the smoke-filled Central Valley does not appear to be affected by injections of anthropogenic emissions during the afternoon.

We present the first analysis of CrIS PAN measurements over North America. We focus our analysis on summer 2018, aligning with *in situ* observations of wildfire smoke collected by the WE-CAN field intensive. Summer 2018 was a particularly active wildfire season, and thus we focus this first analysis of the new CrIS PAN data on the contribution of wildfire smoke to elevated PAN over the U.S.

5. CrIS is able to detect PAN and CO enhancements in smoke plumes from many individual wildfires during summer 2018. These observations also reflect large multi-state scale plumes of smoke containing elevated PAN and CO from regional sets of wildfires.
6. We segregate and examine the abundance of tropospheric average PAN in smoke-impacted CrIS retrievals using two different satellite-based attribution methods. The first is based on identifying CrIS retrievals within smoke plumes identified by the NOAA HMS. The second is based on elevated CO at specific pressure levels (680 and 510 hPa) in paired CrIS CO retrievals. Based on the former criteria, we estimate that during the study period approximately two thirds of the CrIS retrievals were smoke-impacted. Our CrIS-based criteria is conservative, identifying fewer retrievals as smoke-impacted in the mid-troposphere, where CrIS is sensitive to PAN. However, both methods indicate that smoke-impacted retrievals contain higher tropospheric-avergage PAN than smoke-free retrievals.
7. An analysis of smoke-impacted CrIS PAN retrievals over the entire study region suggests that wildfires are responsible for approximately $\sim$15 - 50% of the free tropospheric PAN over the western U.S. during summer months. The contribution of wildfire smoke to free tropospheric PAN generally increases with latitude. It is at a minimum over the Great Basin; however, we suspect that this region may also be challenging for the PAN retrieval due to the underlying sandy/rocky surface. This possibility is currently under investigation. An abundance of negative retrievals supports this hypothesis.
8. We use a specific case study of the Pole Creek Fire to demonstrate that when combined with favorable background conditions, the spatial resolution of CrIS is sufficient to observe the

chemical evolution of PAN in wildfire plumes. We estimate physical ages for each retrieval and compare them with the PAN NEMRs observed in fresh smoke plumes (*i.e.,* < 6 hours ages) during WE-CAN. We show that for the Pole Creek fire smoke plume, the PAN NEMRs increase from <0.1% to 0.35% in $\sim$ 3 - 4 hours of transport downwind from the fire source. Within the WE-CAN observations, PAN NEMRs increase from 0.15% to 0.39% in 3-4 hours of physical aging. The ability of CrIS to observe chemical evolution is in contrast to the ability of TES.

9. We use a second case study of the Carr Fire plume to show that CrIS is able to detect PAN and CO enhancements in plumes that have been transported several hours to days downwind from the fire source. We track smoke from the Carr Fire as it moves across several western U.S. states using a combination of forward and backward HYSPLIT trajectories.

10. Finally, we summarize PAN enhancements in smoke relative to CO (*i.e.,* NEMRs) calculated from CrIS retrievals, and compare them to those calculated from *in situ* data. The CrIS based NEMRs fall within the range of those observed during WE-CAN. A higher percentage of the smoke-impacted CrIS data have NEMRs near zero than the WE-CAN observations. These low NEMRs are largely associated with smoke-impacted retrievals with lower (higher) PAN (CO) mixing ratios.

Our analysis form the WE-CAN campaign provides a comprehensive look at the partitioning of $\sum \mathrm{NO}_y$ in wildfire smoke plumes and smoke-impacted samples over the western U.S. during summer 2018, providing organized data for the modeling community to further investigate the processes controlling the evolution of NO_y in smoke. Furthermore, this work reinforces the importance of wildfires as a source of PAN to the free troposphere over North America during summer months. It also demonstrates that CrIS measurements of PAN complement aircraft observations, and can be used to extend the analysis of recent observational campaigns. We envision two immediate next steps based on this work. We will compare our CrIS-based analysis of the contribution of wildfires to PAN abundances to an attribution based on chemical transport model simulations. We also plan and extrapolate the contribution of PAN from wildfires to ozone production.

Bibliography

[1] P. J. Crutzen and M. O. Andreae. Biomass Burning in the Tropics: Impact on Atmospheric Chemistry and Biogeochemical Cycles. *Science*, 250(4988):1669–1678, December 1990.

[2] Philip M. Fearnside, Niwton Leal, and Fernando Moreira Fernandes. Rainforest burning and the global carbon budget: Biomass, combustion efficiency, and charcoal formation in the Brazilian Amazon. *Journal of Geophysical Research*, 98(D9):16733, 1993.

[3] Tami C. Bond. A technology-based global inventory of black and organic carbon emissions from combustion. *Journal of Geophysical Research*, 109(D14):D14203, 2004.

[4] S. K. Akagi, R. J. Yokelson, C. Wiedinmyer, M. J. Alvarado, J. S. Reid, T. Karl, J. D. Crounse, and P. O. Wennberg. Emission factors for open and domestic biomass burning for use in atmospheric models. *Atmospheric Chemistry and Physics*, 11(9):4039–4072, May 2011.

[5] Matthew D. Hurteau, Anthony L. Westerling, Christine Wiedinmyer, and Benjamin P. Bryant. Projected Effects of Climate and Development on California Wildfire Emissions through 2100. *Environmental Science & Technology*, page 140203132416003, February 2014.

[6] Melita Keywood, Maria Kanakidou, Andreas Stohl, Frank Dentener, Giacomo Grassi, C. P. Meyer, Kjetil Torseth, David Edwards, Anne M. Thompson, Ulrike Lohmann, and John Burrows. Fire in the Air: Biomass Burning Impacts in a Changing Climate. *Critical Reviews in Environmental Science and Technology*, 43(1):40–83, January 2013.

[7] Max A. Moritz, Marc-André Parisien, Enric Batllori, Meg A. Krawchuk, Jeff Van Dorn, David J. Ganz, and Katharine Hayhoe. Climate change and disruptions to global fire activity. *Ecosphere*, 3(6):art49, June 2012.

[8] M. Scholze, W. Knorr, N. W. Arnell, and I. C. Prentice. A climate-change risk analysis for world ecosystems. *Proceedings of the National Academy of Sciences*, 103(35):13116–13120, August 2006.

[9] Anthony LeRoy Westerling. Increasing western US forest wildfire activity: sensitivity to changes in the timing of spring. *Philosophical Transactions of the Royal Society B: Biological Sciences*, 371(1696):20150178, June 2016.

[10] A. Park Williams, John T. Abatzoglou, Alexander Gershunov, Janin Guzman-Morales, Daniel A. Bishop, Jennifer K. Balch, and Dennis P. Lettenmaier. Observed Impacts of Anthropogenic Climate Change on Wildfire in California. *Earth's Future*, 7(8):892–910, August 2019.

[11] Xu Yue, Loretta J. Mickley, Jennifer A. Logan, and Jed O. Kaplan. Ensemble projections of wildfire activity and carbonaceous aerosol concentrations over the western United States in the mid-21st century. *Atmospheric Environment*, 77:767–780, October 2013.

[12] S. K. Akagi, J. S. Craven, J. W. Taylor, G. R. McMeeking, R. J. Yokelson, I. R. Burling, S. P. Urbanski, C. E. Wold, J. H. Seinfeld, H. Coe, M. J. Alvarado, and D. R. Weise. Evolution of trace gases and particles emitted by a chaparral fire in California. *Atmospheric Chemistry and Physics*, 12(3):1397–1421, February 2012.

[13] Xiaoxi Liu, Y. Zhang, L. G. Huey, R. J. Yokelson, Y. Wang, J. L. Jimenez, P. Campuzano-Jost, A. J. Beyersdorf, D. R. Blake, Y. Choi, J. M. St. Clair, J. D. Crounse, D. A. Day, G. S. Diskin, A. Fried, S. R. Hall, T. F. Hanisco, L. E. King, S. Meinardi, T. Mikoviny, B. B. Palm, J. Peischl, A. E. Perring, I. B. Pollack, T. B. Ryerson, G. Sachse, J. P. Schwarz, I. J. Simpson, D. J. Tanner, K. L. Thornhill, K. Ullmann, R. J. Weber, P. O. Wennberg, A. Wisthaler, G. M. Wolfe, and L. D. Ziemba. Agricultural fires in the southeastern U.S. during SEAC ^{4} RS: Emissions of trace gases and particles and evolution of ozone, reactive nitrogen, and organic aerosol: Agricultural Fires in the SE US. *Journal of Geophysical Research: Atmospheres*, 121(12):7383–7414, June 2016.

[14] Qiaoyun Peng, Brett B. Palm, Kira E. Melander, Ben H. Lee, Samuel R. Hall, Kirk Ullmann, Teresa Campos, Andrew J. Weinheimer, Eric C. Apel, Rebecca S. Hornbrook, Alan J. Hills,

Denise D. Montzka, Frank Flocke, Lu Hu, Wade Permar, Catherine Wielgasz, Jakob Lindaas, Ilana B. Pollack, Emily V. Fischer, Timothy H. Bertram, and Joel A. Thornton. HONO Emissions from Western U.S. Wildfires Provide Dominant Radical Source in Fresh Wildfire Smoke. *Environmental Science & Technology*, 54(10):5954–5963, May 2020.

[15] M. J. Alvarado, J. A. Logan, J. Mao, E. Apel, D. Riemer, D. Blake, R. C. Cohen, K.-E. Min, A. E. Perring, E. C. Browne, P. J. Wooldridge, G. S. Diskin, G. W. Sachse, H. Fuelberg, W. R. Sessions, D. L. Harrigan, G. Huey, J. Liao, A. Case-Hanks, J. L. Jimenez, M. J. Cubison, S. A. Vay, A. J. Weinheimer, D. J. Knapp, D. D. Montzka, F. M. Flocke, I. B. Pollack, P. O. Wennberg, A. Kurten, J. Crounse, J. M. St. Clair, A. Wisthaler, T. Mikoviny, R. M. Yantosca, C. C. Carouge, and P. Le Sager. Nitrogen oxides and PAN in plumes from boreal fires during ARCTAS-B and their impact on ozone: an integrated analysis of aircraft and satellite observations. *Atmospheric Chemistry and Physics*, 10(20):9739–9760, October 2010.

[16] S. K. Akagi, J. S. Craven, J. W. Taylor, G. R. McMeeking, R. J. Yokelson, I. R. Burling, S. P. Urbanski, C. E. Wold, J. H. Seinfeld, H. Coe, M. J. Alvarado, and D. R. Weise. Evolution of trace gases and particles emitted by a chaparral fire in California. *Atmospheric Chemistry and Physics*, 12(3):1397–1421, February 2012.

[17] R J Yokelson, J D Crounse, P F DeCarlo, T Karl, S Urbanski, E Atlas, T Campos, Y Shinozuka, V Kapustin, A D Clarke, A Weinheimer, D J Knapp, D D Montzka, J Holloway, P Weibring, F Flocke, W Zheng, D Toohey, P O Wennberg, C Wiedinmyer, L Mauldin, A Fried, D Richter, J Walega, J L Jimenez, K Adachi, P R Buseck, S R Hall, and R Shetter. Emissions from biomass burning in the Yucatan. *Atmos. Chem. Phys.*, page 28, 2009.

[18] M. Val Martín, R. E. Honrath, R. C. Owen, G. Pfister, P. Fialho, and F. Barata. Significant enhancements of nitrogen oxides, black carbon, and ozone in the North Atlantic lower free troposphere resulting from North American boreal wildfires: WILDFIRE IMPACTS ON BC, NO $_x$, NO $_y$ AND O $_3$. *Journal of Geophysical Research: Atmospheres*, 111(D23), December 2006.

[19] Hanwant B. Singh. Reactive nitrogen in the troposphere. *Environmental Science & Technology*, 21(4):320–327, April 1987.

[20] Hanwant B. Singh and Philip L. Hanst. Peroxyacetyl nitrate (PAN) in the unpolluted atmosphere: An important reservoir for nitrogen oxides. *Geophysical Research Letters*, 8(8):941–944, August 1981.

[21] E. V. Fischer, D. A. Jaffe, D. R. Reidmiller, and L. Jaeglé. Meteorological controls on observed peroxyacetyl nitrate at Mount Bachelor during the spring of 2008. *Journal of Geophysical Research*, 115(D3):D03302, February 2010.

[22] Jürgen M. Lobert, Dieter H. Scharffe, Wei M. Hao, and Paul J. Crutzen. Importance of biomass burning in the atmospheric budgets of nitrogen-containing gases. *Nature*, 346(6284):552–554, August 1990.

[23] Thomas A. Kuhlbusch, Jürgen M. Lobert, Paul J. Crutzen, and Peter Warneck. Molecular nitrogen emissions from denitrification during biomass burning. *Nature*, 351(6322):135–137, May 1991.

[24] James M. Roberts, Chelsea E. Stockwell, Robert J. Yokelson, Joost de Gouw, Yong Liu, Vanessa Selimovic, Abigail R. Koss, Kanako Sekimoto, Matthew M. Coggon, Bin Yuan, Kyle J. Zarzana, Steven S. Brown, Cristina Santin, Stefan H. Doerr, and Carsten Warneke. The nitrogen budget of laboratory-simulated western U.S. wildfires during the FIREX 2016 FireLab study. preprint, Gases/Laboratory Studies/Troposphere/Chemistry (chemical composition and reactions), February 2020.

[25] Peter Glarborg, James A. Miller, Branko Ruscic, and Stephen J. Klippenstein. Modeling nitrogen chemistry in combustion. *Progress in Energy and Combustion Science*, 67:31–68, July 2018.

[26] Karl-Martin Hansson, Jessica Samuelsson, Claes Tullin, and Lars-Erik Åmand. Formation of HNCO, HCN, and NH3 from the pyrolysis of bark and nitrogen-containing model compounds. *Combustion and Flame*, 137(3):265–277, May 2004.

[27] Qiangqiang Ren and Changsui Zhao. NO $_x$ and N $_2$ O Precursors from Biomass Pyrolysis: Nitrogen Transformation from Amino Acid. *Environmental Science & Technology*, 46(7):4236–4240, April 2012.

[28] Nicole K. Scharko, Ashley M. Oeck, Tanya L. Myers, Russell G. Tonkyn, Catherine A. Banach, Stephen P. Baker, Emily N. Lincoln, Joey Chong, Bonni M. Corcoran, Gloria M. Burke, Roger D. Ottmar, Joseph C. Restaino, David R. Weise, and Timothy J. Johnson. Gas-phase pyrolysis products emitted by prescribed fires in pine forests with a shrub understory in the southeastern United States. *Atmospheric Chemistry and Physics*, 19(15):9681–9698, August 2019.

[29] Meinrat O. Andreae. Emission of trace gases and aerosols from biomass burning &#8211;An updated assessment. preprint, Biosphere Interactions/Field Measurements/Troposphere/Chemistry (chemical composition and reactions), April 2019.

[30] M. O. Andreae and P. Merlet. Emission of trace gases and aerosols from biomass burning. *Global Biogeochemical Cycles*, 15(4):955–966, December 2001.

[31] Jon G. Goode, Robert J. Yokelson, Darold E. Ward, Ronald A. Susott, Ronald E. Babbitt, Mary Ann Davies, and Wei Min Hao. Measurements of excess O $_3$, CO $_2$, CO, CH $_4$, C $_2$ H $_4$, C $_2$ H $_2$, HCN, NO, NH $_3$, HCOOH, CH $_3$ COOH, HCHO, and CH $_3$ OH in 1997 Alaskan biomass burning plumes by airborne Fourier transform infrared spectroscopy (AFTIR). *Journal of Geophysical Research: Atmospheres*, 105(D17):22147–22166, September 2000.

[32] Gavin R. McMeeking, Sonia M. Kreidenweis, Stephen Baker, Christian M. Carrico, Judith C. Chow, Jeffrey L. Collett, Wei Min Hao, Amanda S. Holden, Thomas W. Kirchstetter,

William C. Malm, Hans Moosmüller, Amy P. Sullivan, and Cyle E. Wold. Emissions of trace gases and aerosols during the open combustion of biomass in the laboratory. *Journal of Geophysical Research*, 114(D19):D19210, October 2009.

[33] Robert J. Yokelson, David W. T. Griffith, and Darold E. Ward. Open-path Fourier transform infrared studies of large-scale laboratory biomass fires. *Journal of Geophysical Research: Atmospheres*, 101(D15):21067–21080, September 1996.

[34] I. R. Burling, R. J. Yokelson, D. W. T. Griffith, T. J. Johnson, P. Veres, J. M. Roberts, C. Warneke, S. P. Urbanski, J. Reardon, D. R. Weise, W. M. Hao, and J. de Gouw. Laboratory measurements of trace gas emissions from biomass burning of fuel types from the southeastern and southwestern United States. *Atmospheric Chemistry and Physics*, 10(22):11115–11130, November 2010.

[35] Nicole L. Briggs, Daniel A. Jaffe, Honglian Gao, Jonathan R. Hee, Pao M. Baylon, Qi Zhang, Shan Zhou, Sonya C. Collier, Paul D. Sampson, and Robert A. Cary. Particulate Matter, Ozone, and Nitrogen Species in Aged Wildfire Plumes Observed at the Mount Bachelor Observatory. *Aerosol and Air Quality Research*, 16(12):3075–3087, 2017.

[36] Jakob Lindaas, Delphine K. Farmer, Ilana B. Pollack, Andrew Abeleira, Frank Flocke, Rob Roscioli, Scott Herndon, and Emily V. Fischer. The impact of aged wildfire smoke on atmospheric composition and ozone in the Colorado Front Range in summer 2015. preprint, Gases/Field Measurements/Troposphere/Chemistry (chemical composition and reactions), March 2017.

[37] H.B. Singh, C. Cai, A. Kaduwela, A. Weinheimer, and A. Wisthaler. Interactions of fire emissions and urban pollution over California: Ozone formation and air quality simulations. *Atmospheric Environment*, 56:45–51, September 2012.

[38] Chenxia Cai, Sarika Kulkarni, Zhan Zhao, Ajith P. Kaduwela, Jeremy C. Avise, John A. DaMassa, Hanwant B. Singh, Andrew J. Weinheimer, Ronald C. Cohen, Glenn S. Diskin,

Paul Wennberg, Jack E. Dibb, Greg Huey, Armin Wisthaler, Jose L. Jimenez, and Michael J. Cubison. Simulating reactive nitrogen, carbon monoxide, and ozone in California during ARCTAS-CARB 2008 with high wildfire activity. *Atmospheric Environment*, 128:28–44, March 2016.

[39] R J Yokelson, J D Crounse, P F DeCarlo, T Karl, S Urbanski, E Atlas, T Campos, Y Shinozuka, V Kapustin, A D Clarke, A Weinheimer, D J Knapp, D D Montzka, J Holloway, P Weibring, F Flocke, W Zheng, D Toohey, P O Wennberg, C Wiedinmyer, L Mauldin, A Fried, D Richter, J Walega, J L Jimenez, K Adachi, P R Buseck, S R Hall, and R Shetter. Emissions from biomass burning in the Yucatan. *Atmos. Chem. Phys.*, page 28, 2009.

[40] M. J. Alvarado, C. R. Lonsdale, R. J. Yokelson, S. K. Akagi, H. Coe, J. S. Craven, E. V. Fischer, G. R. McMeeking, J. H. Seinfeld, T. Soni, J. W. Taylor, D. R. Weise, and C. E. Wold. Investigating the links between ozone and organic aerosol chemistry in a biomass burning plume from a prescribed fire in California chaparral. *Atmospheric Chemistry and Physics*, 15(12):6667–6688, June 2015.

[41] Julieta Juncosa Calahorrano, Jakob Lindaas, Katelyn O'Dell, Brett B. Palm, Qiaoyun Peng, Frank Flocke, Ilana B. Pollack, Lauren A. Garofalo, Delphine K. Farmer, Jeffrey R. Pierce, Jr. Jeffrey L. Collett, Andrew Weinheimer, Teresa Campos, Rebecca S. Hornbrook, Matson A. Pothier, Eric C. Apel, Wade Permar, Lu Hu, Alan J. Hills, Deedee Montzka, Geoff Tyndall, Joel A. Thornton, , and Emily V. Fischer. Daytime oxidized reactive nitrogen partitioning in western U.S. wildfire smoke plumes. *Journal of Geophysical Research: Atmospheres*, n review.

[42] E. V. Fischer, D. J. Jacob, R. M. Yantosca, M. P. Sulprizio, D. B. Millet, J. Mao, F. Paulot, H. B. Singh, A. Roiger, L. Ries, R.W. Talbot, K. Dzepina, and S. Pandey Deolal. Atmospheric peroxyacetyl nitrate (PAN): a global budget and source attribution. *Atmospheric Chemistry and Physics*, 14(5):2679–2698, March 2014.

[43] Nicole L. Briggs, Daniel A. Jaffe, Honglian Gao, Jonathan R. Hee, Pao M. Baylon, Qi Zhang, Shan Zhou, Sonya C. Collier, Paul D. Sampson, and Robert A. Cary. Particulate Matter, Ozone, and Nitrogen Species in Aged Wildfire Plumes Observed at the Mount Bachelor Observatory. *Aerosol and Air Quality Research*, 16(12):3075–3087, 2017.

[44] P. Baylon, D.A. Jaffe, N.L. Wigder, H. Gao, and J. Hee. Ozone enhancement in western US wildfire plumes at the Mt. Bachelor Observatory: The role of NOx. *Atmospheric Environment*, 109:297–304, May 2015.

[45] Emily V. Fischer, Liye Zhu, Vivienne H. Payne, John R. Worden, Zhe Jiang, Susan S. Kulawik, Steven Brey, Arsineh Hecobian, Daniel Gombos, Karen Cady-Pereira, and Frank Flocke. Using TES retrievals to investigate PAN in North American biomass burning plumes. *Atmospheric Chemistry and Physics*, 18(8):5639–5653, April 2018.

[46] Jakob Lindaas, Ilana B. Pollack, Lauren A. Garofalo, Matson A. Pothier, Delphine K, Farmer, Sonia M. Kreidenweis, Teresa L. Campos, Frank Flocke, Andrew J. Weinheimer, Denise D. Montzka, Geoffrey S. Tyndall, Brett B. Palm, Qiaoyun Peng, Joel A. Thornton amd Wade Permar, Catherine Wielgasz, Lu Hu, Roger D. Ottmar, Joseph C. Restaino, Andrew T. Hudak, I-Ting Ku, Yong Zhou, Barkley C. Sive, Amy Sullivan, Jr. Jeffrey L. Collett, and Emily V. Fischer. Emissions of reactive nitrogen from western U.S. wildfires during summer 2018. *Journal of Geophysical Research: Atmospheres*, in review.

[47] H.B. Singh, B.E. Anderson, W.H. Brune, C. Cai, R.C. Cohen, J.H. Crawford, M.J. Cubison, E.P. Czech, L. Emmons, and H.E. Fuelberg. Pollution influences on atmospheric composition and chemistry at high northern latitudes: Boreal and California forest fire emissions. *Atmospheric Environment*, 44(36):4553–4564, November 2010.

[48] W. Zheng, F. M. Flocke, G. S. Tyndall, A. Swanson, J. J. Orlando, J. M. Roberts, L. G. Huey, and D. J. Tanner. Characterization of a thermal decomposition chemical ionization mass spectrometer for the measurement of peroxy acyl nitrates (PANs) in the atmosphere. *Atmospheric Chemistry and Physics Discussions*, 11(3):8461–8513, March 2011.

[49] Darlene L. Slusher. A thermal dissociation–chemical ionization mass spectrometry (TD-CIMS) technique for the simultaneous measurement of peroxyacyl nitrates and dinitrogen pentoxide. *Journal of Geophysical Research*, 109(D19):D19315, 2004.

[50] Ben H. Lee, Felipe D. Lopez-Hilfiker, Claudia Mohr, Theo Kurtén, Douglas R. Worsnop, and Joel A. Thornton. An Iodide-Adduct High-Resolution Time-of-Flight Chemical-Ionization Mass Spectrometer: Application to Atmospheric Inorganic and Organic Compounds. *Environmental Science & Technology*, 48(11):6309–6317, June 2014.

[51] Ben H. Lee, Felipe D. Lopez-Hilfiker, Patrick R. Veres, Erin E. McDuffie, Dorothy L. Fibiger, Tamara L. Sparks, Carlena J. Ebben, Jaime R. Green, Jason C. Schroder, Pedro Campuzano-Jost, Siddharth Iyer, Emma L. D'Ambro, Siegfried Schobesberger, Steven S. Brown, Paul J. Wooldridge, Ronald C. Cohen, Marc N. Fiddler, Solomon Bililign, Jose L. Jimenez, Theo Kurtén, Andrew J. Weinheimer, Lyatt Jaegle, and Joel A. Thornton. Flight Deployment of a High-Resolution Time-of-Flight Chemical Ionization Mass Spectrometer: Observations of Reactive Halogen and Nitrogen Oxide Species. *Journal of Geophysical Research: Atmospheres*, July 2018.

[52] Brett B. Palm, Xiaoxi Liu, Jose L. Jimenez, and Joel A. Thornton. Performance of a new coaxial ion–molecule reaction region for low-pressure chemical ionization mass spectrometry with reduced instrument wall interactions. *Atmospheric Measurement Techniques*, 12(11):5829–5844, November 2019.

[53] Ben H. Lee, Claudia Mohr, Felipe D. Lopez-Hilfiker, Anna Lutz, Mattias Hallquist, Lance Lee, Paul Romer, Ronald C. Cohen, Siddharth Iyer, Theo Kurtén, Weiwei Hu, Douglas A. Day, Pedro Campuzano-Jost, Jose L. Jimenez, Lu Xu, Nga Lee Ng, Hongyu Guo, Rodney J. Weber, Robert J. Wild, Steven S. Brown, Abigail Koss, Joost de Gouw, Kevin Olson, Allen H. Goldstein, Roger Seco, Saewung Kim, Kevin McAvey, Paul B. Shepson, Tim Starn, Karsten Baumann, Eric S. Edgerton, Jiumeng Liu, John E. Shilling, David O. Miller, William Brune, Siegfried Schobesberger, Emma L. D'Ambro, and Joel A. Thornton. Highly functionalized

organic nitrates in the southeast United States: Contribution to secondary organic aerosol and reactive nitrogen budgets. *Proceedings of the National Academy of Sciences*, 113(6):1516–1521, February 2016.

[54] Benjamin Lebegue, Martina Schmidt, Michel Ramonet, Benoit Wastine, Camille Yver Kwok, Olivier Laurent, Sauveur Belviso, Ali Guemri, Carole Philippon, Jeremiah Smith, and Sebastien Conil. Comparison of nitrous oxide (N_2O) analyzers for high-precision measurements of atmospheric mole fractions. *Atmospheric Measurement Techniques*, 9(3):1221–1238, March 2016.

[55] B.A. Ridley and F.E. Grahek. A small, low flow, high sensitivity reaction vessel for no/o3 chemiluminescence detectors. *Journal of Atmospheric and Oceanic Technology*, pages 307–311, April 1990.

[56] Peter F. DeCarlo, Joel R. Kimmel, Achim Trimborn, Megan J. Northway, John T. Jayne, Allison C. Aiken, Marc Gonin, Katrin Fuhrer, Thomas Horvath, Kenneth S. Docherty, Doug R. Worsnop, and Jose L. Jimenez. Field-Deployable, High-Resolution, Time-of-Flight Aerosol Mass Spectrometer. *Analytical Chemistry*, 78(24):8281–8289, December 2006.

[57] Roya Bahreini, Edward J. Dunlea, Brendan M. Matthew, Craig Simons, Kenneth S. Docherty, Peter F. DeCarlo, Jose L. Jimenez, Charles A. Brock, and Ann M. Middlebrook. Design and Operation of a Pressure-Controlled Inlet for Airborne Sampling with an Aerodynamic Aerosol Lens. *Aerosol Science and Technology*, 42(6):465–471, April 2008.

[58] Lauren A. Garofalo, Matson A. Pothier, Ezra J. T. Levin, Teresa Campos, Sonia M. Kreidenweis, and Delphine K. Farmer. Emission and Evolution of Submicron Organic Aerosol in Smoke from Wildfires in the Western United States. *ACS Earth and Space Chemistry*, 3(7):1237–1247, July 2019.

[59] R. Bahreini, B. Ervens, A. M. Middlebrook, C. Warneke, J. A. de Gouw, P. F. DeCarlo, J. L. Jimenez, C. A. Brock, J. A. Neuman, T. B. Ryerson, H. Stark, E. Atlas, J. Brioude,

A. Fried, J. S. Holloway, J. Peischl, D. Richter, J. Walega, P. Weibring, A. G. Wollny, and F. C. Fehsenfeld. Organic aerosol formation in urban and industrial plumes near Houston and Dallas, Texas. *Journal of Geophysical Research*, 114:D00F16, August 2009.

[60] D. K. Farmer, A. Matsunaga, K. S. Docherty, J. D. Surratt, J. H. Seinfeld, P. J. Ziemann, and J. L. Jimenez. Response of an aerosol mass spectrometer to organonitrates and organosulfates and implications for atmospheric chemistry. *Proceedings of the National Academy of Sciences*, 107(15):6670–6675, April 2010.

[61] E. C. Apel. A fast-GC/MS system to measure C $_2$ to C $_4$ carbonyls and methanol aboard aircraft. *Journal of Geophysical Research*, 108(D20):8794, 2003.

[62] E. C. Apel, R. S. Hornbrook, A. J. Hills, N. J. Blake, M. C. Barth, A. Weinheimer, C. Cantrell, S. A. Rutledge, B. Basarab, J. Crawford, G. Diskin, C. R. Homeyer, T. Campos, F. Flocke, A. Fried, D. R. Blake, W. Brune, I. Pollack, J. Peischl, T. Ryerson, P. O. Wennberg, J. D. Crounse, A. Wisthaler, T. Mikoviny, G. Huey, B. Heikes, D. O'Sullivan, and D. D. Riemer. Upper tropospheric ozone production from lightning NO $_x$ -impacted convection: Smoke ingestion case study from the DC3 campaign. *Journal of Geophysical Research: Atmospheres*, 120(6):2505–2523, March 2015.

[63] Kanako Sekimoto, Shao-Meng Li, Bin Yuan, Abigail Koss, Matthew Coggon, Carsten Warneke, and Joost de Gouw. Calculation of the sensitivity of proton-transfer-reaction mass spectrometry (PTR-MS) for organic trace gases using molecular properties. *International Journal of Mass Spectrometry*, 421:71–94, October 2017.

[64] Bin Yuan, Abigail R. Koss, Carsten Warneke, Matthew Coggon, Kanako Sekimoto, and Joost A. de Gouw. Proton-Transfer-Reaction Mass Spectrometry: Applications in Atmospheric Sciences. *Chemical Reviews*, 117(21):13187–13229, November 2017.

[65] Tracey Holloway, Hiram Levy, and Prasad Kasibhatla. Global distribution of carbon monoxide. *Journal of Geophysical Research: Atmospheres*, 105(D10):12123–12147, May 2000.

[66] Katelyn O'Dell, Rebecca S. Hornbrook, Wade Permar, Ezra J.T. Levin, Lauren A. Garofalo, Eric C. Apel, Nicola J. Blake, Alex Jarnot, Matson A. Pothier, Delphine K. Farmer, Lu Hu, Teresa Campos, Bonne Ford, Jeffrey R. Pierce, and Emily V. Fischer. Hazardous air pollutants in fresh and aged western US wildfire smoke and implications for long-term exposure. *Environmental Science and Technology*, submitted.

[67] I. Kind, T. Berndt, O. Böge, and W. Rolle. Gas-phase rate constants for the reaction of NO3 radicals with furan and methyl-substituted furans. *Chemical Physics Letters*, 256(6):679–683, July 1996.

[68] Bin Xiang, Prabir K. Patra, Stephen A. Montzka, Scot M. Miller, James W. Elkins, Fred L. Moore, Elliot L. Atlas, Ben R. Miller, Ray F. Weiss, Ronald G. Prinn, and Steven C. Wofsy. Global emissions of refrigerants HCFC-22 and HFC-134a: Unforeseen seasonal contributions. *Proceedings of the National Academy of Sciences*, 111(49):17379–17384, December 2014.

[69] Dejian Fu, Kevin W. Bowman, Helen M. Worden, Vijay Natraj, John R. Worden, Shanshan Yu, Pepijn Veefkind, Ilse Aben, Jochen Landgraf, Larrabee Strow, and Yong Han. High-resolution tropospheric carbon monoxide profiles retrieved from CrIS and TROPOMI. *Atmospheric Measurement Techniques*, 9(6):2567–2579, June 2016.

[70] K.W. Bowman, C.D. Rodgers, S.S. Kulawik, J. Worden, E. Sarkissian, G. Osterman, T. Steck, Ming Lou, A. Eldering, M. Shephard, H. Worden, M. Lampel, S. Clough, P. Brown, C. Rinsland, M. Gunson, and R. Beer. Tropospheric emission spectrometer: retrieval method and error analysis. *IEEE Transactions on Geoscience and Remote Sensing*, 44(5):1297–1307, May 2006.

[71] Reinhard Beer, Kevin W Bowman, Patrick D Brown, Shepard A Clough, Aaron Goldman, Daniel J Jacob, Jennifer A Logan, Mingzhao Luo, Frank J Murcray, David M Rider, Curtis P Rinsland, Clive D Rodgers, Stanley P Sander, Eugene A Ustinov, Helen M Worden, and Marguerite Syvertson. TROPOSPHERIC EMISSION SPECTROMETER (TES). page 112.

[72] V. H. Payne, M. J. Alvarado, K. E. Cady-Pereira, J. R. Worden, S. S. Kulawik, and E. V. Fischer. Satellite observations of peroxyacetyl nitrate from the Aura Tropospheric Emission Spectrometer. *Atmospheric Measurement Techniques*, 7(11):3737–3749, November 2014.

[73] Glenn D. Rolph, Roland R. Draxler, Ariel F. Stein, Albion Taylor, Mark G. Ruminski, Shobha Kondragunta, Jian Zeng, Ho-Chun Huang, Geoffrey Manikin, Jeffery T. McQueen, and Paula M. Davidson. Description and Verification of the NOAA Smoke Forecasting System: The 2007 Fire Season. *Weather and Forecasting*, 24(2):361–378, April 2009.

[74] Mark Ruminski, Shobha Kondragunta, Roland Draxler, Jian Zeng, and Auth Rm. Recent Changes to the Hazard Mapping System. page 15.

[75] W. Schroeder, M. Ruminski, I. Csiszar, L. Giglio, E. Prins, C. Schmidt, and J. Morisette. Validation analyses of an operational fire monitoring product: The Hazard Mapping System. *International Journal of Remote Sensing*, 29(20):6059–6066, October 2008.

[76] Steven J. Brey, Mark Ruminski, Samuel A. Atwood, and Emily V. Fischer. Connecting smoke plumes to sources using Hazard Mapping System (HMS) smoke and fire location data over North America. *Atmospheric Chemistry and Physics*, 18(3):1745–1761, February 2018.

[77] S. K. Akagi, J. S. Craven, J. W. Taylor, G. R. McMeeking, R. J. Yokelson, I. R. Burling, S. P. Urbanski, C. E. Wold, J. H. Seinfeld, H. Coe, M. J. Alvarado, and D. R. Weise. Evolution of trace gases and particles emitted by a chaparral fire in California. *Atmospheric Chemistry and Physics*, 12(3):1397–1421, February 2012.

[78] D. J. Jacob, S. C. Wofsy, P. S. Bakwin, S.-M. Fan, R. C. Harriss, R. W. Talbot, J. D. Bradshaw, S. T. Sandholm, H. B. Singh, E. V. Browell, G. L. Gregory, G. W. Sachse, M. C. Shipham, D. R. Blake, and D. R. Fitzjarrald. Summertime photochemistry of the troposphere at high northern latitudes. *Journal of Geophysical Research*, 97(D15):16421, 1992.

[79] Peter V. Hobbs, Parikhit Sinha, Robert J. Yokelson, Ted J. Christian, Donald R. Blake, Song Gao, Thomas W. Kirchstetter, Tica Novakov, and Peter Pilewskie. Evolution of gases and

particles from a savanna fire in South Africa: EVOLUTION OF GASES AND PARTICLES. *Journal of Geophysical Research: Atmospheres*, 108(D13):n/a–n/a, July 2003.

[80] Jörg Trentmann. An analysis of the chemical processes in the smoke plume from a savanna fire. *Journal of Geophysical Research*, 110(D12):D12301, 2005.

[81] J.H. Seinfield and S.N. Pandis. *Atmospheric chemistry and physics: From air pollution to climate change*. J. Wiley, Hoboken, NJ, USA:, 2006.

[82] A. Tabazadeh, M. Z. Jacobson, H. B. Singh, O. B. Toon, J. S. Lin, R. B. Chatfield, A. N. Thakur, R. W. Talbot, and J. E. Dibb. Nitric acid scavenging by mineral and biomass burning aerosols. *Geophysical Research Letters*, 25(22):4185–4188, November 1998.

[83] E. C. Browne, A. E. Perring, P. J. Wooldridge, E. Apel, S. R. Hall, L. G. Huey, J. Mao, K. M. Spencer, J. M. St. Clair, A. J. Weinheimer, A. Wisthaler, and R. C. Cohen. Global and regional effects of the photochemistry of CH $_3$ O $_2$ NO $_2$: evidence from ARCTAS. *Atmospheric Chemistry and Physics*, 11(9):4209–4219, May 2011.

[84] J. B. Gilman, B. M. Lerner, W. C. Kuster, P. D. Goldan, C. Warneke, P. R. Veres, J. M. Roberts, J. A. de Gouw, I. R. Burling, and R. J. Yokelson. Biomass burning emissions and potential air quality impacts of volatile organic compounds and other trace gases from fuels common in the US. *Atmospheric Chemistry and Physics*, 15(24):13915–13938, December 2015.

[85] L. E. Hatch, W. Luo, J. F. Pankow, R. J. Yokelson, C. E. Stockwell, and K. C. Barsanti. Identification and quantification of gaseous organic compounds emitted from biomass burning using two-dimensional gas chromatography–time-of-flight mass spectrometry. *Atmospheric Chemistry and Physics*, 15(4):1865–1899, February 2015.

[86] Abigail R. Koss, Kanako Sekimoto, Jessica B. Gilman, Vanessa Selimovic, Matthew M. Coggon, Kyle J. Zarzana, Bin Yuan, Brian M. Lerner, Steven S. Brown, Jose L. Jimenez, Jordan Krechmer, James M. Roberts, Carsten Warneke, Robert J. Yokelson, and Joost de Gouw.

Non-methane organic gas emissions from biomass burning: identification, quantification, and emission factors from PTR-ToF during the FIREX 2016 laboratory experiment. *Atmospheric Chemistry and Physics*, 18(5):3299–3319, March 2018.

[87] C. E. Stockwell, P. R. Veres, J. Williams, and R. J. Yokelson. Characterization of biomass burning emissions from cooking fires, peat, crop residue, and other fuels with high-resolution proton-transfer-reaction time-of-flight mass spectrometry. *Atmospheric Chemistry and Physics*, 15(2):845–865, January 2015.

[88] Matthew M. Coggon, Patrick R. Veres, Bin Yuan, Abigail Koss, Carsten Warneke, Jessica B. Gilman, Brian M. Lerner, Jeff Peischl, Kenneth C. Aikin, Chelsea E. Stockwell, Lindsay E. Hatch, Thomas B. Ryerson, James M. Roberts, Robert J. Yokelson, and Joost A. de Gouw. Emissions of nitrogen-containing organic compounds from the burning of herbaceous and arboraceous biomass: Fuel composition dependence and the variability of commonly used nitrile tracers: ORGANIC NITROGEN IN SMOKE. *Geophysical Research Letters*, 43(18):9903–9912, September 2016.

[89] Xiaoxi Liu, L. Gregory Huey, Robert J. Yokelson, Vanessa Selimovic, Isobel J. Simpson, Markus Müller, Jose L. Jimenez, Pedro Campuzano-Jost, Andreas J. Beyersdorf, Donald R. Blake, Zachary Butterfield, Yonghoon Choi, John D. Crounse, Douglas A. Day, Glenn S. Diskin, Manvendra K. Dubey, Edward Fortner, Thomas F. Hanisco, Weiwei Hu, Laura E. King, Lawrence Kleinman, Simone Meinardi, Tomas Mikoviny, Timothy B. Onasch, Brett B. Palm, Jeff Peischl, Ilana B. Pollack, Thomas B. Ryerson, Glen W. Sachse, Arthur J. Sedlacek, John E. Shilling, Stephen Springston, Jason M. St. Clair, David J. Tanner, Alexander P. Teng, Paul O. Wennberg, Armin Wisthaler, and Glenn M. Wolfe. Airborne measurements of western U.S. wildfire emissions: Comparison with prescribed burning and air quality implications. *Journal of Geophysical Research: Atmospheres*, 122(11):6108–6129, June 2017.

[90] H.B. Singh, C. Cai, A. Kaduwela, A. Weinheimer, and A. Wisthaler. Interactions of fire emissions and urban pollution over California: Ozone formation and air quality simulations. *Atmospheric Environment*, 56:45–51, September 2012.

[91] J. A. de Gouw, C. Warneke, A. Stohl, A. G. Wollny, C. A. Brock, O. R. Cooper, J. S. Holloway, M. Trainer, F. C. Fehsenfeld, E. L. Atlas, S. G. Donnelly, V. Stroud, and A. Lueb. Volatile organic compounds composition of merged and aged forest fire plumes from Alaska and western Canada: VOCS IN AGED FOREST FIRE PLUMES. *Journal of Geophysical Research: Atmospheres*, 111(D10):n/a–n/a, May 2006.

[92] A Stelson and J Seinfeld. Relative humidity and temperature dependence of the ammonium nitrate dissociation constant. *Atmospheric Environment*, 41:126–135, 2007.

[93] Kiyoshi Matsumoto and Hiroshi Tanaka. Formation and dissociation of atmospheric particulate nitrate and chloride: An approach based on phase equilibrium. *Atmospheric Environment*, 30(4):639–648, February 1996.

[94] D. J. Jacob, J. H. Crawford, H. Maring, A. D. Clarke, J. E. Dibb, L. K. Emmons, R. A. Ferrare, C. A. Hostetler, P. B. Russell, H. B. Singh, A. M. Thompson, G. E. Shaw, E. McCauley, J. R. Pederson, and J. A. Fisher. The Arctic Research of the Composition of the Troposphere from Aircraft and Satellites (ARCTAS) mission: design, execution, and first results. *Atmospheric Chemistry and Physics*, 10(11):5191–5212, June 2010.

[95] H. M. Worden, M. N. Deeter, C. Frankenberg, M. George, F. Nichitiu, J. Worden, I. Aben, K. W. Bowman, C. Clerbaux, P. F. Coheur, A. T. J. de Laat, R. Detweiler, J. R. Drummond, D. P. Edwards, J. C. Gille, D. Hurtmans, M. Luo, S. Martínez-Alonso, S. Massie, G. Pfister, and J. X. Warner. Decadal record of satellite carbon monoxide observations. *Atmospheric Chemistry and Physics*, 13(2):837–850, January 2013.

[96] Y. Yin, F. Chevallier, P. Ciais, G. Broquet, A. Fortems-Cheiney, I. Pison, and M. Saunois. Decadal trends in global CO emissions as seen by MOPITT. *Atmospheric Chemistry and Physics*, 15(23):13433–13451, December 2015.

[97] R. E. Honrath. Regional and hemispheric impacts of anthropogenic and biomass burning emissions on summertime CO and O $_3$ in the North Atlantic lower free troposphere. *Journal of Geophysical Research*, 109(D24):D24310, 2004.

[98] Hervé Petetin, Bastien Sauvage, Mark Parrington, Hannah Clark, Alain Fontaine, Gilles Athier, Romain Blot, Damien Boulanger, Jean-Marc Cousin, Philippe Nédélec, and Valérie Thouret. The role of biomass burning as derived from the tropospheric CO vertical profiles measured by IAGOS aircraft in 2002–2017. *Atmospheric Chemistry and Physics*, 18(23):17277–17306, December 2018.

Appendix A

Supplementary Information. Chapter 3

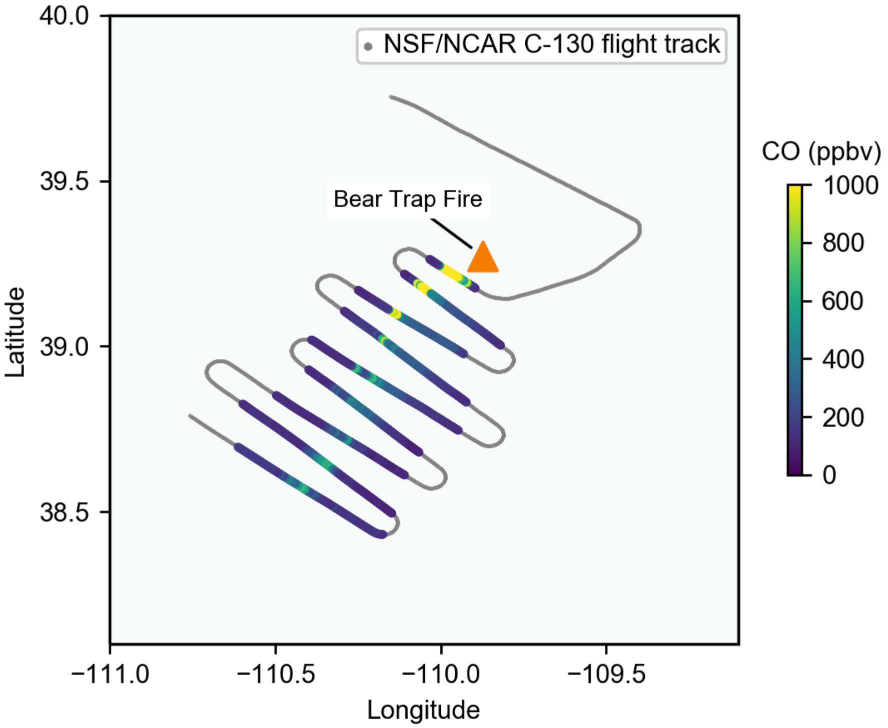

Figure A.1: NSF/NCAR C-130 flight track around the Bear Trap Fire, 9 August 2018 during Research Flight 9 (RF09), colored by CO mixing ratios. The black arrow shows the average wind direction and the orange triangle shows the Bear Trap Fire location.

$$\ln\left(\frac{\Delta X_1}{\Delta X_2}\right)_t = -[OH](k_1 - k_2)t + \left(\frac{\Delta X_1}{\Delta X_2}\right)_0 \tag{A.1}$$

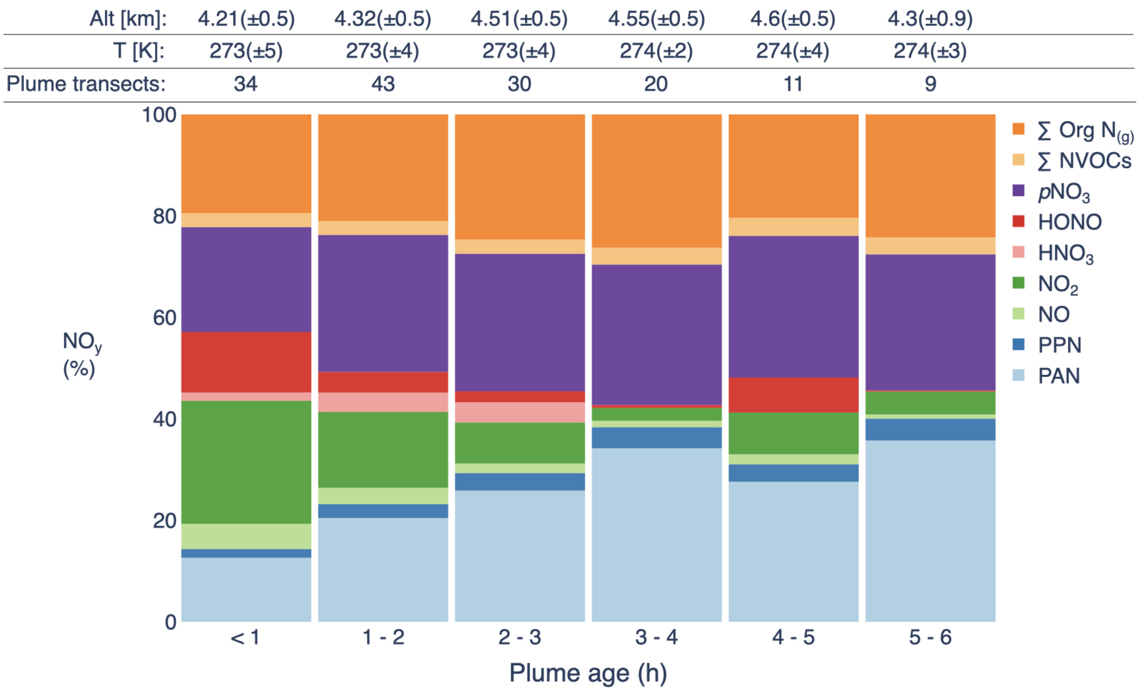

Figure A.2: Partitioning of NO$_y$ as a function of physical age (h) outside the most concentrated part of western U.S. wildfire smoke plumes sampled in a pseudo-lagrangian fashion during WE-CAN 2018. Each of the plumes included in this figure are associated with a specifically targeted fire (see Figure 2.1). The observations shown here correspond to sampling in the portion of each plume crossing where CO is between the 25th and the 75th percentile of that crossing. To calculate the enhancement of each species, a crossing-specific background mixing ratio for each individual species is subtracted.

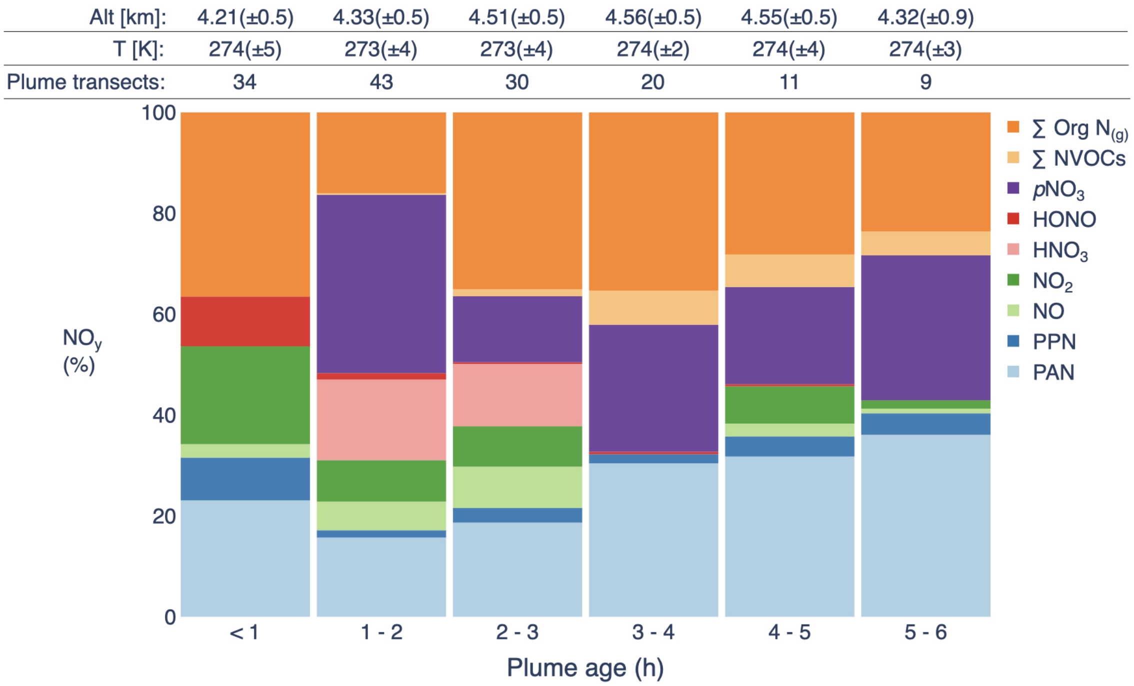

Figure A.3: Partitioning of NO$_y$ as a function of physical age (h) in the edges of western U.S. wildfire smoke plumes sampled in a pseudo-lagrangian fashion during WE-CAN 2018. Each of the plumes included in this figure are associated with a specifically targeted fire (see Figure 2.1). The observations shown here correspond to sampling in the edges of the plume, which is defined as the portion of each plume crossing where CO is between the 5^{th} and the 25^{th} percentile of that crossing. To calculate the enhancement of each species, a crossing-specific background mixing ratio for each individual species is subtracted.

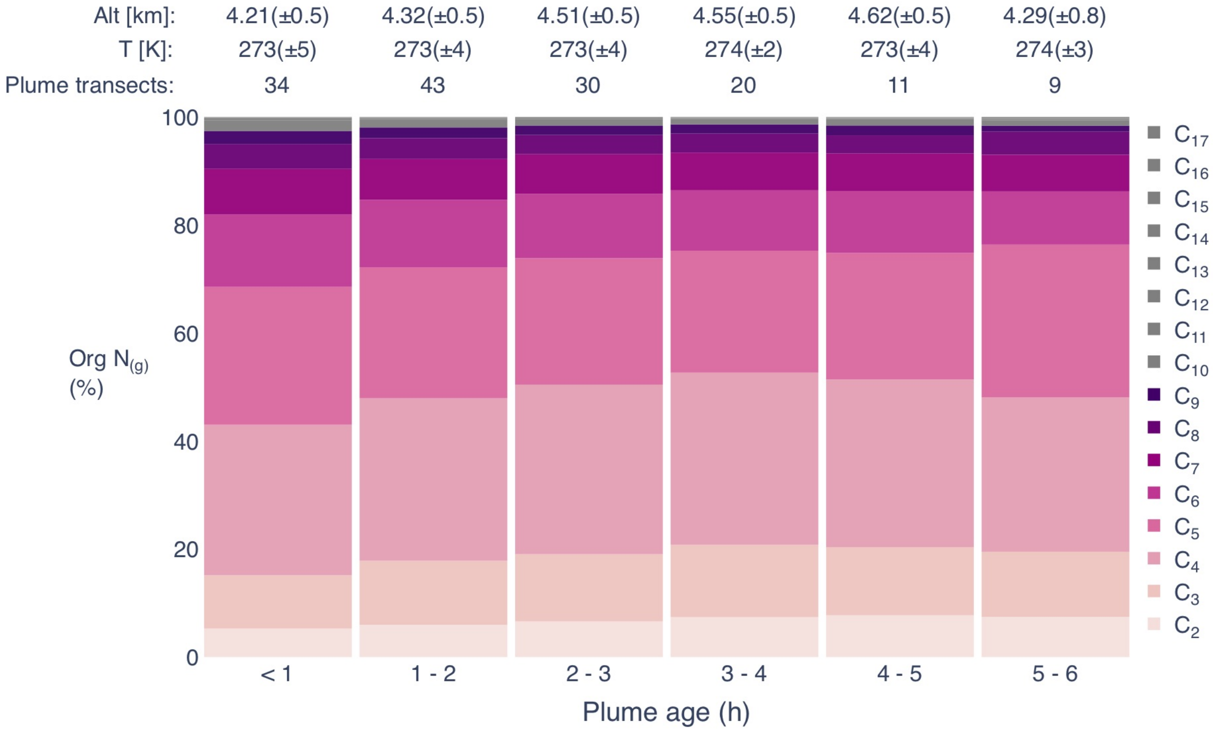

Figure A.4: Partitioning of $\sum$Org N (dark orange bars in Figure 3) as a function of physical age (h) in the most concentrated cores of western U.S. wildfire smoke plumes sampled in a pseudo-lagrangian fashion during WE-CAN. The different Org N species have been grouped by their carbon atom number. Molecules with > 10 carbon atoms are depicted in grey. Each of the plumes included in this figure are associated with a specifically targeted fire (see Figure 2.1). The observations shown here correspond to sampling in the center of the plume, which is defined as the portion of each plume transect where CO is above the 75^{th} percentile of that transect. To calculate the enhancement of each species, a transect-specific background mixing ratio for each individual species is subtracted.

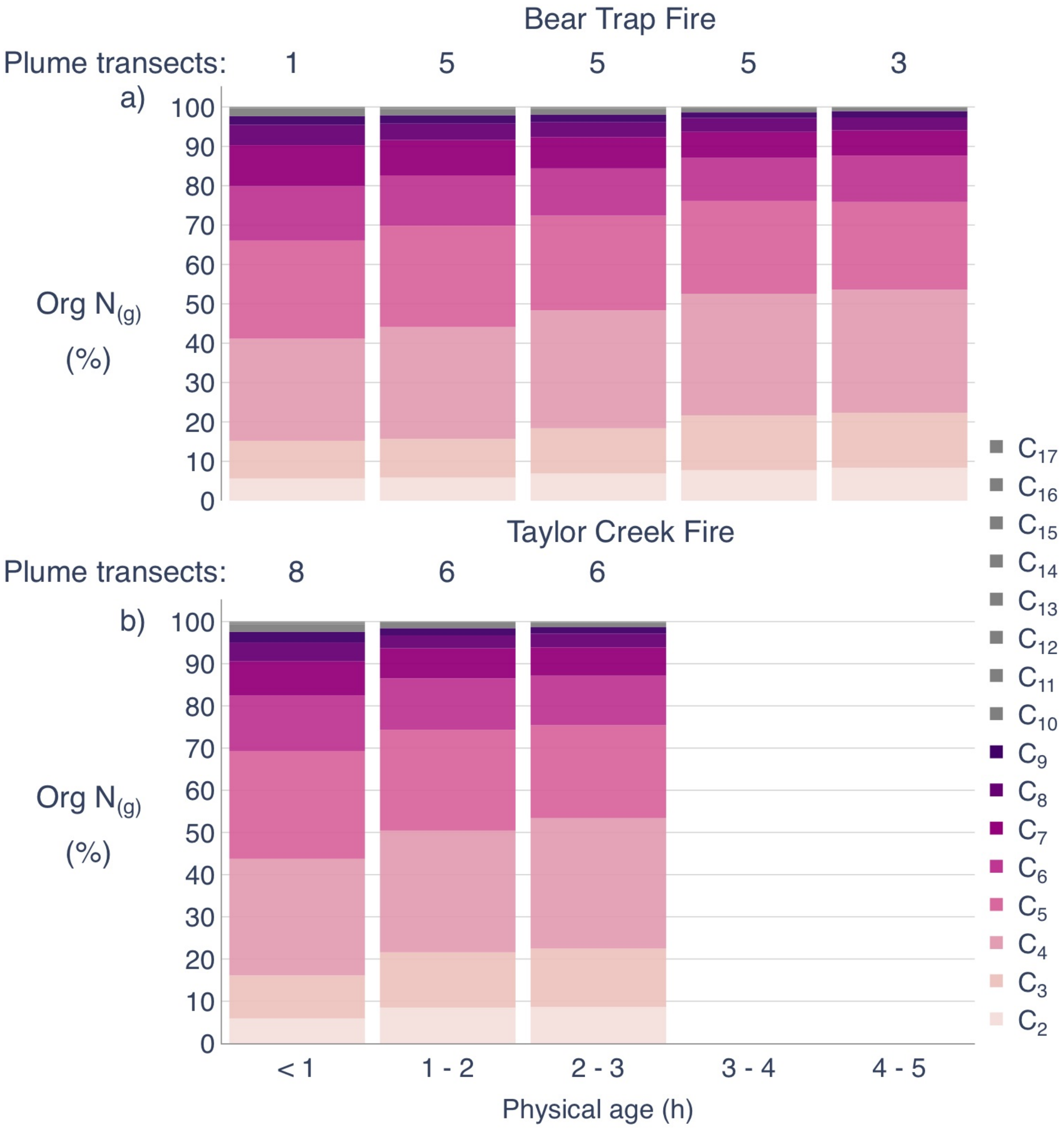

Figure A.5: Partitioning of $\sum$Org N (dark orange bars in Figure 3.2) as a function of physical age (h) in the most concentrated cores of the Bear Trap and Taylor Creek Fire smoke plumes sampled during WE-CAN. These smoke plumes were sampled in a pseudo-lagrangian fashion twice. Here we present the average of the plume transects from both samples binned by their corresponding physical age. The center of the plume is defined as in Figure 3, and a transect-specific background mixing ratio for each individual species was subtracted. The numbers above each bar signify the individual transects through the plume in each physical age bin. Error bars were calculated by adding the individual uncertainty for each NO_y species in quadrature.

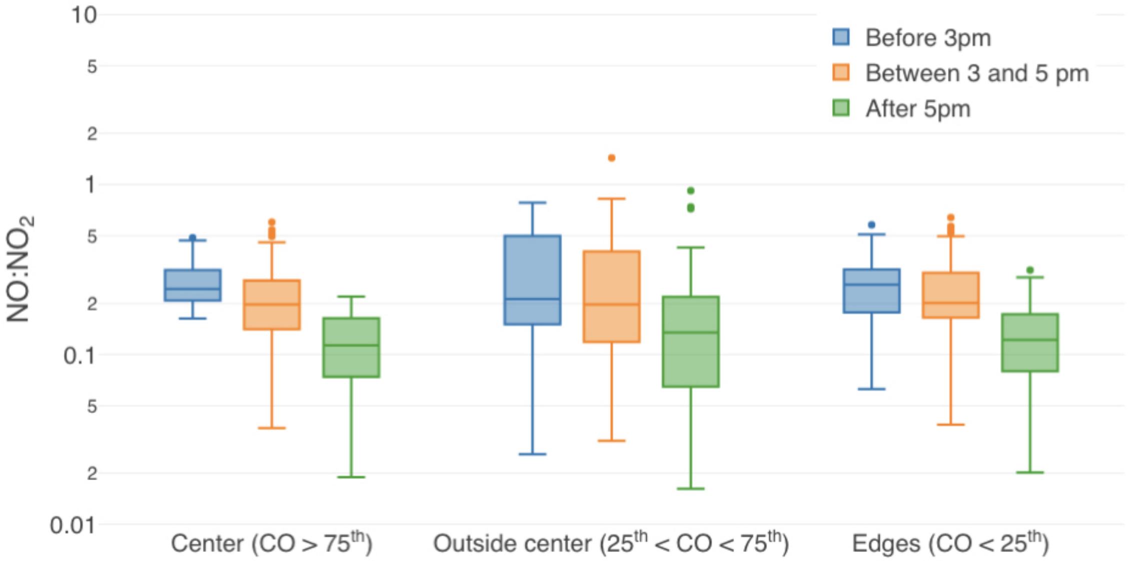

Figure A.6: NO to NO_2 ratios in the center, outside the center, and the edges of western US wildfires smoke plumes. The colors of the whisker plots represent different times of the day where blue signifies samples collected before 3 PM (LT), orange signifies samples collected between 3 PM and 5 PM (LT), and green signifies samples collected after 5 P< (LT).

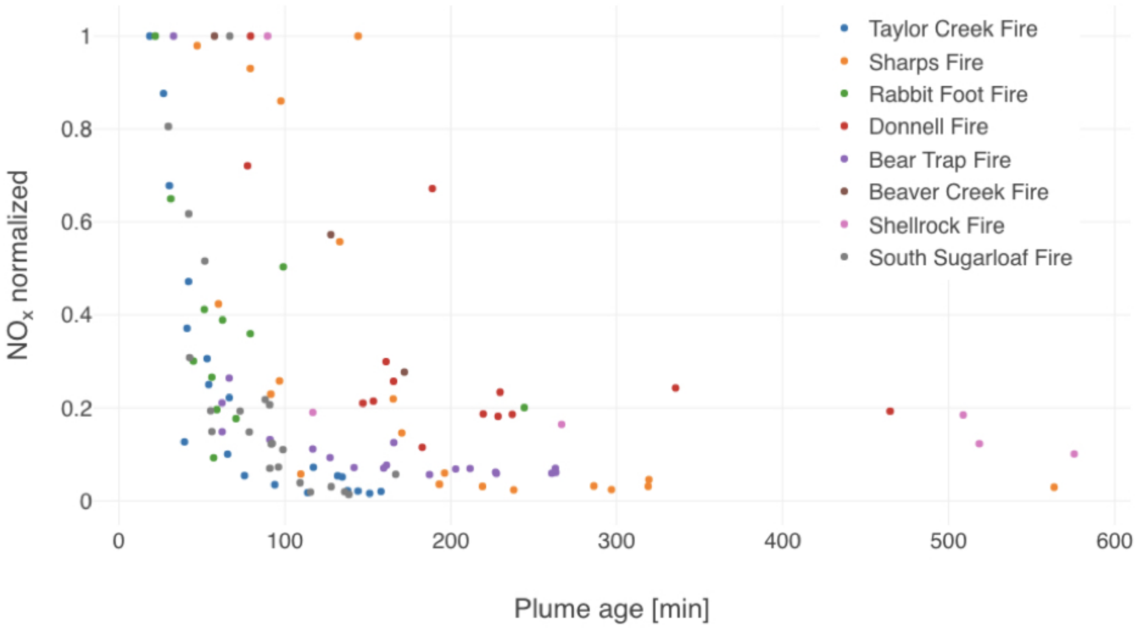

Figure A.7: Normalized NO_x in plume cores as a function of plume age [min] for specific fires. The average *e*-folding time for NO_x is 90 minutes.

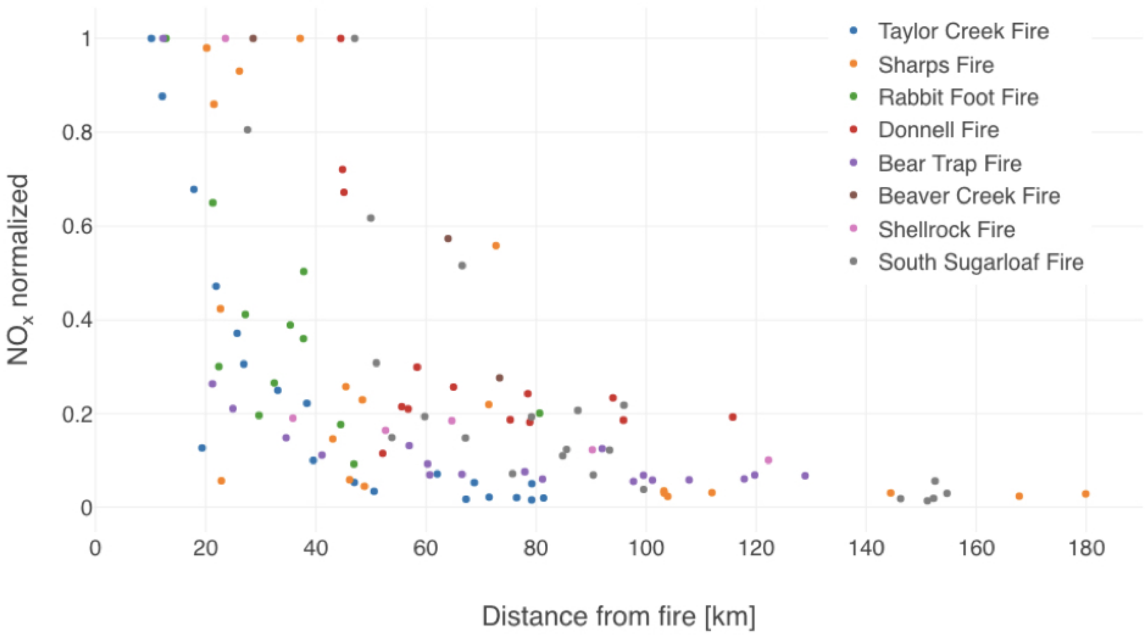

Figure A.8: Normalized NO_x in plume cores as a function of distance from the fire [km] for specific fires. The average *e*-folding distance for NO_x is 37 kilometers downwind.

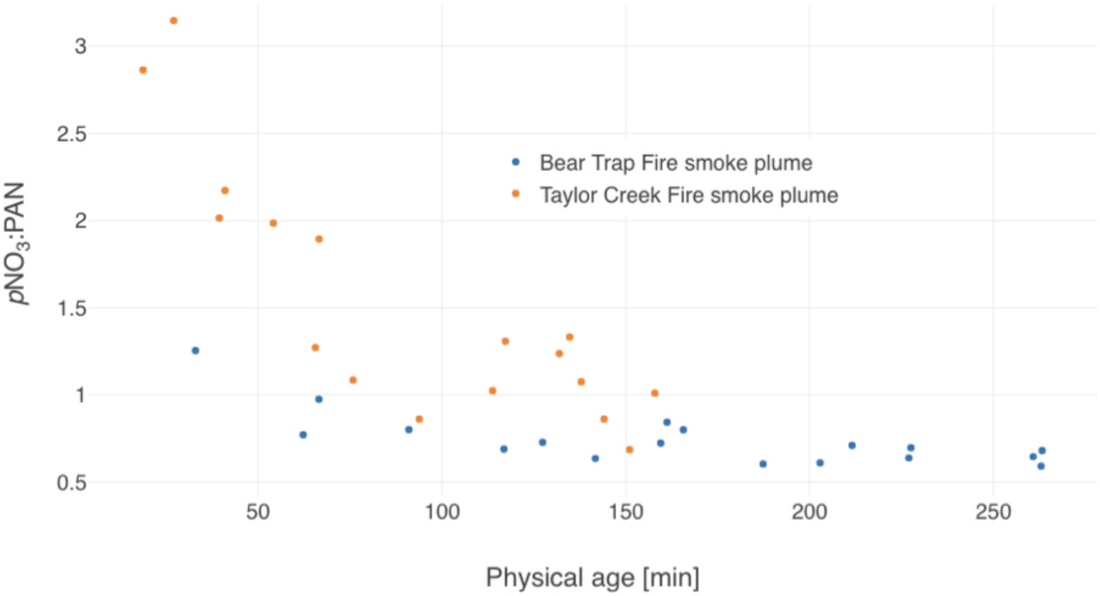

Figure A.9: $p\mathrm{NO}_3$ to PAN ratios at the core of the plume for the Bear Trap Fire (blue) and the Taylor Creek Fires (orange) smoke plumes as a function of physical age

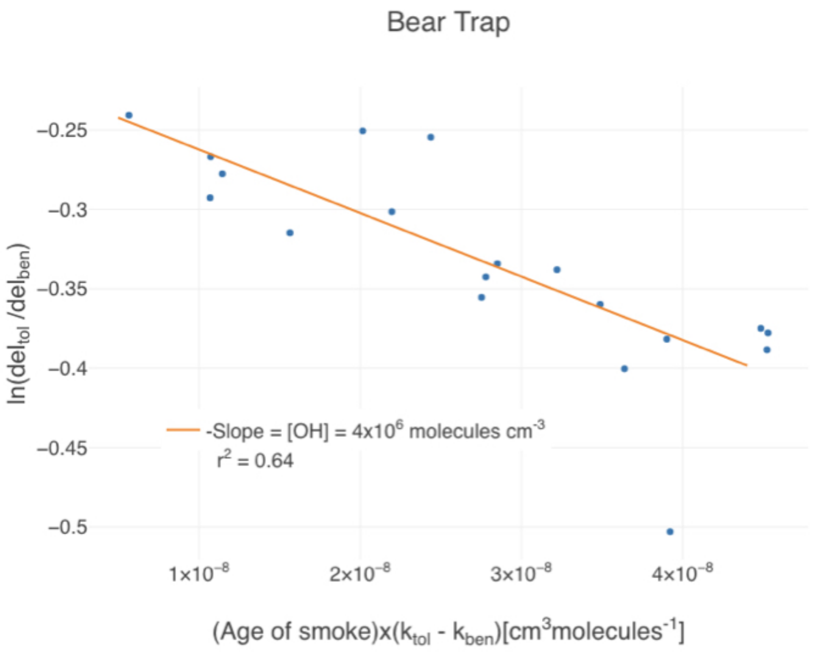

Figure A.10: Plot of Eq. (A.1) for the Bear Trap Fire smoke plume. Mixing ratios for toluene and benzene are at the core of the plume. The slope of the fit provides an estimate for the OH concentration at the core of the plume.

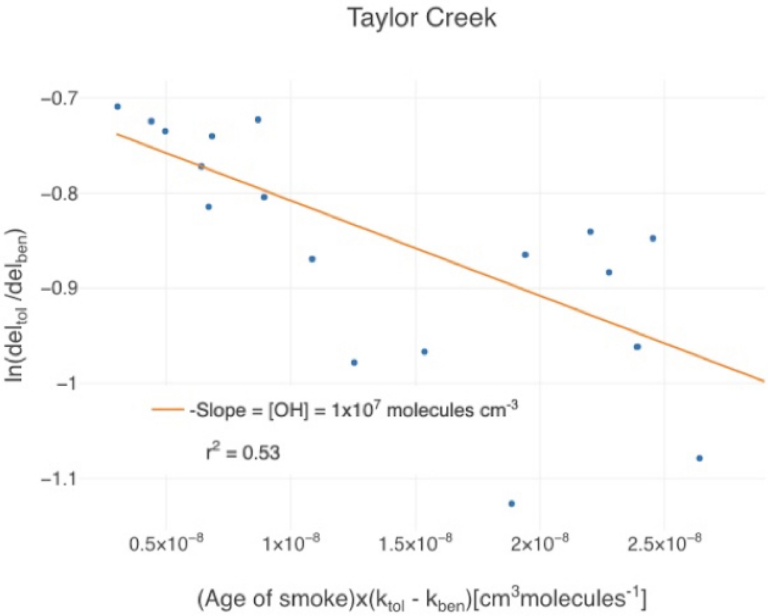

Figure A.11: Plot of Eq. (A.1) for the Taylor Creek Fire smoke plume. Mixing ratios for toluene and benzene are at the core of the plume. The slope of the fit provides an estimate for the OH concentration at the core of the plume.

Appendix B

Supplementary Information. Chapter 4

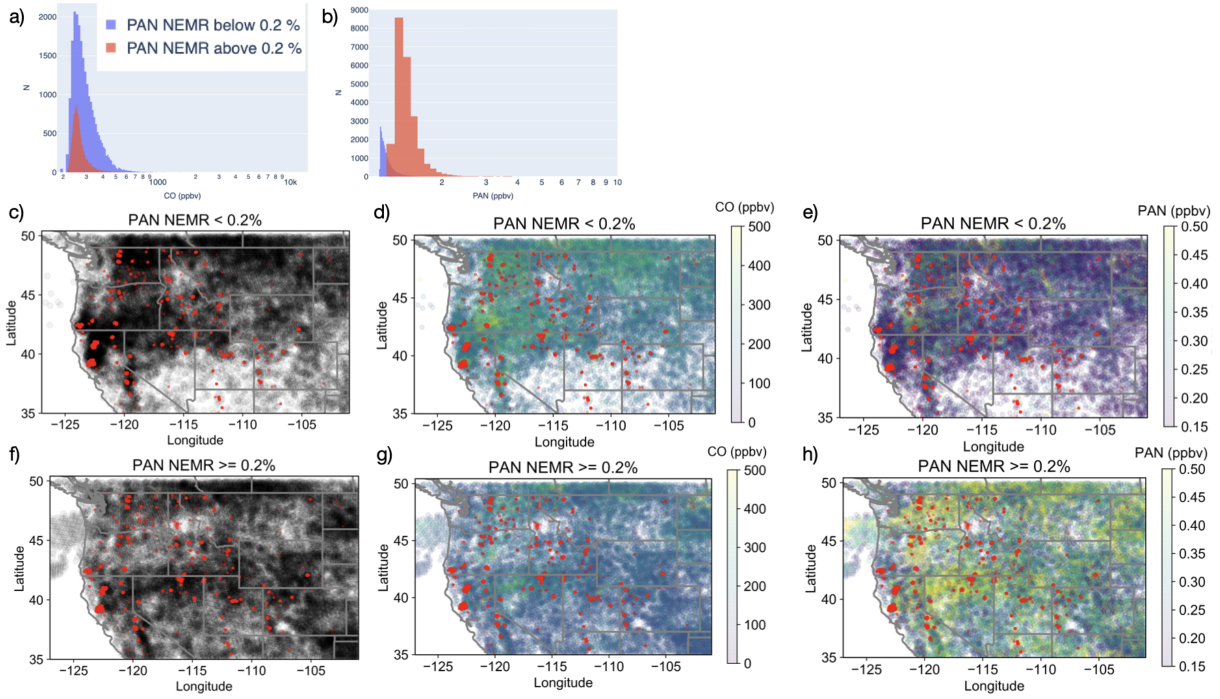

Figure B.1: Distribution of tropospheric CrIS a) CO and b) PAN for PAN NEMRs below (blue) and above (red) 0.2%. c) and f) show the spatial distribution of the retrievals that meet the NEMR criteria above. d) and g) same as c) and f) colored by tropospheric CO. e) and h) same as c) and f) colored by tropospheric PAN